Università degli Studi di Ferrara

DOTTORATO DI RICERCA
in Fisica

CICLO XXX

COORDINATORE Prof. GUIDI Vincenzo

Studies of innovative photon detectors working in the single-photon regime for the RICH detector of the CLAS12 experiment.

Settore Scientifico Disciplinare FIS/04

Dottorando
Dott. Balossino Ilaria

Tutore
Dott. Contalbrigo Marco

Anni 2014/2017

Contents

List of Figures

Introduction

High energy physics focuses its main effort in the subatomic particle detection and interaction study. More and more sophisticated experiments have been developed to follow the urge to detect new particles and structures with a continuously improving technology. By the day a new experiment begins, further upgrades start to be envisioned to boost the precision with which scientists improve the knowledge of the nature around us, and in particular, of the elementary components and their interactions.

There are several experimental facilities that investigate this subatomic world, each one with different techniques. The Thomas Jefferson National Accelerator Facility (JLAB) is one of the most important laboratories dedicated to nuclear physics research, it hosts the CEBAF (Continuous Electron Beam Accelerator Facility) Large Acceptance Spectrometer at 12 GeV (CLAS12) and it is related to this work. The JLAB facility has been recently upgraded together will all the experiments involved in it, to double the initial 6 GeV electron beam energy and increase by orders of magnitude the luminosity. The deep-inelastic scattering experiment CLAS12 is the evolution of the original CLAS: using polarized nuclear targets and beam, it aims at the study of the spin dependence of the nucleon structure functions.

A description of the JLAB facility, of the CLAS12 experiment with its scientific program and experimental setup will be given in the first part of Chapter 1. The most important development of the CLAS12 experiment correlated with this work is the replacement of one of the already existing gas Cherenkov detectors with a newer and innovative Ring Imaging CHerenkov detector (RICH). The aim of this upgrade, together with other new installations, is to improve the detection capabilities over a wider range momenta and luminosities achieved with the new beam. The RICH detector has to satisfy some requirements imposed by the environment and by the geometry of the experiment. It has to have an active area with the smallest possible dead space, to sustain a high rate with low dead time, to ensure high spatial and time resolutions to best identify the particles under investigation. The required detector performance and all its components will be described in the

second part of Chapter 1.

This work concentrates on one of the most delicate and innovative elements of the CLAS12 RICH: the photon detector. The CLAS12 RICH detector will be composed of modules covering two out of six sectors of the experiment with similar geometries but different degrees of innovation. The photon detector that has been chosen and its now assembled in the first module is based on Multi-Anode Photo-Multiplier Tubes (MAPMTs). For the second sector, that should be ready in few years, a new photon detection technology has been considered: Silicon Photo-Multiplier (SiPM). A general description of the interaction of the photon with the matter and the technology developed to detect it will be given in Chapter 2, together with a discussion of the working principles and of the nominal performance of the chosen sensors.

The following chapters present the author's contributions to the RICH project. The CLAS12 RICH is the first to use flat panel MAPMTs of large area. A dedicated front-end electronics has been developed for the readout of this kind of sensors, to enable single photon detection, since they were not originally designed for this application. The author's contribution, presented in Chapter 3, included the preparation of the setup for the characterization of all the final components (sensors and electronics) of the photon detector for the first sector, the analysis of the collected data to extract a set of parameters that optimizes the performance of the MAPMTs during the physics runs and the definition of a set of performance indicators to be used as a reference during calibration run.

Although SiPMs have never been used in Cherenkov application, the rapid evolution in their production technology has lately opened interesting opportunities. The author's work on the SiPMs, presented in Chapter 4, is concentrated on testing this innovative technology to validate its use in the CLAS12 environment. The first part of the chapter describes the irradiation test and a detailed study of the dark counts, dedicated to the characterization of the detector background. The second part explores the single photon detection capability of novel SiPM matrices in conjunction with the RICH readout electronics.

The author's contribution to the first RICH sector photon detector assembling and commissioning is described in Chapter 5. A dedicated setup was developed to test the photon detector with cosmic muons, in a configuration mimicking the one in the experimental hall. The first analysis of the cosmic data allowed to test the correct mapping of the detector and the timing precision.

The conclusions are meant to summarize the main outcomes of each study done as part of this work and to give an idea of what and how could be done in the future to maximize the performance of the RICH detector.

Chapter 1

The RICH detector for CLAS12

In the last decades the knowledge in nuclear, hadronic and electroweak physics has been significantly enhanced through continuously improving theoretical and experimental tools. The more we learn about parton dynamics the more the community aims at starting new experiments to reduce the unknown from the fundamental structure of matter, with a particular attention to the nucleon, of which the observable physical world around us is formed. In this thesis a new instrument to study the tridimensional structure of the nucleon with sensitivity to the quark flavor is presented. The study is based on the deep-inelastic scattering of polarized nuclear targets. It is a Ring Imaging CHerenkov detector (RICH) with innovative design and components: its role is to improve the particle identification capability of the CEBAF Large Acceptance Spectrometer (CLAS12) hosted in the experimental hall B of the Thomas Jefferson National Accelerator Facility (JLAB). This chapter introduces the physics motivations, describes the CLAS12 experiment and presents the design and specifications of the RICH detector.

1.1 The Thomas Jefferson National Accelerator Facility

The Thomas Jefferson National Accelerator Facility (JLAB) is one of the world leading laboratories in this field. This laboratory hosts the Continuous Electron Beam Accelerator Facility (CEBAF) that has been recently upgraded to reach 12 GeV energy. This accelerator serves four different experimental halls: A, B, C and, just added with the upgrade, D. These four experimental halls together will produce a core set of capabilities. With high intensity, highly polarized and stable electron beams, this laboratory will provide innovative opportunities for probing and extending the Standard Model through parity

violation studies and new particles discovery [1]. A brief introduction of the program of each hall follows.

Hall A   is the largest of these four experimental staging areas. Its physics program spreads from nucleon and few-body form factor studies, strange-quark structure of the proton, nucleon spin and nuclear structure at small internucleon separations. Hall A collaborators represent more than 70 institutions and 18 countries.

Hall B   is the site of the upgraded version of the old CLAS (CEBAF Large Acceptance Spectrometer), now called CLAS12, built as part of the JLAB 12 GeV upgrade project. The aim is to investigate and understand nuclear structure via Generalized Parton Distributions (GPD). CLAS12 collaboration involves nearly 150 physicists from more than 30 universities in the U.S., Europe, South America, the former Soviet Union, and Korea. Further insight will be given later in this document.

Hall C   will improve the experimental setup adding at the already existing High Momentum Spectrometer a new Super High Momentum Spectrometer (SHMS). Here, the setup supports high-luminosity experiments detecting reaction products with momenta up to the full beam energy, a virtue well matched for making high-precision measurements of neutrino-like cross sections to map valence quarks in nucleons and nuclei.

Hall D   searches for new exotic states and strives to measure mass and spin-parity. GlueX is the dedicated spectrometer of this hall. It is designed to search for QCD-predicted hybrid mesons using photoproduction via linearly polarized photons. This will allow to run a partial wave analysis of any new observed states to determine whether they have allowed or exotic quantum numbers. The spectrometer can also perform studies of meson and baryon spectroscopy, which bears on the physical origins of quark confinement.

The planned experiments, just described, vary in required luminosity by more than three orders of magnitude and have momentum resolution requirements ranging from a few percent to 10^{-4}. To emply polarized target these experiments must comply to the requirements given by geometrical restrictions, particle identification capability and possibility to operate in high magnetic field. Polarized electrons, routinely produced at CEBAF, will serve the parity violation experiments and many of the electroproduction experiments planned. All of them aim to an excellent identification of electrons, as well as tagging and identification of scattered target nucleons, and/or produced hadrons such

as pions or kaons. The range of requirements necessarily leads to major differences among the halls and some specialized capabilities. The 12 GeV CEBAF

(a) Comparison to other major   (b) Comparison to 6 and 4 GeV
           facilities   CEBAF
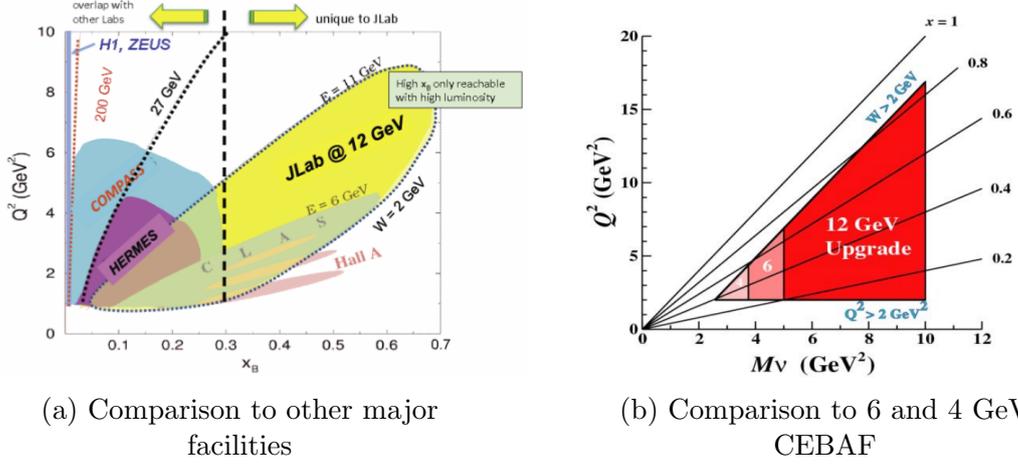
Figure 1.1: Status of the kinematic coverage of 12 GeV

is suited to examine the valence quark region of $x_B > 0.25$ (x_B being the Bjorken scaling variable) in contrast with other major facilities that focus on the sea quark region below x_B of $0.1-0.01$. In Figure 1.1a the kinematic coverage provided by the 12 GeV upgrade is shown. Figure 1.1b shows the kinematic coverage at different beam energies. The possible beam currents reach $100\mu A$ in hall A and C. It is possible to see that the upgrade provides enhanced access to the deep-inelastic scattering (DIS) regime with enough luminosity to reach the high-Q^2, high-x_B region.

1.2 CLAS12

In hall B, the CEBAF Large Acceptance Spectrometer (CLAS) was designed to study exclusive multi-particle reactions with its combination of large acceptance and moderate momentum resolution. It has been upgraded to CLAS12 and optimized for the study of the internal dynamics, 3D imaging of the nucleon, quark hadronization processes through exclusive and semi-inclusive processes [2]. With these upgraded new and unique features, it will be a flagship for JLAB accessing to:

- high beam energy and luminosity
- high beam polarization

- longitudinally and transversely polarized proton and deuterium targets without dilution
- variety of nuclear targets
- large acceptance, multipurpose spectrometer

1.2.1 Scientific Program

The past lepton-nucleon scattering experiments improved significantly the knowledge of the connection of the partonic dynamics to the nucleon through the parton distribution functions (PDFs) and Fragmentation Functions (FFs). The investigation of these physics distributions brought to intriguing aspects of the nucleon structure: sizeable breaking of isospin symmetry in the light sea quark sector suggesting differences between the sea quark and antiquark distributions; the steep rise of the distributions at small momentum fractions, an interesting pattern of modifications of the distributions in nuclei; and the contribution from quark and antiquarks to a small fraction of the proton's spin. These studies revealed the necessity to further investigate the proton spin structure in terms of parton orbital angular momenta and gluons' role [3].

The three-dimensional momentum and space resolution of the nucleon structure can be obtained for the first time through the Transverse Momentum Dependent (TMD) distributions together with the so-called Generalized Parton Distributions (GPDs). These new concepts, which go beyond the collinear approximation, are a key to unravel the intricacies of the intrinsic motion of partons and the possible connection between their orbital motion, their spin and the spin of the nucleon. Mapping of GPDs and TMD distributionsallow for the deduction of a three-dimensional image of the nucleon, which is a major focus of the hadron physics community and it constitutes a milestone in the physics program of the Jefferson Laboratory (JLAB) 12 GeV upgrade.
TMD distributions are measured in semi-inclusive deep-inelastic scattering (SIDIS) where at least one hadron is detected in the final state in addition to the scattered lepton. Those experiments provide access to the strangeness distributions and to the role of the strange quarks in the fragmentation process.
GPDs can be probed in hard exclusive processes: the nucleon stays intact and the final state is fully observed. In this case different spin and azimuthal asymmetries of exclusive hadron can provide a unique possibility to access the elusive chiral-odd GPDs.
In both these processes, kaons play an important role in understanding the

dynamics behind spin-orbit correlations in hard processes. These particles' results point to a significant role of sea quarks and in particular strange quarks. Pioneering polarized SIDIS experiments have revealed surprising effects in various kaon production observables, which deviate from the expectations based on u-quark dominance for the scattering off a proton target. Such processes can be critical in the studies of p_T dependencies of different hadrons: recent experimental (COMPASS, HERMES) and theoretical studies indicate the fragmentation involving strange quarks may have a very different orbital structure (Fig. 1.2a). If a particular spin orientation is considered, the up and the down quark distributions appear as opposite. The opportunity to address also sea s-quarks distribution can help understanding the role of the sea quark in the nucleon, and if their distribution shows similar anisotropies like in the up and down case. This is possible by separating kaons and pions in the final state with very efficient particle identification in a broad momentum range. Also in exclusive processes the identification of kaons will be critical for separation of different exclusive states involving K and K^*. These kind of measurements will help accomplishing the CLAS12 program of studies of the three-dimensional structure of the nucleon. In particular this region will cover the kinematic region around $x_B = 0.1$ where the deviation from the expected behaviour of all kaon observables are most pronounced.

The effects of nuclear matter are essential for the interpretation of high energy proton-nucleus interactions and ultra-relativistic heavy-ion collisions. In the lepton-nucleon scattering the energy and momentum transferred to the hit parton are well determined: it is "tagged" by the scattered lepton and the nucleus is basically used as a probe at the Fermi scale with increasing size or density. The nuclear SIDIS has an enormous potential to investigate the hadronization mechanism thanks to the well and unique determination of the leptonic and hadronic planes. The azimuthal angle between them allow to determine the path of the produced hadron, as shown in Fig. 1.2b, where the typical angles of interest in SIDIS analyses are depicted.
The nuclear modification to the angular modulation of the production rate, as well as the transverse momentum broadening of the produced hadrons, provides a sensitive probe to the color and parton density fluctuations inside nucleus, which is very important for the understanding of the initial condition of relativistic heavy ion collisions. The high beam intensity and the usage of a large variety of nuclear targets will provide data in a kinematic region that is very suitable for studies of nuclear effects. Also in these kind of studies the capability of identifying pions, kaons and protons will be crucial for gaining more insights into the space-time evolution of the hadronization process

(a) When the spin of the nucleon is taken into consideration (white arrow), the quark distribution is distorted in opposite ways for up- and down-quarks. [4]

(b) Typical angle representation
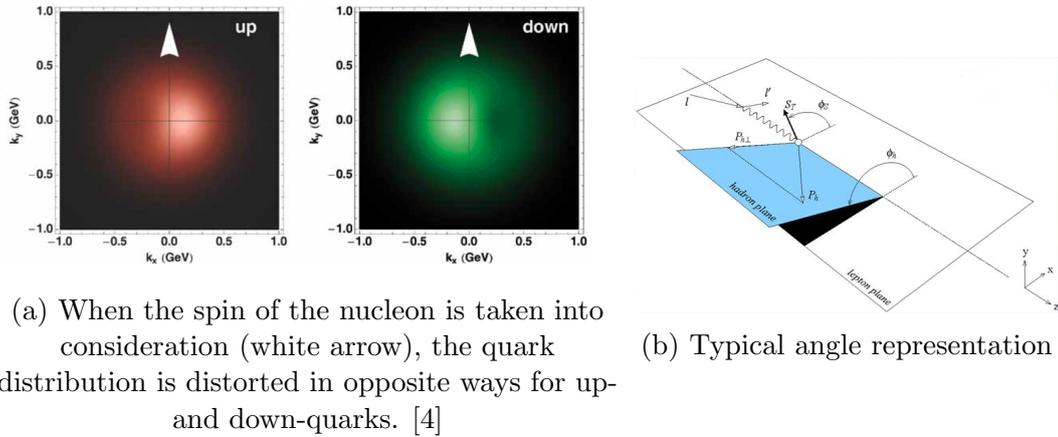
Figure 1.2: SIDIS properties

The exotic mesons are also under investigation to deepen our knowledge about the dynamics of QCD. It is possible to identify exotic configurations such as hybrids ($q\bar{q}g$), tetraquarks ($qq\bar{q}\bar{q}$) and glueballs through strangeness-rich final states, where the kaons from the decay of the involved ϕ-meson are usually high energetic. Kaon identification over the whole accessible momenta, up to $8\,\mathrm{GeV/c}$, would hence provide unique capabilities for these studies.

1.2.2   The CLAS12 Detector

The spectrometer will operate at a luminosity of 10^{35} cm^{-2}s^{-1} with highly polarized beam on nucleon targets.

Design Overview   CLAS12, schematically shown in Fig. 1.3a, uses many already existing detector components. Major new components include the superconducting torus coils that cover the forward angle range, a new gas Cherenkov counter, additions to the electromagnetic calorimeter and the central detector. Modifications and new components will be briefly described in the following.

The Beam Line and the Target   will be mainly kept from the existing setup. This includes the photon tagger and the pair spectrometer, the polarized photon instrumentation, a polarized target (for photon experiments) and beam position and current monitors. [2]
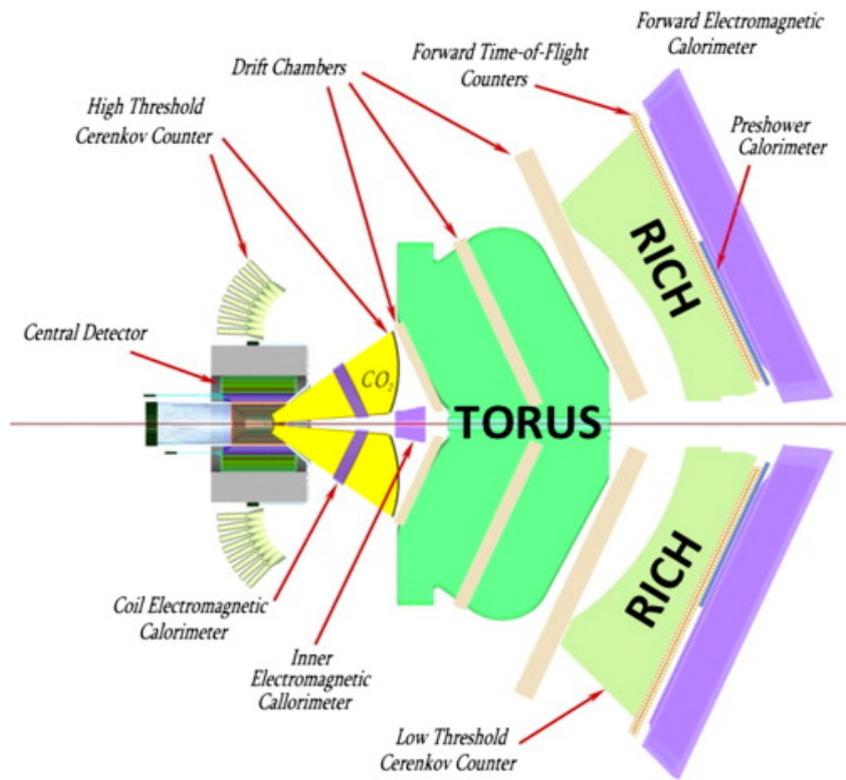
(a) Horizontal view
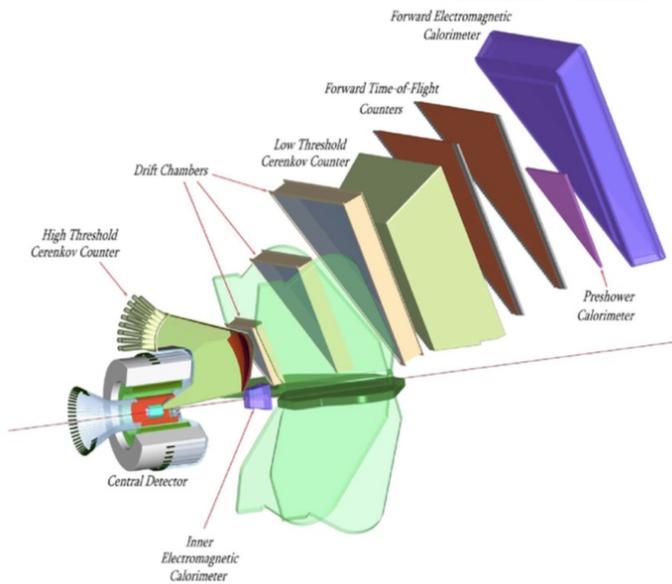
(b) Exploded view of one of the six sectors

(c) Hexagonal geometry of the FTOF

Figure 1.3: Schematic views of the CLAS12 spectrometer

The Central Detector (CD) will detect charged particles from 35°
to 125°. Its main component is a compact superconductive solenoid magnet
(5T). It fulfills several goals: it provides magnetic shielding of all tracking
detectors from charged electromagnetic background, mostly Moeller electrons
and particles from secondary interactions; it purveys the magnetic field for
the layers of silicon strip sensors to allow the momentum analysis of charged
particles at large angles; it gives the uniform field needed for the operation of
a dynamically polarized solid state target. Particle identification is achieved
by the combination of momentum analysis and time-of-flight measurements in
the scintillation counters.

The Forward Detector (FD) shown in an exploded design in Fig. 1.3b,
is meant to detect charged and neutral particles in the polar angle range be-
tween 5° and 40°. It is based on the 2T superconducting toroidal magnet and
retains the same six-sector structure of the CLAS spectrometer (Fig. 1.3c). It
includes a tracking system made of a vertex tracker and three regions of Drift
Chambers, the second of which inside the toroidal field, two gas Cherenkov
detectors (High-Threshold Cherenkov Counter, HTCC, and Low-Threshold
Cherenkov Counter, LTCC) for electron/pion separation, a Time-Of-Flight
(FTOF) system for hadron identification and an electromagnetic calorimeter
(EMC) to help in electron identification and to detect neutral particles. More-
over, to improve the particle identification and event reconstruction in the
momentum range between 3 and 8 GeV/c, 2 sectors of the existing LTCC
will be replaced with a Ring-Imaging CHerenkov (RICH) detector. This last
detector will be of interest for this thesis.

1.3 The RICH detector

SIDIS reactions, as already introduced in the physics program (1.2.1), rely
on a good separation of kaons from pions and protons. The high momentum
region (above 6 GeV/c) is important to study the transition from the hard
semi-inclusive to the exclusive regime. The intermediate momentum (4 < p
< 6 GeV /c) and angle (15° < θ < 25°) region is important to reach the
highest values of the hadron transverse momentum. Therefore, CLAS12 must
provide the best PID performances in these two regions. The existing CLAS
detectors as HTCC, LTCC and FTOF were the ones in charge of particle iden-
tification for hadrons in the FD, together with the momentum measurements
from the drift chambers within the toroidal magnetic field. They use to give
relevant contributions in specific kinematic regions: the FTOF is composed by
two panels of plastic scintillators that allow to have a time resolution ranges

between 45 and 80 ps, depending on the polar angle of the particle. This detector can provide the required kaon to pion separation up to momenta of about 3 GeV/c with the 4σ separation expected: it corresponds to a time difference ΔT (πK) = 320 ps for a large angle particles ($\theta = 36°$) achievable up to 2.8 GeV/c momentum; the HTCC is composed by a CO_2 radiator and PMTs with quartz window. It is designed to separate electrons from pions, while kaons and protons are always below threshold and cannot be detected. For pions, the number of photoelectrons (p.e.) goes from 0 at the threshold of about $p = 5\,\mathrm{GeV/c}$ up to 12at $p = 10\,\mathrm{GeV/c}$. As an example with a minimum number of p.e. n_{pe}=3, a 3σ pion to kaon separation may be obtained only above $p = 7.8\,\mathrm{GeV/c}$. The needed 4σ separation in this case may be obtained only in the extreme region of the kaon momentum distribution; the LTCC is made by a C_4F_{10} gas radiator. The threshold for the pion is at $p = 2.7\,\mathrm{GeV/c}$ and a number of p.e. about a factor of two smaller than the HTCC. Kaons are below threshold for momenta up to about $9\,\mathrm{GeV/c}$. Moreover, it has a limit in ϕ and irregular acceptance, and for these reasons in CLAS it has been used for particle ID only after careful determination of fiducial regions [2]. With only these detectors CLAS12 can not provide adequate kaon identification in the momentum range between 3 and 8 GeV/c. Improved particle identification and event reconstruction can be achieved in this momentum range by replacing two sectors of the existing LTCC with a RICH detector [5]. The idea of such a detector will be shown in the following.

1.3.1 Scientific Program

The addition of a RICH detector would significantly enhance the particle identification capabilities of CLAS12 and make Hall B an ideal place for obtaining flavor separated information about the complex multi-dimensional nucleon structure [3]. The novel TMD distributions and GPDs will be uniquely explored in the valence kinematic region where many new, intriguing aspects of nucleon structure are expected to be most relevant. Furthermore, as pions greatly outnumber the other hadrons at nearly all kinematics, the RICH detector can tremendously reduce the backgrounds for the detection of unstable particles that decay to at least one charged non-pion, hence opening a new window for studying exotic mesons with strangeness contents [6]. In particular, the RICH contributions to the CLAS12 physics program are:

- **study of the strange distributions** of the nucleon in the valence kinematic region using kaon production in unpolarized and doubly longitudinally polarized deep-inelastic scattering off proton and deuterium targets, as well as exclusive kaon-hyperon and ϕ-meson production;
- **study of the flavor and kinematic dependence of the intrinsic**

transverse quark momenta employing fully differential analyses of
pion and kaon production in unpolarized deep-inelastic scattering off
proton and deuterium targets;

- **study of the TMD quark distributions** via the extraction of spin-
  and azimuthal asymmetries for pions and kaons from deep-inelastic scat-
  tering off unpolarized, transversely and longitudinally polarized proton
  and deuterium targets;
- **study of the transverse spatial distribution of 'valence-like' glu-
  ons** from hard exclusive ϕ-meson production variety of nuclear targets;
- **study of quark propagation through cold nuclear matter** via
  nuclear hadronization and transverse momentum broadening employing
  pion and kaon production in deep-inelastic scattering off a variety of
  nuclear targets
- **study of exotic meson configurations** via the tagging of strangeness-
  rich final states in quasi-real photoproduction

1.3.2 Detector
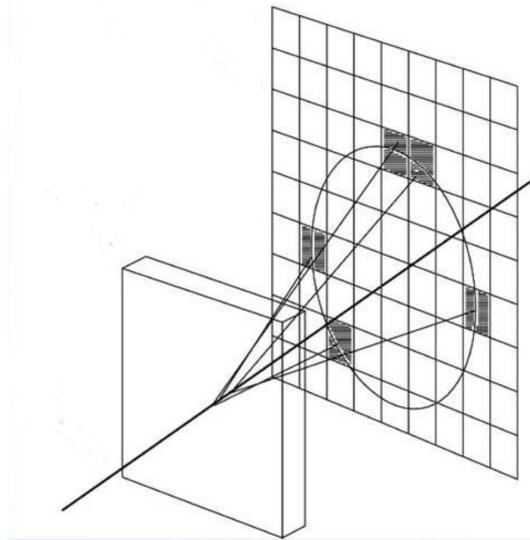
Figure 1.4: Schematic views of a RICH detector

The Ring Imaging CHerenkov (RICH) detector is based on the so-called
Cherenkov light production of a fast particle crossing a medium, typically
called radiator. Those photons are emitted from a particle whose velocity β
is larger than the velocity of the light in a radiator having refractive index

$n(\lambda)$ depending on the wavelength λ. The light spreads in a cone with opening angle θ_C given by:

$$cos(\theta_C) = \frac{1}{\beta n(\lambda)}$$

After a gap region where the cone opens up, the photons are detected and the ring can be reconstructed.

$$\frac{d^2 N}{dL d\lambda} = \left(\frac{2\pi \alpha Z^2}{\lambda^2} \right) sin^2(\theta_C)$$

is the number of Cherenkov photons emitted per radiator thickness unit L at a given wavelength. The higher is the number of the detected photos, the more precise is the measurement of the Cherenkov angle. Once the latter is known, the particle can be identified by its velocity together with the information of the tracking system. Detection efficiency can be influenced by contamination due to misidentification. The parametrization $n\sigma$ shown in Fig. 1.5 helps to estimate the efficiency taking into account the separation between the angle distribution of different particles that depends on the Cherenkov angle resolution σ_θ.
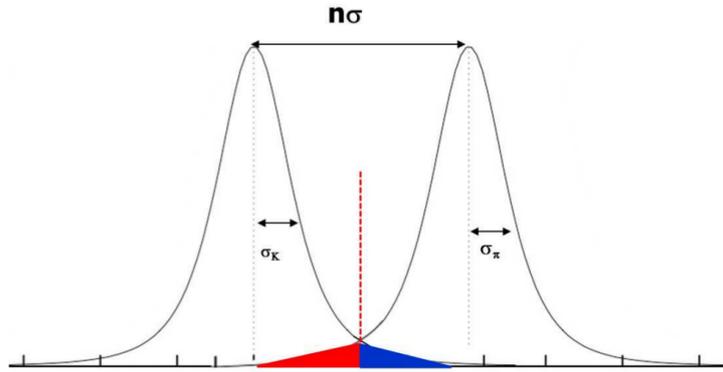
Figure 1.5: Pion to Kaon separation in the RICH. Red triangle: pion contamination; Blue triangle: kaon loss

Design Overview

The detector has to satisfy different requirements: its own expected performance and the constraints imposed by other detectors already existing or in the construction phase. Starting from the performance of the detector, it is
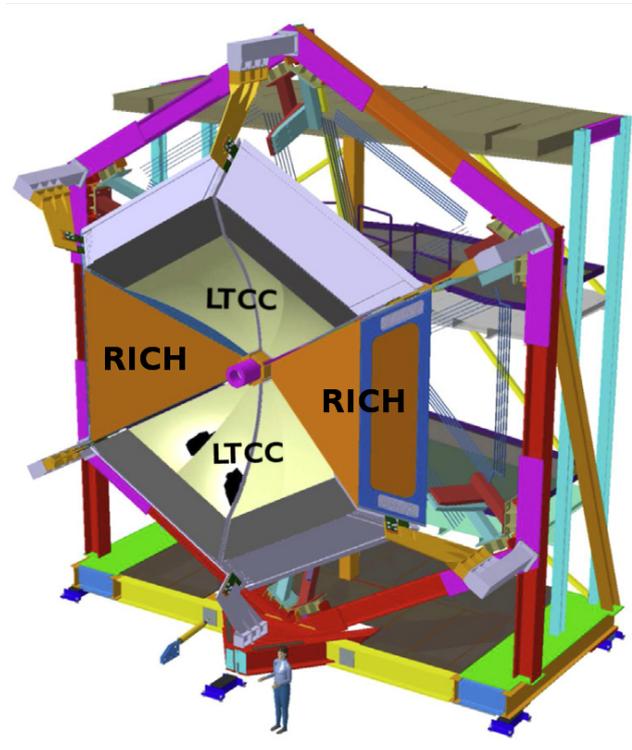
(a) View of the CLAS12 RICH modules replacing the LTCC modules

(b) Cherenkov light opening angle as a
function of the momentum for different
particles using liquid, gas or aerogel
radiator

(c) Residual toroidal magnetic field,
indicated by the vertical color scale, in
the region covered by the RICH
photodetectors

Figure 1.6: Requirements for the RICH detector

necessary to consider the CLAS12 momentum range in which the RICH radiator is supposed to provide sufficient angular separation together with a fast photon detection and a good spatial resolution. The only radiator that satisfies the requirements for the opening angle is the aerogel, as shown in Fig. 1.6b. It offers a lower chromatic error and a higher quantum efficiency in the detection of photons in the visible wavelength spectrum. Regarding the photodetection, one affordable solution are the Multi-Anode Photo-Multipliers Tubes (MAPMTs). They have high quantum efficiency in the visible and near UV region, give a fast response and provide the necessary spatial resolution. The CLAS12 geometry introduce some constrains to the detector. It will be placed as substitute of two of the six sectors of the LTCC between the torus cryostat and the Time of Flight and the Calorimeter. The RICH will have a six-sector projection geometry as shown in Fig. 1.6a. The first sector, as shown, will be installed in fall 2017 to start the physics with un-polarized and longitudinally polarized targets, while the second one, that will be placed symmetrically with respect to the beam pipe, will be installed in the near future to extend the kinematical coverage and to control systematic effects in polarized target. Their geometry will be the same. The external frame has a trapezoidal shape, with a major base of about 4.3 m, an height of about 3.8 m and a depth of about 1 m and it is tilted by 65° with respect to the vertical axis. It needs to take into account the residual magnetic field that can be present. As shown in Fig. 1.6c, it should be negligible close to the beam and increasing with the polar angle. The last constraint to take into account is the limited material budget allowed. Considering that most of the RICH material budget will be constituted by the photodetectors, the area they could cover should be reduced and located at small polar angles, where the particles have, on average, higher momentum.

Figure 1.7: RICH hybrid design.

To satisfy all the requirements, an hybrid designed has been developed (Fig. 1.7) [7]. This will allow to reduce the active area from several squared meters to about $1m^2$ and also the costs. The detection will happen in two different ways: directly and reflected. Forward scattered particles with momenta $p = 3-8\,\text{GeV/c}$ and $\theta < 13°$ will be detected directly. The scattered particles with larger angles $13° < \theta < 35°$ and lower momenta $p = 3-6\,\text{GeV/c}$ will have a longer path (about 3 times the direct one) to be detected. First they have to be focused by a spherical mirror. Then the geometry force them to pass through a thinner radiator, be reflected by a planar mirror and to cross one last time the aerogel before detection. Inside the sector the enviroment if filled by nitrogen.

The RICH will provide the required $\pi/p/K$ identification in the momentum range between $3-8\,\text{GeV/c}$ at scattering angles from $5°$ to $30°$ [8]. The benefits of the RICH are presented through the pion/kaon separation and proton/kaon separation in Fig. 1.8a and Fig. 1.8b, respectively. In both figures the top plot shows the total production ratio, the middle shows the inverse of the pion (proton) to kaon rejection factor using the TOF, the HTCC and the LTCC while the bottom one shows the same ratio using also the RICH. At lower momenta ($< 2.8\,\text{GeV/c}$) the TOF is in charge to provide good particle identification; the HTCC will do the same at high momenta ($> 7.0\,\text{GeV/c}$); the RICH will cover the range where the other detectors fail to discriminate the kaons from the other particles: the intermediate one ($3.5\,\text{GeV/c} < p < 7.0\,\text{GeV/c}$). In the plots is possible to see that the $\pi(p)$ contamination to K decrease using the RICH [9, 10].

(a)   (b)
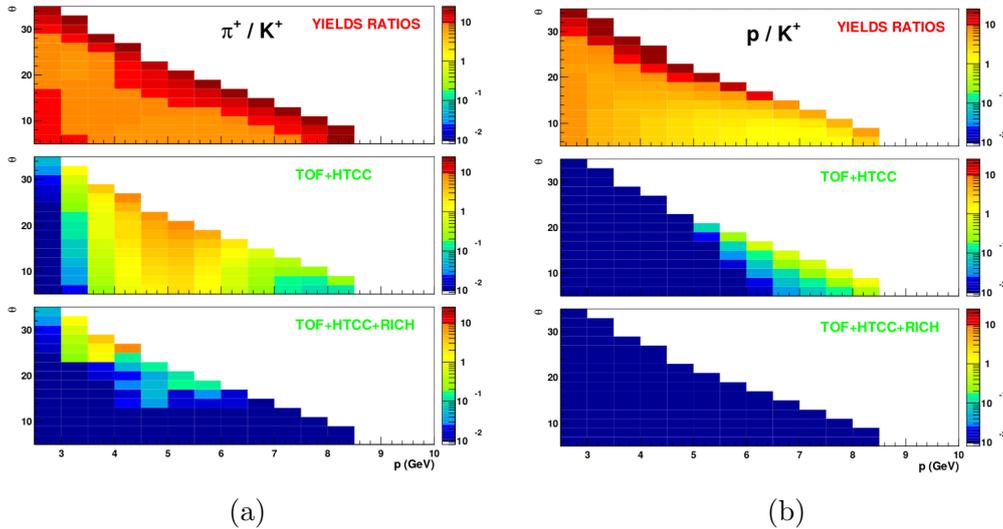
Figure 1.8: RICH detection capacitance.

A brief explanation of each component that compose the detector will be given in the following paragraph.

Radiator

As already introduced, the radiator chosen for the RICH detector is silica aerogel: it is an amorphous solid network of SiO_2 nanosphere with a very low macroscopic density and a refractive index intermediate between gases and liquids. Its production has been performed by a collaboration of Budker Institute of Nuclear Physics and Boreskov Institute of Catalysis in Novosibirsk.

The radiator will need to satisfy stringent requirements in terms of geometry and light transmittance. The first one is that it need to cover a $3.5\,m^2$ area. The refractive index, chosen not to affect angular resolution and photon yield, is $n = 1.05$. The geometry chosen for the tiles that will compose the entire plane of aerogel is squared. In total 92 tiles of aerogel have to be produced with $20\,cm$ side length: 72 tiles $3\,cm$ thick will be used superimposed ($6\,cm$ total thickness) in the large angle region; 22 tiles with $2\,cm$ thickness will cover the proximity focusing region (Fig. 1.9). The tiles that will be placed in the middle of the detector acceptance will be the more demanding ones both in terms of performance and volume carrying. Some of the side tiles will have to be cut into different shapes (trapezoidal or pentagonal) to match the RICH shape. In every case no defect detectable by visual inspection has to be present: the chipping at the edges should not exceed 2% of its own cross-section.

Several tests to investigate the performance and to validate the produced tiles have been made: they were focused on optical performances (transmittance, absorption, chromatic properties, forward scattering), moisture absorption monitoring, geometrical properties (size, surface planarity).

Figure 1.9: RICH aerogel scheme

Mirror

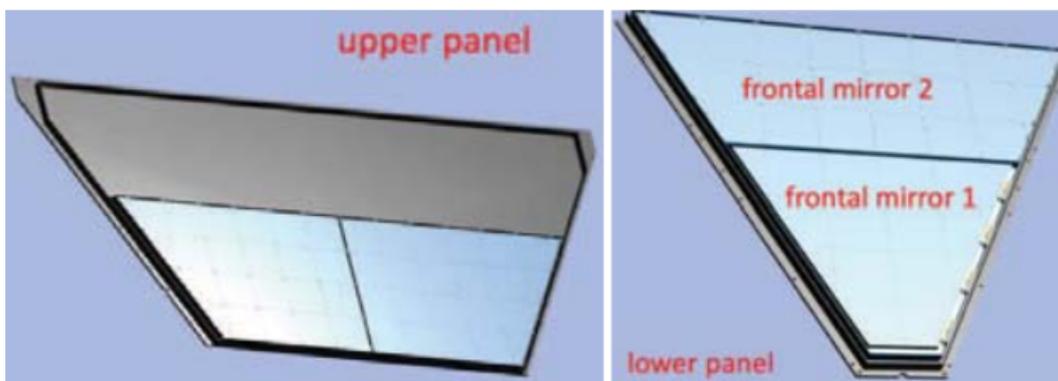The hybrid design foresees a complex mirror system to focus the Cherenkov photons on the active area of the detector. Inside the sector, as sketched in Fig. 1.10, ten spherical mirrors, placed on top of the photon detector, and seven planar ones, before the aerogel tiles, will contain the photons produced at large angles. Two more planar mirrors will be placed in the inner walls on the sides of the module, not to lose any produced photons. The total area of these mirrors will be about $4\,\mathrm{m}^2$.

Together with high reflectivity performance, relevant features to be verified are rigidity and material budget. Rigidity is important to ensure that there will be no deviation from the nominal position during several years of operations. The material budget, instead, is correlated to the necessity to not deteriorate the energy and time measurements of the detector behind the RICH.

The spherical mirrors have been produced by the *Composite Mirror Application Inc* company. This mirror area covers a surface of about $3.5\,\mathrm{m}^2$ and is tilted by $65°$ with respect to the beam axis. Their curvature radius is $4000\,\mathrm{mm}$. Their are made of two carbon fiber layers with a honeycomb core. Compared to the LHCb mirrors, an improvement of about 20% in the areal density has been achieved (the equivalent radiation length is about 1% X_0) [11].

All planar mirrors have been produced by the *MediaLario Technologies* which worked for years with telescope applications. To our knowledge, this is the first time that this technology has been utilized in nuclear physics experiments. The al mirrors are in the CLAS12 geometrical acceptance: they will be made of thin glass layers of $0.7\,\mathrm{mm}$ similar to the carbon fiber mirrors, to obtain an equivalent thickness of about 1% of X_0. The lateral mirrors will have a thicker layer of glass ($1.6\,\mathrm{mm}$).

Photon detector

The third component of the hybrid design is the photon detector. As already mentioned, the active area of the detector has been reduced from the whole sector to $1\,\mathrm{m}^2$ close to the beam pipe. Due to the RICH necessity to do imaging, there are several requirements that have to be satisfied. The area will be covered with multiple photon detectors tiled into larger arrays: the photon detectors must provide a spatial resolution of less than $1\,\mathrm{cm}$ with the minimal dead space. They have to be efficient at single photon level signal detection in visible light wavelengths. Finally, they have to be sufficiently insensitive to the residual magnetic field expected in the RICH position.

Multi-Anode Photo-Multiplier Tubes (MAPMTs) have been chosen as ade-
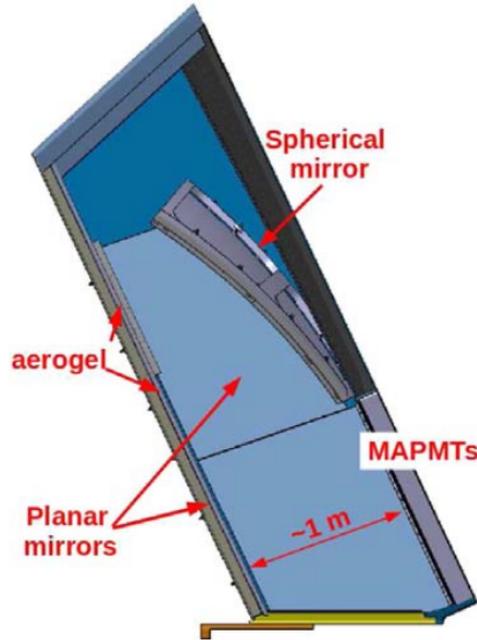
Figure 1.10: RICH mirror scheme

quate compromise between detector performance and cost for the first sector of
the detector. In particular, two devices will compose the active area: flat-panel
Hamamatsu H8500 and H12700. They have an active area of $49.0 \times 49.0 \, \mathrm{mm}^2$
which comprises an 8×8 array of pixels, each with dimensions $5.8 \times 5.8 \, \mathrm{mm}^2$.
The H8500 was the first choice, even if not advertised as the optimal choice for
single photon detection: detailed studies have been performed to characterize
their response and to confirm them as a good choice for the RICH [12, 13].
The H12700 has become available later in time: it is produced with the same
layout of tH8500 and similar gain (typical value is $1.5 \cdot 10^6$ at $1000 \, \mathrm{V}$) but with
optimized dynode structure for single photon detection. For the second sec-
tor, that will be installed in the near future, Silicon Photo-Multipliers (SiPM)
matrices have been considered as cost-effective solution in conjunction with
the same readout of the MAPMTs. Since those sensors are the subject of this
thesis, more information will be provided in the following chapters.

Electronics and readout

The choice to have MAPMTs as photon detectors implies to have a total num-
ber of about 25600 independent channels. An highly integrated -end electronics
with modular design becomes necessary. The component main requirements
are described here:

27

- **material budget** limitation in terms of background and particle straggling both for the RICH and for the detectors behind it;

- **geometry** limitation since it has to cover the photon-detector area at maximum and has to have a total thickness of 10 cm:

- **number of channels** needs to match the number of independent anodes (25600);

- **single photoelectron (SPE)** sensitivity is required. The minimum detectable charge is at the level of few 10^6 electrons;

- **trigger rate and dead time** are expected to be of 20 kEvents/s and smaller than few %, respectively;

- **trigger latency** has to be maintained as the value of CLAS12 which is 8 μs. This implies that the electronics must keep track of events that occurred in the 8 μs before the arrival of the trigger;

- **time resolution** is correlated to the temporal development of the MAPMT signal and could allow to disentangle the direct and reflected photons, whose time difference is about 6 ns, keeping into account that the difference in traveling distance is 2 m or more. A time resolution of the order of 1 ns would help the reconstruction strategy;

- **anode gain compensation** could be accessible via electronics modules to reduce the gain dispersion of the MAPMT;

- **crosstalk** between adjacent electronics channel is expected to be at a level of 1% to be smaller than the photodetector crosstalk.

A modern readout electronics architecture that fits these requirements consists of -end cards with dedicated Application Specific Integrated Circuit (ASIC) configured, controlled and readout by programmable devices such as Field Programmable Gate Array (FPGA) directly connected to them. The ASIC chosen for this detector is the 64 channel MAROC [14] (Multi Anode Read Out Chip) manufactured by *Omega Group* of LAL (Paris, France). The final design (Fig. 1.11) for this component uses two PCB layers behind each set of MAPMT sensor. The first layer will host the ASIC front-end and will be connected through a passive adapter board to the MAPMTs, while the second will house the FPGA to configure, manage and acquire two or three ASICs and the low voltage distribution. Data are transmitted via optical lines, minimizing the wiring and therefore the material budget.

The MAROC has been originally designed for the ATLAS Luminometer in AMS 0.35 μm CMOS technology and consists of 64 independent channels. It provides both the analog and digital information of each channel. The analog

signals allow for charge measurements and will be only used during calibration procedures in dedicated runs, because of the latency in the readout of the signal. The digital information will be the one used during the physics runs, since it is promptly available for each channel in parallel and can be sampled with a predefined clock.

Several tests on this electronics have been done to evaluate performance and radiation hardness. All the boards for the RICH have been produced and installed on the detector.

(a) Readout Scheme   (b) MAPMT double tile readout
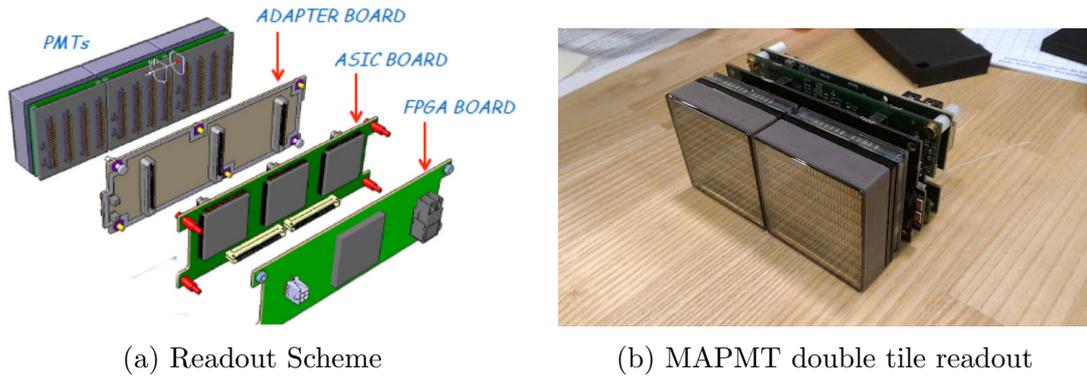
Figure 1.11: RICH active area: photon detector and readout electronics

1.4 Conclusions

The CLAS12 RICH is designed for the identification of the products of the semi-inclusive deep-inelastic scattering of the JLAB 12 GeV polarized electron beam off polarized nuclear targets [15]. This kind of processes is important to study the tridimensional structure of the proton, in particular the parton transverse momentum degrees of freedom. The RICH, providing access to the quark's flavor, will contribute to the momentum tomography of the fundamental brick of the known matter.

Chapter 2

CLAS12 RICH Photo-Counters

Cherenkov radiation is the phenomenon generated by a particle traveling in a transparent medium when its velocity exceeds the speed of light in that medium. It is observed as a cone of light with a specific opening angle, called Cherenkov angle, which can be used to infer the particle identity (mass) when knowing its momentum. In particular, looking at the quantum mechanical picture, the movement of a charged particle inside a polarizable medium excites the molecules to higher level states. When they return back to the ground state, they re-emit photons as electromagnetic radiation. This behaviour implies that in the RICH detector the leading actors are photons. The measure of the Cherenkov angle is challenging because the number of emitted photons is so limited that the photon detector has to be sensitive to a single quantum of light. The aim of this chapter is first to offer an introduction of the photon's interaction with matter and, later, to bring the attention on photon detectors suitable for Cherenkov applications. In this work, two different types of sensors are discussed because a mature technology has been chosen for the first RICH sector but an innovative approach is under consideration for the second one. Here a comprehensive description of their design, properties and performance parameters is given as an introduction. The study done as part of the author's work is presented in the following chapters.

2.1 Electromagnetic radiation

Photons are elementary particles with no mass and charge. They are quanta of electromagnetic energy that exhibit both wave-like and particle-like properties. Their interaction with the matter is unique and not ascribable to other charged particles. They are not subject to the Coulomb or nuclear forces but they interact only in localized and discrete interactions. As a consequence, a beam

of photons, propagating through any material, will be attenuated in intensity but the energy will remain constant. Due to the small cross section of these interactions, the intensity attenuation in the interaction with matter can be described as

$$I = I_0 e^{-\mu x}.$$

The transmitted intensity, I, is calculated as a function of the incident intensity, I_0, it depends on the thickness of the material, x, and on the linear attenuation coefficient $\mu = \eta_A \sigma_{tot}$, that is given by the product of the number of atoms per units of mass η_A times the total cross section of the interactions σ_{tot} [16]. Fig. 2.1 shows the photon attenuation as a function of the photon energy and highlights the different components of the mechanism of the interaction:

- photoelectric effect;

- compton scattering;

- pair production.

At low energies ($E_\gamma < 0.1$ MeV) the photoelectric effect dominates, while the Compton scattering is important at intermediate energies and the pair production dominates at the highest photon energies and has an absolute threshold of 1.022 MeV, that is equal to the mass of the produced pair.

Photoelectric Effect   The photoelectric effect (Fig. 2.2a) was originally described by Einstein to establish the quantized nature of light. During the process a photon is converted into a single photoelectron. In particular the process can be described as follow: the photon interacts with an atom and it is absorbed completely; its energy is transfered to an electron that emerges with kinetic energy $E_{e^-} = h\nu - BE$ that corresponds to the photon energy ($h\nu$) minus the portion that has been used to overcome the binding energy (BE) and remove the electron from the atom. This effect is most probable when the binding energy of the electron is slightly lower then the energy of the incident photon.
This interaction leaves the atom in an excited state creating a vacancy in one of the electron shells. When an orbital electron moves to fill in, it can emit a characteristic x-ray photon, depending on the binding energy of the electron involved. This process is usually called flourescence.

Compton Scattering   A Compton scattering (Fig. 2.2b) occurs when the incident photon interacts trough an inelastic scattering with an electron.
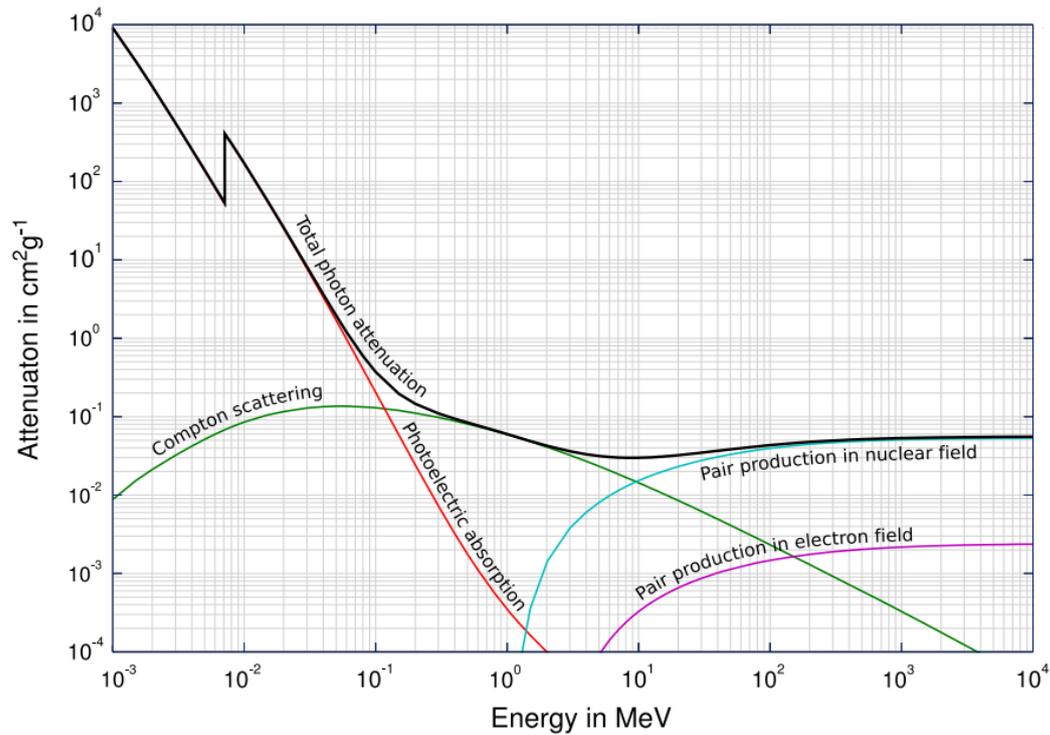
Figure 2.1: Total photon cross sections [17].

The photon energy is usually high with respect to the binding energy of the electron so that the latter can be considered "free". The resulting electron energy depends on the scattering angle and on the original photon energy.

Pair Production   This process (Fig. 2.2c) involves a photon that interacts with an electron or a nucleus producing a positron-electron pair. This is a threshold process: the incident energy has to be higher than 1.022 MeV. In Fig. 2.1, at the higher energies are visible the two components of this process: the interaction with an electron or the one with a nucleus. Conservation of energy and momentum in the Coulomb field causes the pair of electrons to move forward along the initial direction of the photon with a small opening angle. The pair of particles will interact with the electrons and nuclei in the remaining material and will radiate photons. If the energy of the produced photons is still higher than the threshold, the same pair production process can occur again. This mechanism is frequently used to determine particle energies in the electromagnetic calorimeters from the developed showers. Each of these interactions occurs in particular conditions of the incident photons as

(a) Photoelectric effects   (b) Compton scattering   (c) Pair production

Figure 2.2: Pictorical examples of photon interaction with matter [18].

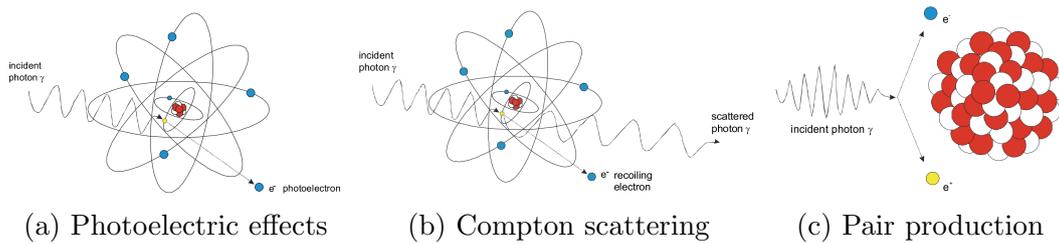well as of the material. In fact, a not negligible role is played by the energy, by the scattering angle of the photons and also by the atomic number of the atoms involved. These features have to be taken into account while working on the applications of these phenomena.

2.2   Introduction

The technology of light detection is a powerful tool that exploits the present understanding of the above described phenomena such as the photoelectric effect. Photodetectors or light sensors allow to do measurements with unique advantages: nondestructive analysis, high-speed properties and high detectability. Several scientific fields use this technology to improve their measurements: medical diagnosis and treatment, spectroscopy, biotechnology and high energy physics, as examples.
In this thesis the focus will be on high energy physics and in particular on RICH detector requirements.
As previously introduced, photon detection involves an incident photon that interacts with the material and, in particular, with the electron.
The ideal photon detector should provide a response proportional to the incident photon flux. This implies that the small perturbation that occurs inside the target material with the extraction of an electron could be amplified to ease the operation of yielding a signal to be recorded. Usually it is a quantized mechanism: the single incident photon generates a single response from the element of the detector. There are different kinds of photon detectors:

- photomultiplier tubes,
- photoemissive sensors,
- photodiodes (silicon detectors),
- photoconductors.

Each of them have characteristic mechanical features that have to be taken into account because they can affect the voltage level or the current flow obtained

as a result of the photon interaction. This means that any readout electronics or display device has to be calibrated exactly for the specific kind of photon detector. Moreover, it is not to be underestimated that the output signal of a photon detector is strongly dependent on the wavelegth of the incident light. There is a critical wavelength, the so-called cut-off wavelength, beyond which the photoresponse decreases abruptly: it can correspond either to the bandgap of the semiconductor material or to the activation energy of defect states.

Two different photon detectors have been chosen for the RICH detector of the CLAS12 experiment: PhotoMultipliers Tubes (PMTs) and Silicon PhotoMultipliers (SiPMs). The first ones are already in use for the first RICH sector, while the others are under consideration to be used in the future in the second sector. The work of this thesis is focused on the features they share in high energy physics application. An introduction of their design and of their main properties will be done in this chapter, while a detailed analysis on these devices will be presented in the following chapters.
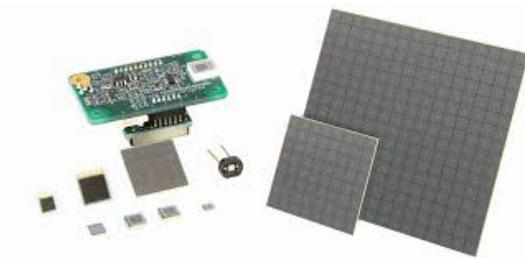
(a) PMT   (b) SiPM

Figure 2.3: Examples of PhotoMultipliers Tube and Silicon PhotoMultipliers.

2.2.1 History

The first observation of the photelectric effect happened back in 1839 by Becquerel [19]. He noticed that when one of a pair of electrodes in an electrolyte was illuminated, a voltage or a current resulted. Later in 19th century, a further confirmation of the photoelectric effect was reached experimentally by Hertz, with the exposure of a negative electrode to ultraviolet radiation, and by Elster and Geitel, producing a forerunner of the vacuum phototube with visible light striking an alkali metal. From then, many photoemission experiments have been made by several scientists until Einstein postulation that the

light can be considered both as a wave and as a particle (quanta) has been proven (Millikan's experiment or Compton scattering measurement) and accepted by the whole community of physicists.

These discoveries helped the development of several photocathodes with high sensitivity extending from the infrared, through the visible, to the ultraviolet region thanks to the application of different kind of materials.

The technological improvement of the photocathodes helped also the rapid progress of the photomultiplier tubes. The first half of the 20th century has been the scene for several studies about secondary emissive surfaces (dynodes) to reach higher performance in secondary electron emission and in electron multiplication. The starting point saw the production of a photocathode coupled with single-stage dynode (triode photomultiplier tube). Afterwards the development of a new photomultiplier tube started: it was based on the introduction of different dynode stages with an electric and a magnetic field to enable the electrons to accelerate. Finally, this brought to a technology stage that is currently used, that consists in an electrostatic-focusing type photomultiplier tube. Always improving photomultiplier tubes have been developed along the years with intensive studies of all the components of the device: dynode geometric structure and material, cathode and anode material or magnetic-focusing types of multipliers.

The PMTs carry some practical disadvantages such as fragility, limited rigidity of the multi-electrode dynode chain or the vacuum-tight requirement of enclosure. Several improvements have been done along those years of research but some definitive features like the already named fragility could not be solved and leave the PMT as a device difficult to be qualified for specific enviroments like space o biomedical research.

An alternative to the PMTs started to be developed in the '60s as a solid-state replacement for the single photon detection: the semiconductor photodiodes [20]. In particular, silicon photomultipliers (SiPMs) are based on reversed biased PN diodes and can directly detect light from near ultra violet to near infrared. This rapidly improving technology offers an attractive alternative to PMTs: SiPMs provide a combination of low light detection capability with the benefits of a solid-state sensor such as mechanical robustness and uniformity of response. Several studies are still on-going to improve the performance of this technology in order to use SiPM for light detection in different scientific enviroments.

The technologies at the base of these photon detection devices will be introduced in the following part of this chapter.

2.3   Design

The two devices chosen to be installed in the CLAS12 RICH, even if at different moments of the detector's life, share the common goal of photon detection and the principle of operation related to the photoelectric effect. The two technologies are however quite different and will be introduced separately in the following part.

2.3.1   PMT

The interaction of an incident photon with a photomultiplier tube is schematically shown in Fig. 2.4. It operates following few steps:

1. the photon passes through the input window and hits the photocathode;
2. in the interaction with the photocathode, photoelectrons are emitted due to the photoelectric effect into the vacuum;
3. the focusing electrode focuses and accelerates the photoelectrons onto the first dynode;
4. secondary emission occurs from the first dynode as for all the following dynodes;
5. the multiplied secondary electrons emitted from the last dynode are collected by the anode;
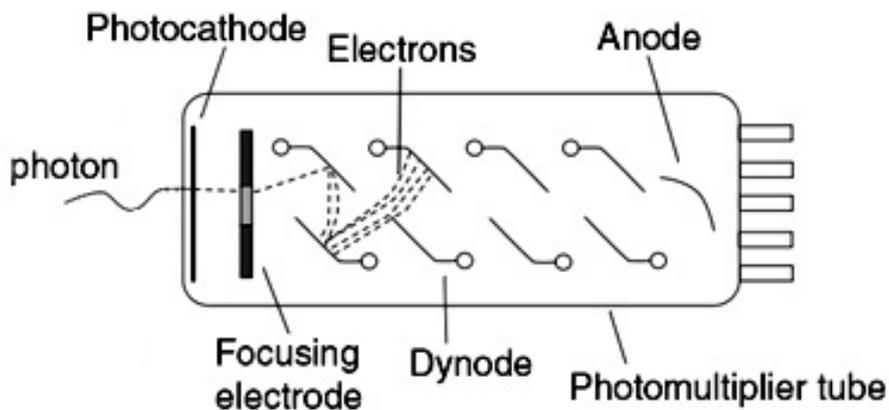6. the signal is later extracted from the anode.

Figure 2.4: Schematic representation of a photomultiplier.

Photocathode   Having a look at the energy band models of the photocathode, it is possible to understand why it is important to choose the proper

material correlated to the application of the devices. A description of this
model will be done following the schemes in Fig. 2.5:

- The **valence band** is the band occupied by the valence electrons.

- The **conduction band** is the band where the electrons, so-called con-
  duction electrons, can move freely. It is normally empty.

- The **Fermi level** does not correspond to an actual energy level, but it can
  be considered as an hypotetical energy level that at the thermodynamic
  equilibrium would have the 50% probability of being occupied by an
  electron.

- The **work function** ϕ is the necessary energy to free an electron from
  the nucleus.

- The **vacuum level** is defined as the sum of the work function and the
  Fermi level of the material. It refers to the energy of a free stationary
  electron that is outside of any material.

- The **energy gap (EG)** is the forbidden-band gap that can not be oc-
  cupied by electrons.

- The **electron affinity (EA)** is an interval between the conduction band
  and the vacuum level.

(a) Alkali   (b) Semiconductor

Figure 2.5: Photocathode band models.
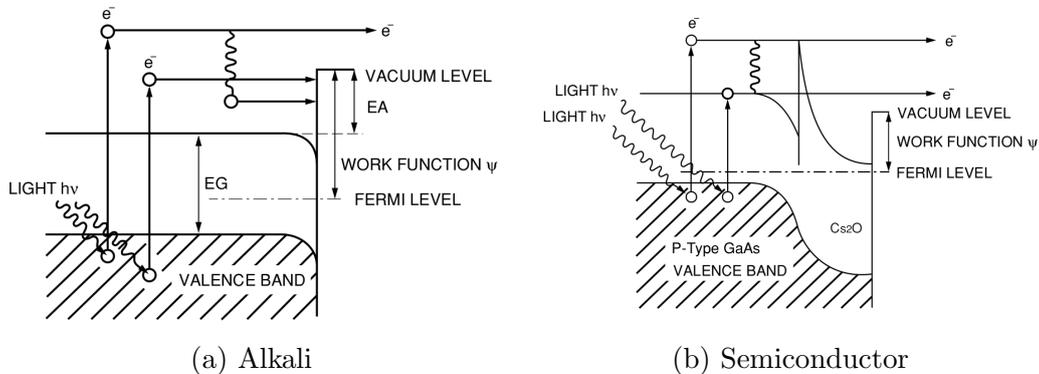
When the photon strikes the photocathode, the electrons in the valence band
absorbe its energy ($h\nu$) and become excited. If they have enough energy to
overcome the vacuum level barrier, they are emitted as photoelectrons in the
vacuum. It is possible to define a probability for this process through the
ratio of the number of output electrons to the number of incident photons by

defining the quantum efficiency $\eta(\nu)$ [21]:

$$\eta(\nu) = (1 - R)\frac{P_\nu}{k} \cdot \left(\frac{1}{1 + \frac{1}{kL}}\right) \cdot P_s$$

The parameters are:
- $R \rightarrow$ reflection coefficient;
- $k \rightarrow$ photons full absorption coefficient;
- $P_\nu \rightarrow$ probability that the absorbed light may excite electrons to a greater level than the vacuum level;
- $L \rightarrow$ mean escape lenght of the excited electron;
- $P_s \rightarrow$ probability that excited electrons become photoelectrons;
- $\nu \rightarrow$ frequency of light.

The parameters correlated to the chosen material are R, k and P_ν. If it is chosen properly, then the quantum efficiency will be dominated by L and by the P_s parameter that is correlated to the EA.

The difference between the two shown photocathodes in Fig. 2.5 is that the use of semiconductors allows to apply on the photocathode itself a surface layer of electropositive material (Cs_2O). This creates a depletion layer that forces the band structure to bent forward. This state is called negative electron affinity (NEA) and increases the P_s probability that the excited electron reaching the photocathode surface may be emitted.

Electrode   The arrangement of the focusing electrode is as much important as all the other components. It is very decisive that the emitted photoelectrons are carried to the first dynode in order to have the highest collection efficiency with the lowest transit time. This collection efficiency is defined as the ratio of the number of electrons landing on the effective area of the first dynode to the number of emitted photoelectrons. As a general rule, the electron movement in the photomultiplier tube is influenced by the electric field that is dominated by the electrode configuration, its arrangement and the voltage applied. Several numerical analyses have been performed to predict the electron trajectory and optimize it.

Dynodes   New simulations have been implemented to improve the performance of the dynode chain. In fact, a photomultiplier is usually constructed with several to more than ten stages of secondary-emissive electrodes (dynodes). Each one of them should have, as the first one, high collection efficiency, low transit time spread and it has to allow the best trajectory of each generated electron (as shown in Fig. 2.6b). The optimum dynodes has to be chosen according to the application of the photomultiplier. It is made, as shown in

Fig. 2.6a, of an emissive surface coated onto a substrate electrode. Usually the material for the electrode are nickel, stainless steel or copper-beryllium allow. The options for the secondary emissive material are alkali antimonide, beryllium oxide (BeO), magnesium oxide (MgO), gallium phosphide (GaP) and gallium arsenide phosphide (GaAsP). The decision of the material influences the number of secondary electrons emitted per primary electron. Ideally the amplification (gain) of a PMT with a defined average secondary emission δ per stage and n dynode stages is expected to be δ^n.

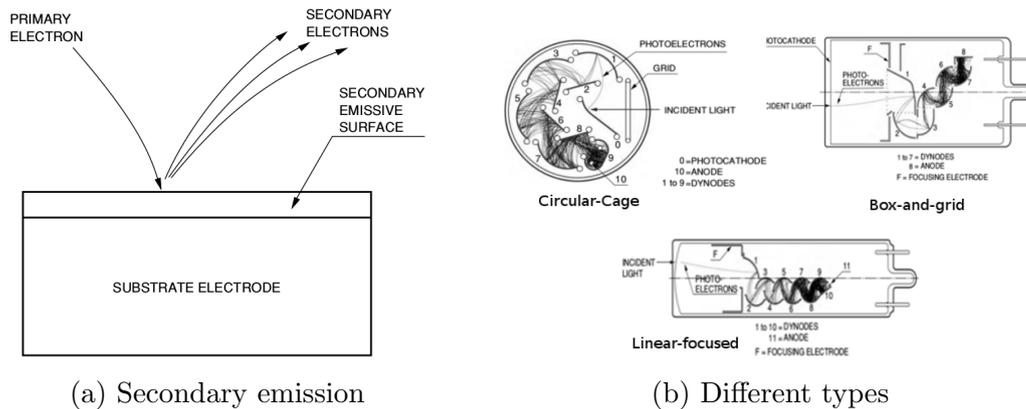(a) Secondary emission   (b) Different types

Figure 2.6: Dynode scheme.

Anode   The anode is the last electrode of the chain of dynodes. Its goal is to collect secondary electrons multiplied in the cascade and output the electron current to an external circuit. It has to be designed accordingly to the dynodes structure. Usually it is fabricated in the form of a rod, plate or mesh electrode. It has to have also an optimized potential difference with respect to the last dynode in order to have the largest output current possible.

2.3.2   MAPMT

The MultiAnode Photomultiplier Tube (MAPMT) has been chosen as photon detector for the first RICH sector (Fig. 2.7). They are flat panel type multianode PMT assemblies of the H8500 and H12700 Hamamatsu series and feature $52\,mm^2$ area, bialkali photocathode, 8×8 multianode matrix with a 6 mm pixel pitch. The first model, named H8500, was originally developed for position sensitive scintillation counting in molecular imaging studies (PET and mini-gamma cameras) [22]. Several studies performed on them allowed to validate their use at single photon level [23, 24]. The second model, named H12700, has been lately developed following the high demand from high energy

physics groups [25, 26]. It differentiates from the first one thanks to an higher first stage accelerating field and a revised collection geometry optimized for single photon detection [27].

(a) H8500

(b) H12700

Figure 2.7: RICH MultiAnode Photomultiplier Tube.

Here just a quick introduction on their structure is provided. Following the sketch in Fig. 2.8, the photoelectrons emitted from the photocathode pass through the focusing mesh and are directed to the first of the metal channel dynode, then, while being multiplied, they flow to the other dynodes until they reach the multi-anode structure. This configuration is typical for position-sensitive photomultiplier tubes. The so-arranged dynodes provide wide dynamic range, high gain and high position resolution. Moreover, since they are assembled in close-proximity to each other, they allow to have the minimum spatial spread in the avalanche of multiplied electrons ensuring low crosstalk during secondary electron multiplication and compact size of the whole device.

2.3.3   SiPM

The Silicon Photomultiplier (SiPM) is a solid-state single-photon-sensitive device that integrates a dense array of avalanche photodiodes (APDs) on a common substrate of silicon.

Before providing insights on SiPM and APD properties, an ovelook on their operation principles may be useful. A pure crystalline silicon is characterized by having the same amount of positive (holes) and negatives (electrons) charge carriers. Silicon photodiodes are built with a PN junction in the pure structure. This operation is done by doping a portion of the material with electron donors (from the group V of elements) and the other portion with electron acceptors (from the group III of elements). The first one will become a N-region with negative electrons as majority of charge carriers while the second one
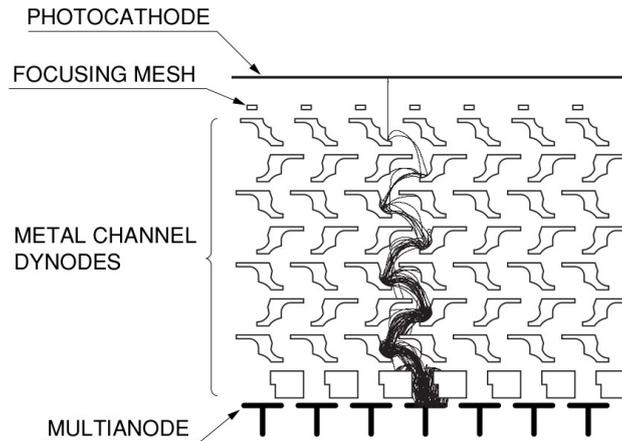
Figure 2.8: MAPMT dynode structure scheme with electron trajectories.

will become a P-region with positively charged holes as the majority charge carriers. Once the junction is formed, a diffusion current appears due to the holes and electrons recombination neutralizing each others' electrical charge. This process empties the layer adjacent to the junction on each side of the two regions: this forms the so-called depletion layer where opposite charges have been recombined and have been neutralized. Electrons and holes in the positive and negative side respectively turn the N-side of the depletion layer to have a positive potential and the P-side to have a negative one, with an electric field across this region that has a negative polarity. The N-region can be define as the cathode and the P-region as the anode. The convection of the electric field will go from the cathode to the anode (Fig. 2.9a). As in the PMTs, a current across the junction can be induced by an external source of energy that disturbs the equilibrium in the depletion region. This could be the thermal agitation or the photoelectric effect if the incident photon can provide enough energy to an electron to transit from the valence to the conduction band as shown in Fig. 2.9b. The excesses of electrons and holes drift in opposite directions towards their majority sides (N for electrons and P for holes). For more than one electron-hole pair traveling through the depletion region it is possible to start talking about a photocurrent.

The photosensitivity and frequency response of the photodiode is affected by the depth of the depletion region. As presented in Fig. 2.9c, longer wavelengths (red) are absorbed at deeper depth of the silicon with respect to the short ones (blue). A depletion layer deep enough into the silicon could help to increase the photosensitivity in a wider wavelenght range and also to decrease the capacitance of the junction. For the application in which a broad photosensitivity is requested, it is possible to reverse the bias of the PN junc-

(a) PN junction scheme at the
equilibrium

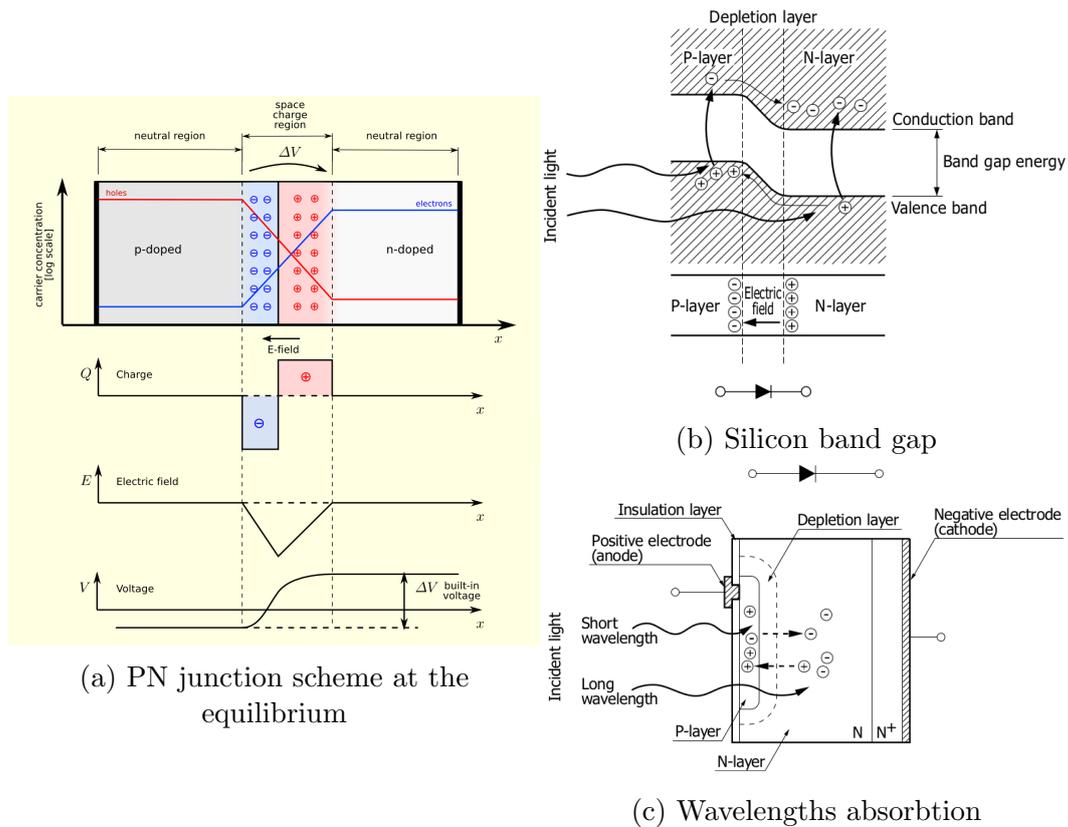(b) Silicon band gap

(c) Wavelengths absorbtion

Figure 2.9: Operation characteristic of a PN junction [28].

tion to increase the depletion region. The N-region (cathode) will be biased
with an higher electric potential than the P-region (anode). Increasing the re-
verse voltage has different correlated benefit for this technology. First, it helps
increasing the depletion layer, to have it as deep as the photodiode's bulk sil-
icon. This also prevents the photoelectrically generated carries to diffuse and
neutralize before being collected. Moreover, it intensifies the electrical field in
the depletion layer. This reflects in an increase of the kinetic energy gained
by the accelerated carriers in between scattering collisions with atoms in the
lattice. With enough energy to overcome the energy gap between consecu-
tive collisions, some carriers are likely to ionize lattice atoms and release upon
impact at least one electron-hole pair into the conductive and valence band,
respectively. This latter effect constitues a carrier multiplication phenomenon
resembling an avalanche in which the number of carriers increases rapidly. This
avalanche process, called Geiger Mode (GM), is the one that generates the fi-
nal signal to be readout as the evidence that an interaction with an incident
photon has occurred. The minimum reverse voltage that allows this multi-

plication process is called Breakdown Voltage (V_{bd}). As already mentioned, a SiPM, also known as multi-pixel photon counter (MPPC), is a common-bias and common-output matrix of micro-cells, each of them being an independent Geiger Mode Avalanche Photo-Diode (GM-APD) connected in parallel. Each micro-cell detects photons identically and independently. Fig. 2.10 illustrates the layout of the micro-cells of different pitch sizes, that can compose a SiPM.

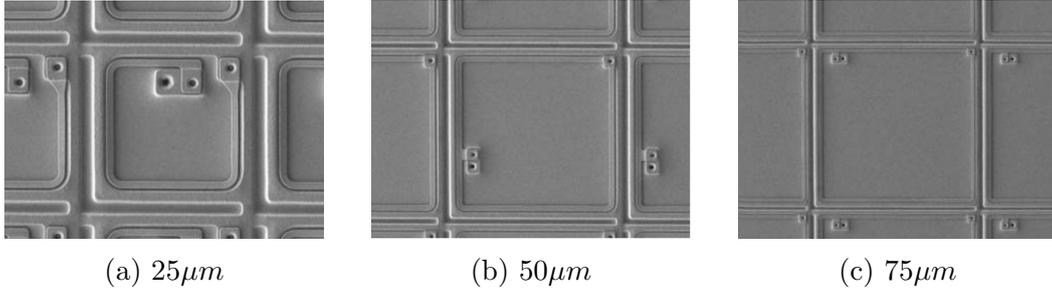(a) $25\mu m$ (b) $50\mu m$ (c) $75\mu m$

Figure 2.10: Individual micro-cell layout for different pitch sizes.

In Fig. 2.11, instead, is shown the equivalent circuit of a GM-APD. In the circuit, C_d is the diode capacitance in reverse bias, R_s is the silicon substrate resistance and R_q is the quenching resistor, with $R_q >> R_s$ [29]. It will help during the introduction of the three main operation modes:

1. **Quiescent Mode**: the diode is first reversed biased at $V_{bias} = V_{bd} + V_{ov}$ where V_{ov} is the excess beyond V_{bd} called overvoltage. This basically is the situation when the switch is open in the circuit and no current is flowing.

2. **Discharge Phase**: when the photon strikes, an avalanche multiplication starts inside the GM-APD. The switch closes and C_d discharges through the series resistance R_s, whose value is reduced by the avalanching carrier population. This brings the current flow to increase and the potential difference across C_d (V_d) to exponentially decay from V_{bias} to V_{bd}, weakening the avalanche process but not stopping the current flow in the device.

3. **Recovery Phase**: when V_d reaches V_{bias}, R_q is large enough so that the current flow can not sustain the C_d's discharge and the avalanche process is quenched. The switch opens again; C_d is recharged back thanks to R_q; back in the quiescent mode, the device is ready for a new photon. The quenching process is necessary because when the corrent starts to flow, no discrete output pulses could be detected without a stop. Once the photoelectron event can lead to a succeeding output pulse (gain and

amplitude) the resistance R$_q$ helps to end the avalanche. During the recovery time the device is unavailable to detect a new photoelectric event. The latter is the main reason why they have been arranged in matrices for light detection applications.
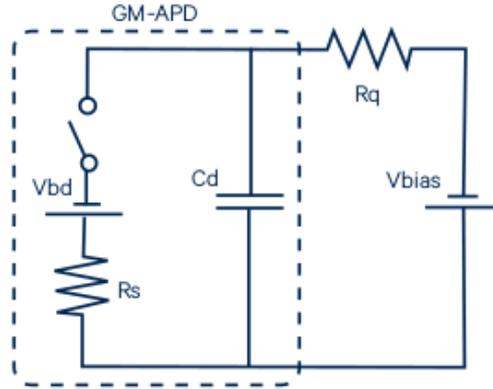

Figure 2.11: Equivalent circuit of a GM-APD.

To measure the sensitivity of a SiPM, or alternatively, to calculate the probability that a photon arriving on the SiPM surface is detected, producing an output pulse, it is necessary to introduce the Photon Detection Efficiency (PDE). It is different from the PMT's quantum efficiency because it has to consider the micro-cell structure. Generically it can be described as the ratio between the number of detected photons over the number of incoming photons, but it has to take into account the features of the device. This is the reason why is defined as

$$PDE(\lambda, V_{ov}) = \eta(\lambda) \times \varepsilon(V_{ov}) \times FF$$

- $\eta(\lambda)$ is the quantum efficiency of the silicon: it is function of the wavelength and of angular incidence of incoming photons; it is the probability that an incident photon is transmitted to the silicon, absorbed and finally converted in an electron/hole pair. To increase the efficiency it has to be as high as possible: anti-reflecting coating layers deposited over the active area are helping to reach the value of ~ 0.98.

- $\varepsilon(V_{ov})$ is the avalanche initiation probability: the generated electron/hole pair initiates a self-sustaining avalanche process. It is correlated with the electron/hole ionization rates dependence on the induced electric field and on the wavelength of the incoming photon. This means that it is a function of V_{ov} and of the wavelength, too. To maximize it, the internal

junction structure and the electric field can be optimized as a function of the applications.

- *FF* is the fill factor of the device or geometry efficiency: it is due to the fact that the micro-cells necessarily have some dead area on their periphery. These areas accomodate isolating structures and signal routing's metal lines, see Fig. 2.10. They have to be minimized in order to increase the fill factor: advance lithography tecniques and clever device layout are the options to achieve it [30]. Its values range from $\sim 30\%$ to $\sim 80\%$, with the larger value for the larger size of a microcell [31].

2.4 Photon Counting

Inside the RICH detector the working conditions of the photon detector are defined as single photon ones: the incident light is very low with negligible probability to have more than one photoelectron in the same readout channel within the time resolution of the device. An introduction of the working principles of both devices will be done in this section. They will be approched in parallel since all the work on them will be presented in the same way.

MAPMT

A description of the readout process will be introduced in the following lines and in particular the single photon counting approach will be explained. The two most important quantities to keep in mind during this kind of work are:

- *Collection efficiency* it is the probability that the photoelectrons emitted from the photocathode will impige on the first dynode. Or, introduced differently, it is the ratio between the number of photoelectrons emitted from the photocathode with the number of incident photons per unit time.
- *Detection efficiency* it is the ratio of the number of counted output pulses to the number of incident photons.

They are correlated through the following relation:

$$\mathrm{Detection\,Efficiency} = \frac{Nd}{Np} = \eta \cdot \alpha$$

where Nd are the counted pulses, Np are the incident photons, η is the photocathode's quantum efficiency and α is the dynode's collection efficiency. They allow us to understand how the mechanical features of the device are correlated to their performance.

Fig. 2.12 shows a scheme of the readout signal: the pulse height is proportional to the amount of charge accumulated at the anode after the cascade process.
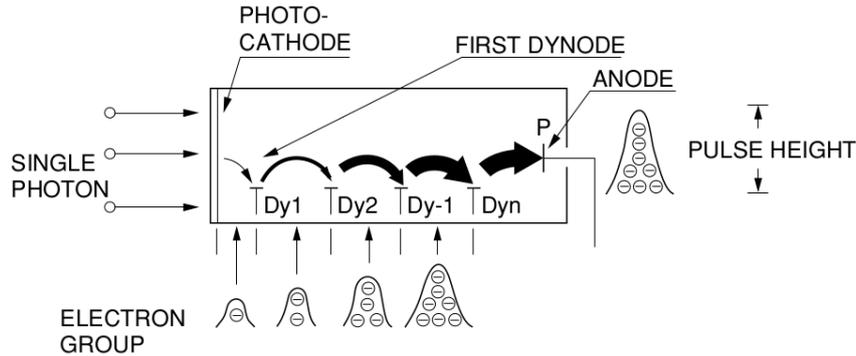

Figure 2.12: PMT operation in photon counting mode [21].

Two are the methods to process the signal: analog and digital mode. Their use depends on the light intensity and on the bandwith of the output circuit. By observing the output signal with an oscilloscope it is clear how they differentiate. At higher light level the output pulse intervals are narrow and they overlap each others in one analogue waveform while lower light level allows to see discrete pulses that can be counted in a digital mode. The latter is exactly the photon counting, and it is the one on which this work will concentrate on. The output pulses exhibit a certain distribution in the pulse height because of fluctuations in the multiplication at each dynode stage due either to the dynode position or to the electrons deviating from their nominal trajectories. Fig. 2.13a shows on top an example of pulse height distribution. It provides a direct information of the collected charge, hence information on the incident radiation intensity. In the bottom the single anode output pulses are ordered as a function of the arrival time on the vertical axis with their pulse height on the x-axis. A proper readout electronics allows to record each pulse overtaking a given threshold with an assigend timestamp. Without a sophisticated analysis, i.e. exploiting the time over threshold information, overlapping photons can not be resolved. This illustration helps to compare the analog (top) and digital (bottom) way to process the signal.

SiPM

The SiPM device is a matrix of equal micro-cells. Each one of them has the duty to detect a single photon. When N photons arrive on the surface of the device they hit N different micro-cells producing N single-cell signals. The integrated SiPM output pulse is N-times larger than the single-cell response and

is also correlated to the overvoltage chosen to operate. Fig. 2.13b illustrates on top the single-cell signals. On the bottom, the analog pulse amplitde ditribution is shown both for individual photons and for the SiPM integrated output. The plot shows on the y-axis the output voltage measured: it is an arbitrary choice as the output current is often plotted as well. The amplitude and the

(a) MAPMT   (b) SiPM
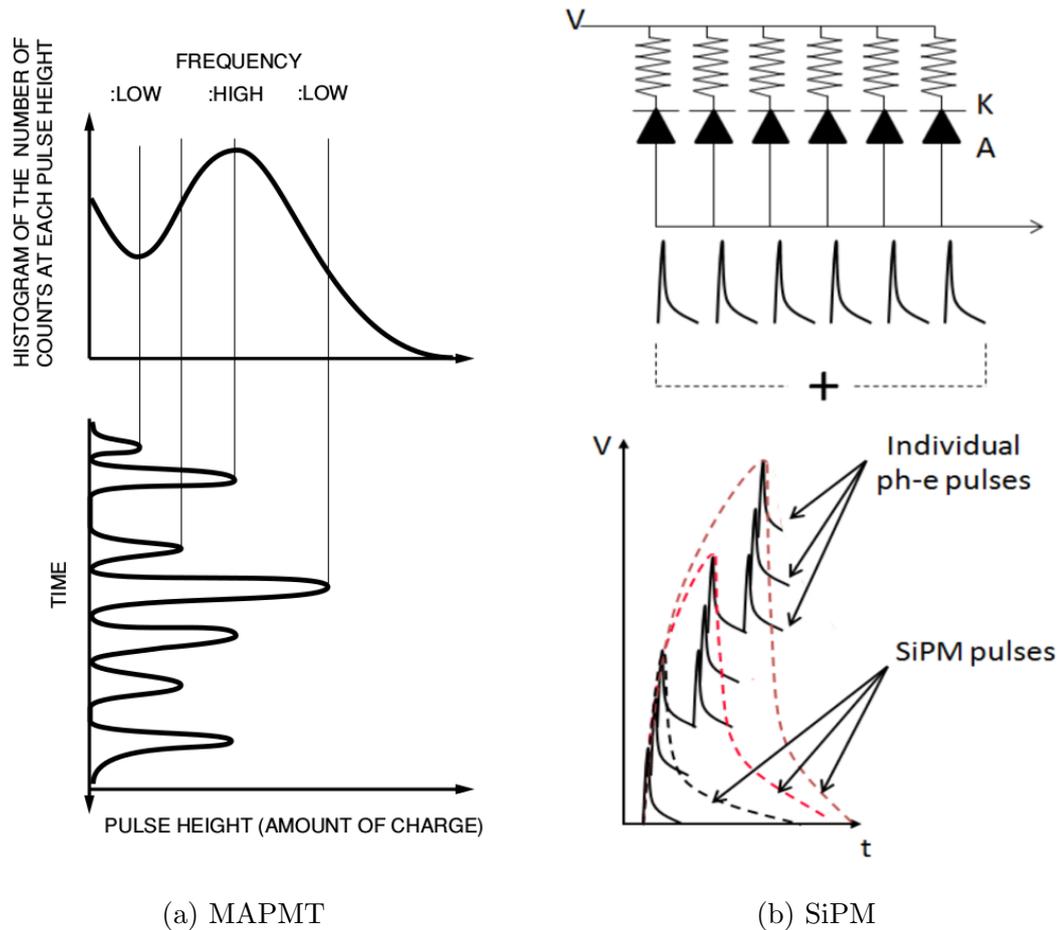
Figure 2.13: Photosensors output distribution

area of these SiPM pulses are proportional to the number of detected photons if the incoming light is low enought not to occupy all the micro-cells. In fact, if the signal is larger, saturation occurs and the proportionality is lost together with the information about the incoming particle flow. More examples of the readout signals are presented in Fig. 2.14. A brief description of all the cases is provided in the following lines.

- **2.14a** Single-cell signal. Its shape depends mainly on the three elements, shown in Fig. 2.11, C_d, R_s and R_d. The rising edge corresponds to the

discharge phase (when the photon strikes), while the trailing edge is the recovery phase with time constat $C_d \times R_q$.

- **2.14b** Simultaneous firing of several cells. The orange curve reports the same single-cell signal of 2.14a, while the blue one is the integrated SiPM pulse.

- **2.14c** Not concurrent cells firing. It is called pile-up of pulses. Several (three in this case) micro-cells fire at different times. Their signals integrate into the SiPM output, but since they were not coincident, they do not perfectly overlap. The area is still proportional to the number of detected photons.

(a) Single-cell firing   (b) Multi-cell firing   (c) Pile-up
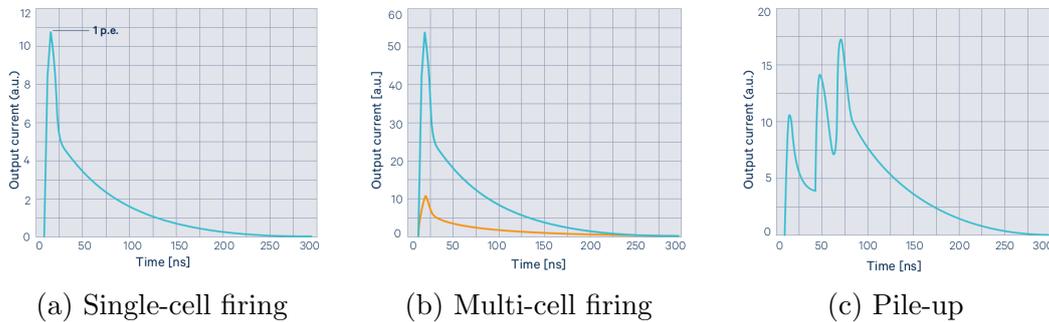
Figure 2.14: Example of a current pulse produced in response to photon absorption [29].

Similarly to the PMT, the analog information of this kind of signals allows to have a direct information of the original light intensity through its deposited charge.

2.5 Performance Parameters

In this section a quick review of some of the main parameters that can be investigated to understand the way the photon detector works are introduced. This presentation has been meant to be a general overview of the main features. A more deep investigation of the sensor parameters will be given in the next chapters following the work that has been done by myself as a contribution to the experiment. In order to better compare the different sensors, a parallel discussion of these parameters will be maintained:

- **Gain** as a parameter to define the quality of the device;
- **Dark Current** to introduce the problem of the noise in these kind of sensors;

- **Crosstalk** and **Afterpulse** to show some structural problems of these technologies.

2.5.1 Gain

The gain is a parameter to define quantitatively the amount of electrons multiplication in the device after a photon strikes on the surface.

MAPMT   For the photomultiplier, the gain is defined as a function of the secondary electron emission ratio. Generally it is defined as $\mu = \delta^n$. In detail, n is the number of dynodes that compose the PMT in use, while δ is the secondary electron emission ratio. The latter can be explained as a function of the interstage voltage of dynodes (E) and of the structure and material chosen for the dynodes themself. Usually the material is mathematically described with a constant with a value between 0.7 and 0.8. In this way it is possible to define $\delta = a \cdot E^k$ with a an arbitrary constant. The typical value for this kind of devices is of the order of $\mu \simeq 10^6$.
The H8500 and H12700 MAPMTs chosen for the RICH detector have a gain declared by the producer similar to each other even if they were not built for the same purposes.

SiPM   The gain is the amount of charge created for each detected photon. In fact, every time a photon is absorbed, each micro-cell generates an highly uniform and quantized amount of charge. This quantity depends on the applied overvoltage and on the micro-cell size. It is defined as

$$G = \frac{C \cdot \Delta V}{q}$$

where C is the micro-cell capacitance, ΔV is the overvoltage and q is the electron charge. In other words, G is the ratio of the charge from an activated micro-cell to the charge of an electron. The typical gain value for the SiPMs is the same as for PMTs: of the order of $G \simeq 10^6$.
All the devices under test in this work have specific gains but close to the standard one: they range from $2.3 \cdot 10^5$ to $3.6 \cdot 10^6$ [32, 33].

2.5.2 Dark Current

Dark current is a source of noise: it is the current that flows inside the device even without incoming photons. It has to be kept as small as possible because it can compromise the detection and the identification of a single photon.

MAPMT   Several are the causes of dark current in MAPMTs:

- Thermoionic emission current. This is function of photocathode and dynodes materials and their work function. For some applications it is better to have a wide spectral response to be able to work with lower energy or longer wavelengths. This implies a lower work function but an increase of thermoionic emissions. This kind of dark current varies exponentially with the supply voltage. Cooling down the device is the main technique to optimize these conditions.

- Leakage current. It can occur inside the tube between anode and electrodes and/or outside the tube itself between the anode pin and the other pins on the bulb stem. It is mainly correlated to the insultating materials used in the tubes and the supply voltage:

$$I_{leak} = \frac{V_{bias}}{R_{insulation}}$$

Contamination from dirt and moisture in several parts of the device as the surface of the glass stem, base or socket, causes an increase of the leaking current. Low humidity and clean conditions helps to reduce this component of the dark current.

- Photocurrent. Electrons that are emitted from the photocathode or dynodes but deviate from the nominal trajectories are called stray electrons. They do not contribute to the output signal but they can impinge on the glass envelope (due to the negative voltage applied to the cathode) or on the electrode support: there, scintillation may occur and result in dark pulses. A solution to minimize this phenomenon has been implemented by Hamamatsu and it is called "HA coating": they apply a conductive paint around the outside of the bulb connecting it to the cathode potential.

- Field emission current. It is correlated to an excess of voltage in the operating mode: a stronger electric field forces a larger amount of electrons to be emitted, increasing the dark current. Each device has a maximum supply voltage specified to prevent this phenomenon to occur and to prevent damages to the photomultiplier tube. Usually, for safety reasons, it is suggested to operate at a voltage level $20 - 30\%$ lower than the maximum declared.

- Ionization current. Even if the tubes are kept under vacuum, a residual gas still exists. Its particles can by ionized by the collisions with electrons

and produce a noise pulse that can be identified as an output pulse appearing right after the main photocurrent. These signals can be called afterpulses.

- Noise current. This last phenomenon is the less probable to occur: it is caused by cosmic rays producing Cherenkov radiation while passing through the glass envelope, radiation from radioisotopes contained in the glass enevelopes and enviromental gamma rays. These dark noises have low frequency, therefore they are negligible if the number of signal counts is not exceptionally small.

Precautions while using these devices are necessary to reduce the amount of noise that could compromise the detection and the analysis of low signals. The technologies used for CLAS12 MAPMTs achieve typical values of $\sim 0.1\,\text{nA/channel}$, which is one of the highest performance Hamamatsu could reach with respect to all the other PMTs produced [34].

SiPM On the contrary of MAPMTs, SiPM dark current is due to only one main phenomenon: thermal agitation. Its rate, defined as the number of dark events per unit time is a function of active area, overvoltage and temperature. During the quiescent mode, if an electron or hole is thermally generated inside the active region of the device, an avalanche is initiated and an output pulse is observed. This kind of pulse can be defined as a single dark count. This process is a source of noise at the single photon level: photon-generated or thermally generated electrons are indistinguishable. In SiPM, the thermal generation of carriers, and its rate, doubles approximately ever $10°C$.
Usually, the producer can provide an estimation of the dark count rate (DCR) per unit area, at a specified overvoltage and temperature, to allow the user to set the optimal parameters for its own application. The tecnologies under test in this work have typical values that spam from $\sim 40\,\text{kHz/mm}^2$ up to $\sim 100\,\text{kHz/mm}^2$ depending on the producer and the material used. These values are exceptionally lower than what was available only few years ago, thanks to a significant improvement in the material and production technology.

2.5.3 Crosstalk

Crosstalk is any phenomenon by which a signal transmitted on one channel creates an undesired effect in another channel. It is usually caused by a capacitive, inductive, or conductive coupling from one channel to another.

MAPMT   In the case of PMTs, crosstalk is a measure to know how accurately the light, incident on a certain position of the photocathode, is detected while retaining the position information. Ideally, it is expected that the avalanche walks straightforward as in the scheme of Fig. 2.8. If the photoelectron and the following multiplication at the dynodes starts to broaden, the signal could be read out from more than one adiacent anode. Another possibility that can cause crosstalk is that the incident light itself spreads within the faceplate.

It is a feature to be kept under control in the analysis because it can influence the real signal interpretation. A technique used with the RICH electronics to control the crosstalk is to disentagle neighbour pixels in the MAPMTs from adjacent electronic channel. This allows to distinguish the optical crosstalk (between anodes) and the electronic crosstalk (between channels).

For both MAPMTs in use for CLAS12 RICH, the measured crosstalk ranges from 2.1% in the worst conditions of the border pixels to 0.1% in the middle of the PMT. This measurements have been performed illuminating one anode with a laser pulse and recording the adjacent anode output values as relative to the illuminated one (100% being the output of the illuminated anode). The results from Hamamatsu datasheets are shown in Fig. 2.15, where 2.15a and 2.15b are the measurements for the H8500 and the H12700, respectively.
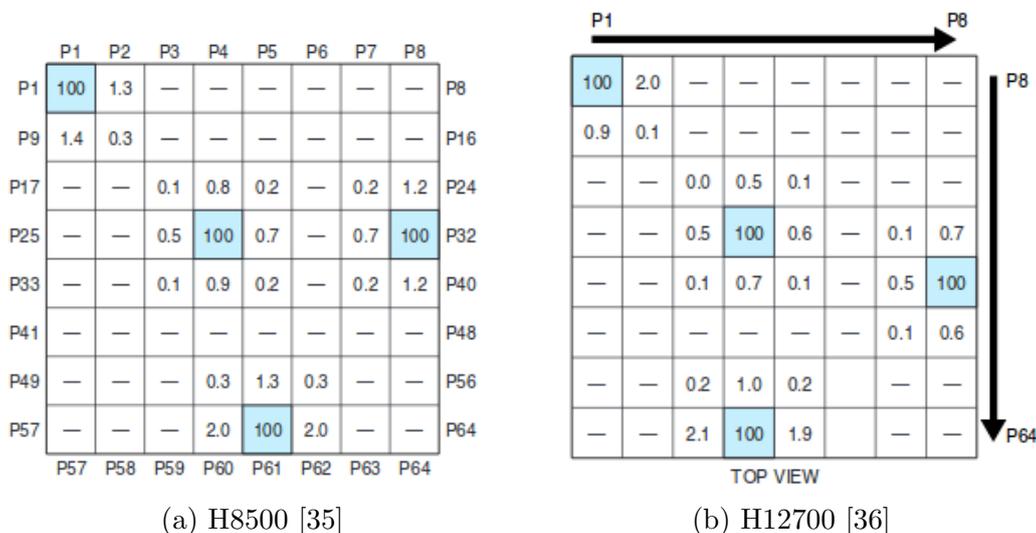

(a) H8500 [35]   (b) H12700 [36]

Figure 2.15: Example of the anode crosstalk of the RICH MAPMTs measured with a Tungsten lamp with a blue filter and a fiber of $1\,mm$ diameter (Kuraray: Clear Fiber NA=0.72).

SiPM   For these devices the crosstalk is defined as the probability that an avalanching micro-cell will cause an avalanche in a second micro-cell. This could happen since accelerated carriers in the high field region emit photons that can initiate a secondary avalanche in a neighboring micro-cells. This so-called secondary photons are emitted in the near infrared region and can travel substantial distances though the silicon. Fig. 2.16a represents the different routes the secondary photon can take to propagates:

(a) directly to a neighborin micro-cell,

(b) reflected from the window material,

(c) reflected from the bottom of the substrate.

(a) Propagation of the secondary photon

(b) Signal pulses with direct and delayed crosstalk (middle and right respectively) with respect a single discharge (left)
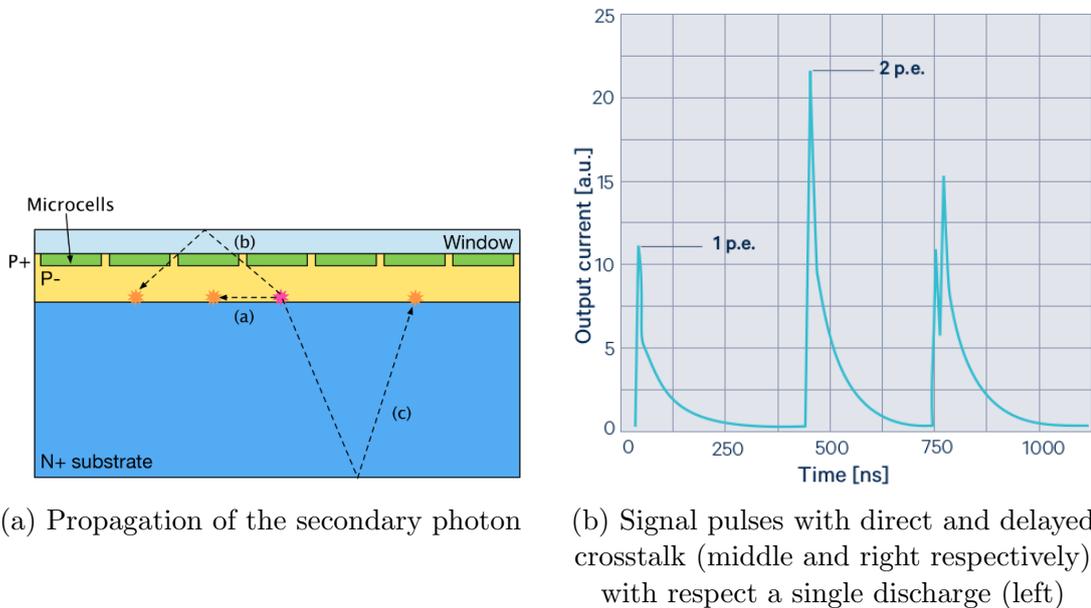
Figure 2.16: SiPM optical crosstalk.

As shown in Fig. 2.16b, with respect the single-cell signal of the left pulse, crosstalk can generate the signal equivalent to two or three photons of the middle pulse, if the process happens instantaneously, while, if a little delay occurs, the resulting signal is the third pulse. The signal crosstalk can be estimated by measuring the ratio of the count rate at multi-photon amplitude level to the count rate at the single photon level. As the optical crosstalk originates from an existing current, it is called correlated noise. It depends on the overvoltage, on the fill factor of the sensor and on the current density in the original avalanche.

In this work a comparison between different SiPM technologies is discussed, to check how state-of-the-art devices could satisfy the necessities of the RICH detector in single photon conditions. In fact, the producers are continuously improving the performance of their devices reducing the noise effects as shown for example in Fig. 2.17: on the left there is a previous product, on the right the one improved with trenches between the micro-cells where the crosstalk effect has been reduced to the level of 1%.
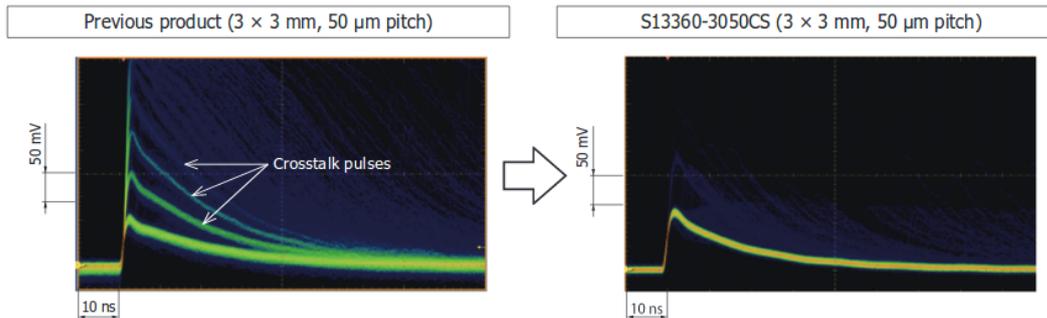

Figure 2.17: SiPM optical crosstalk improvements [37].

2.5.4   Afterpulse

An afterpulse is a spurius small amplitude signal that usually occurs a bit late in time with respect to the main signal pulse. This kind of noise may affect low level signal measurements by causing, e.g., errors in the photon (pulse) counting.

MAPMT   There are two main types of afterpulses distinguished by the time at which they are detected and by the different mechanisms from which they are generated:

- **short delay, at the ns level**. They are caused by elastic scattering of electrons on the first dynode. It is not a problematic kind of noise. Since it occurs within a very short time from the original pulse, it is often hidden in the time constant of the subsequent signal processing circuit.

- **long delay, at the level ms level**. They are generated from the ionization of residual gases in the photomultiplier tube that generates positive ions that travel back to the cathode and produce new photoelectrons delayed from the original ones. The amplitude of this kind of pulses is

related to the type of ions and the position at which they were gener-
ated. The amount of charge produced, instead, is function of the supply
voltage used.

In general, the second noise source generates more errors than the first one
while operating in photon counting at high gain. This kind of problems can
be neglected in the MAPMTs chosen for the CLAS12 RICH.

SiPM   The phenomenon that can cause an afterpulse is that a carrier re-
mained trapped in the silicon defects during the multiplication. After few
nanoseconds those particles are released and they may start an avalanche in
the same micro-cells. The net effect is a new current pulse on the tail of the
original pulse (Fig. 2.18). The amplitude of the second pulse is lower than the
original due to the fact that C_d has not recharged to V_{bias} yet. Afterpulses with
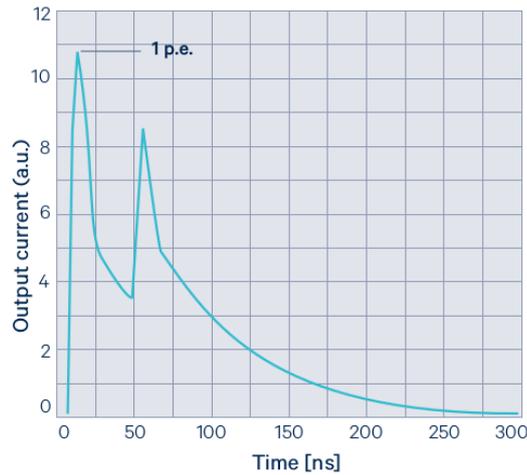

Figure 2.18: SiPM afterpulse.

short delays have a negligible impact thanks to the fact that the cell is not fully
charged. Longer delays can impact the measurement if the afterpulses are not
identified. Their probability to occur increase linearly with the overvoltage
and quadratically with the cell size because of the corresponding increase in
the gain.
The technologies under study in this work have been largely improved against
afterpulses: with respect previous products, an upgrade in terms of materi-
als and wafer process technologies allow to contain this potential issue to a
negligible level [38].

2.6   Conclusions

The measurement of the Cherenkov angle is a powerful and sophisticated instrument for particle's identification. However, the single photon detection is challenging and requires a specific and deeply studied interplay between sensors and readout electronics depending on the specific application.

Chapter 3

# Multi-anode PMTs for RICH Sector 1

This chapter presents a description of the author's work on the photon detector characterization and preparation for the first RICH sector. The chapter starts with an introduction on the RICH active area: how it is designed and how the sensor and electronic components are organized. In the following part, the laser stand built to characterize the components is presented. After a description of the setup, an explanation of the developed analyses is given and the obtained results are shown.

3.1   Overview of the RICH active area

To satisfy the main requirements of the RICH detector, i.e. minimize the resolution on the Cherenkov emission angle, a specific solution for each component has been studied. Focusing on the active photosensitive area, some very important elements to improve the performance of the entire detector are the number of photons detected per track and the uncertainty on the hit position. Those can be improved with features typical of the MAPMTs, like high granularity, minimum dead space and excellent single photon readout capabilities. As shown in Fig. 3.1a, the active area will have a trapezoidal shape at the bottom of the sector, close to the beam pipe. A particular structure to host the MAPMTs and the electronics has been studied to optimize the requested performance.

The mechanical structure, called from now on electronic panel, is shown in Fig. 3.1b. Its main role is to support the photon detector during the whole period of data-taking. Being within the acceptance of the CLAS12 spectrometer, it has to minimize the material budget but, at the same time, to guarantee a

planar surface without any deformation during the years in order not to affect the imaging of the optical flux. It has to cover a $1\,\mathrm{m}^2$ surface area and be only 1 cm thick. It is made of carbon fiber reinforced polimer (CFRP) foils with a nomex core. This material allows to sustain the instrumentation weigth combining lightness and rigidity and preserves the possibility to be worked to fit inside the prescribed space and to host anchoring elements and the printed circuit board with all their connectors. The final electronic panel is shown in Fig. 3.1b on a temporary support, constructed to run some functionality tests before being moved into the RICH sector. The detail presented in Fig. 3.1c shows the holes that will be used to host for the connectors and the screws to secure the electronics boards to the panel.
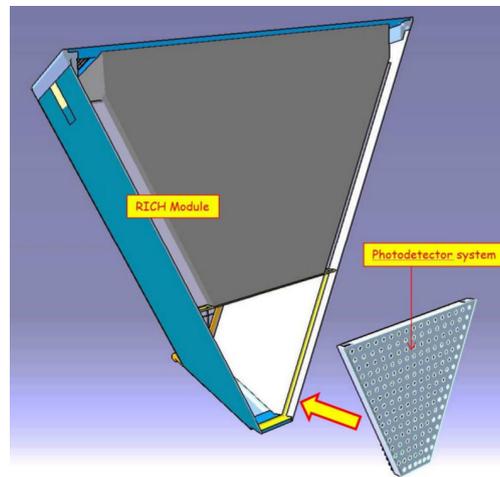
(a) Back view of the RICH sector
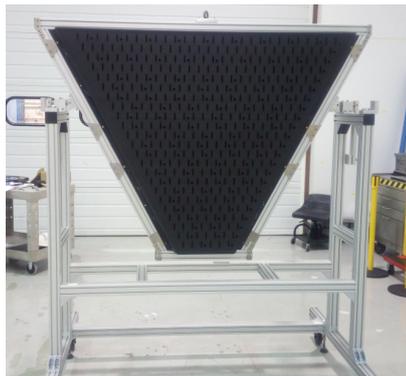
(b) Temporary support

(c) Structure

Figure 3.1: Electronic panel

The electronic panel will be the layer that separates the inner volume of the detector from the outer space of the experimental hall. The RICH detector will be filled with purified nitrogen gas to prevent moisture absorption by the aerogel radiator without interference with the optical elements and light propagation. As represented in Fig. 3.2a, the inner side of the panel will host the MAPMTs while the outer part will host the front-end electronics and the readout controllers. This mounting scheme allows to keep the heating of the electronics under control without interfering with the sealing and the light contamination.

Since there are ~ 25600 pixel to readout on the whole panel, it has been decided to bring digitization and buffering on the front-end boards just behind the sensors, while limiting the number of connections to the data aquisition by grouping the components. This allows to optimize the service lines used to supply the low voltage to the boards and the high voltage to the MAPMTs, to send the data to check the overall status of each component or to read the digitized data from the sensors. The boards will be organized in 138 compact units called tiles. Each of these tiles will host 2 or 3 MAPMTs (and the corresponding ASIC chips) depending on their position on the panel, to fully cover the trapezoidal area (Fig. 3.2b). Each tile is composed as shown in Fig. 3.2c and in Fig. 3.2d in two different configurations:

- An **ADAPTER** board in the inner side of the panel to connect the MAPMTs with the electronics. It is a passive board for mechanical and electrical matching through the electronic panel. It receives one high voltage power line and distributes it to groups of MAPMTs. There is a black custom rubber sealing bewteen the adapter and the electronic panel to prevent light trasmission and ensure gas sealing. Neighboring MAPMT anodes are mapped to be connected to separated readout channels in order to decouple the crosstalk introduced by the electronics form the one of the sensors.

- An **ASIC** board that hosts the Multi Anode Read Out Chip (MAROC). It converts the analog signals from the sensors into digitized information for the acquisition. The chip consists of 64 independent channels. Each one of them has a pre-amplification stage with a configurable 8-bit gain correction and provides both analog and digital informations. In particular, 64 digital (binary) lines are composed by a fast shaper followed by a discriminator with a configurable threshold to maximize the efficiency, while the analog line has a slow shaper followed by two track and hold circuits to allow charge measurement through a serial multiplexing. The analog information will be used mainly in dedicated runs for calibration purposes with pulse height measurements. The binary information in-

stead, as it is promptly available in parallel and can be sampled with a predefined clock on an external digital pipeline, is perfect for the RICH detector application during physics runs for signal discrimination and timing.

• A **FPGA** board as a controller unit. It works as a mediatior to exchange the information between the front-end and the external data aquisition. It helps configuring, controlling and debugging the front-end circuits.

(a) Mounting sequence

(b) Tiles scheme: blue, 3MAPMTs; cyan, 2MAPMTs

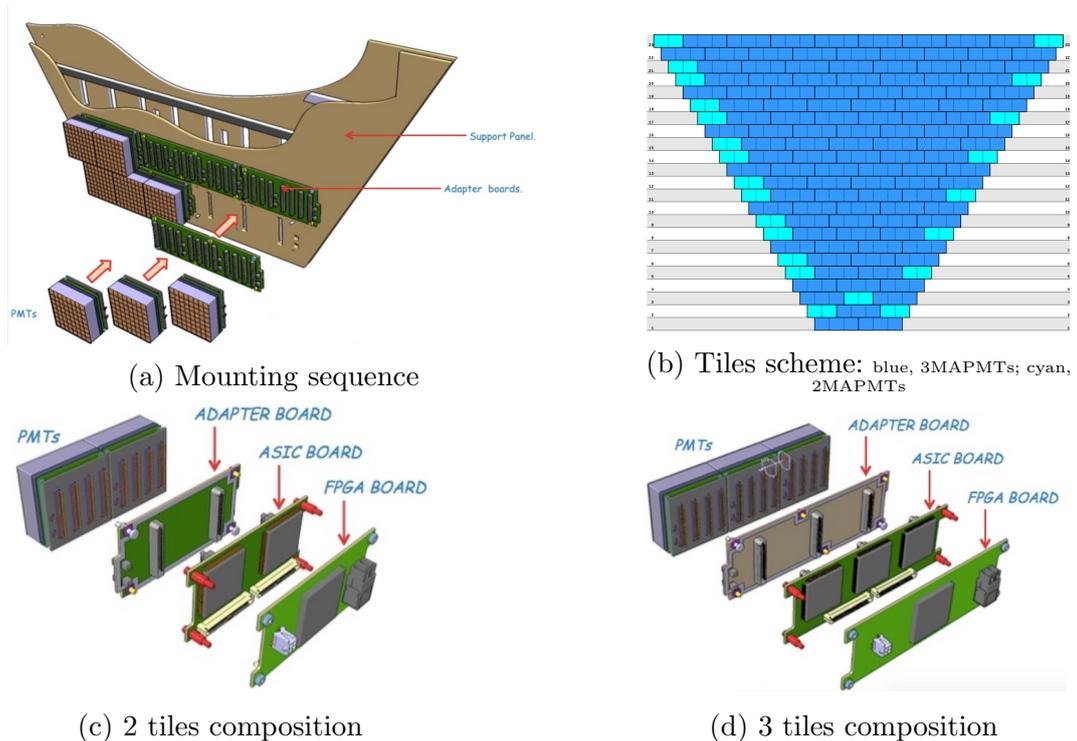(c) 2 tiles composition

(d) 3 tiles composition

Figure 3.2: Configuration scheme

Each one of them carries a different function on this board to board chain, but they work as a single extended surface. This is a good compromise between geometry and costs. At the end on the electronic panel there will be:

• 391 MAPMTs;
• 138 FPGA boards;
• 115 ASIC boards to readout 3 MAPMTs;
• 115 ADAPTER boards connected with 3 MAPMTs;
• 23 ASIC boards to readout 2 MAPMTs;
• 23 ADAPTER boards connected with 2 MAPMTs.

3.2   LASER STAND

After all the validation tests done on every single component were completed, the full tile characterization could start. This has been done on site at JLab where a pre-existing experimental apparatus has been adapted to the RICH requirements.

3.2.1   Setup

The full work has been done inside a dark box (see Fig. 3.3a) where a laser source is pulsed with a precision of tents of microseconds to simulate the condition of a single photon striking on the photomultiplier. The sensors (up to six) are readout by the complete set of front-end boards as they will be on the RICH electronic panel during the physics runs.

Laser Source   It is a PicoQuant unit with 405 nm wavelength laser. The laser head mounts a set of optical neutral density filters in order to reach single photon conditions. The laser source can be moved along two spatial directions by a set of motors to perform alignment and to fully cover the sensitive surface under test. A light diffuser has been used to reach an uniform illumination condition over the whole sensor area. This allows to run the test without the necessity to scan the active surface pixel by pixel, saving time and providing a result independent from the local variations of the sensor response. The laser movement and light intensity are controlled by the external data acquisition PC, while its turning on and off are regulated by the electronics itself.

Tiles   In front of the laser a support structure has been built to host two tiles in parallel. Two series of tracks (red in the Fig. 3.3b) have been organized to allow the tile to slide at the right position. Once installed in, the two units are readout indipendently in series, one after the other. During the test, the FPGA on-board pulse generator drives the laser with a squared wave to trigger a light pulse synchronous with the readout clock. This allows to get the minimum uncertainty, i.e. the intrinsic jitter, of the TDC time measurement.

Power Supply   The same power supply system foreseen for the final setup has been used. It is based on the CAEN SYS4527 mainframe, hosting both High Voltage (HV) and Low Voltage (LV) boards with a remote ethernet control. The HV power supply boards are CAEN A1536 with two channels used for the two units. An interlock system is running to check the status of the front door of the setup: every time the door is open the HV bias is turned off.

This is a safety measure both for the user whenever he needs to work on the setup and for the MAPMTs themselves, to avoid bright light could reach their surface and ruin their performance. The LV power supply boards are CAEN A2518A and also in this case two channel will be used to provide power to the two tiles.

Data Acquisition   An adapted version of the data acquisition program developed for the electronic stand alone test has been used. A single bash script allows the user to manage all the parameters of the apparatus and to build a logbook file to keep track of the running conditions. The MAPMTs response has been studied as a function of the preamplifier gain set, of the high voltage bias and of the TDC threshold to discriminate a pulsed signal. A full explanation will be done in the following.

The laser characterization provides a full set of data to understand how each

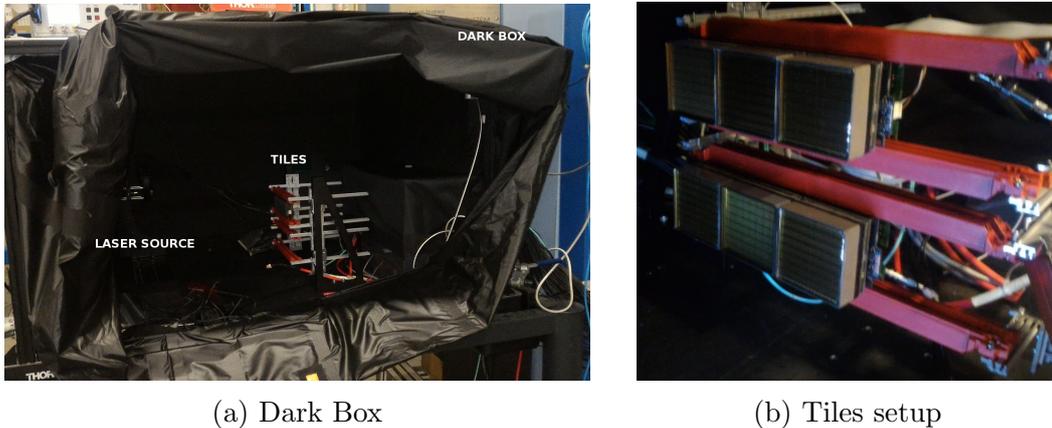(a) Dark Box   (b) Tiles setup

Figure 3.3: Dark Box configuration

component performs. Such a first-time calibration is used to define the proper working conditions of each readout unit. It identifies the relevant working parameters to be stored in the CLAS12 database and the correct procedures to measure them, in order to be able to monitor their stability and to recognize possible deterioration effects during the data-taking, by comparing the original values with the ones obtained during the actual physics runs.

3.2.2   Analysis

The MAROC front-end chips allow to extract analog (ADC) and digital (TDC) information for each MAPMT channel to identify the signal from a single Cherenkov photon.

Charge measurements   The analog (ADC) information provides an instantaneous measurement of the amplitude of the photoelectron signal. A hold signal is generated with a programmable delay with respect to the trigger to sample the analog waveform and freeze the information for the multiplexed readout. The response is linear in charge but does not support long trigger latency and precise time measurement. The tipical charge spectrum measured in single-photon regime from a MAPMTs is shown in Fig. 3.4. In the following a brief explanation of the information that can be extracted from it is provided. The charge spectrum can be fitted, as shown by the black line on Fig. 3.4,
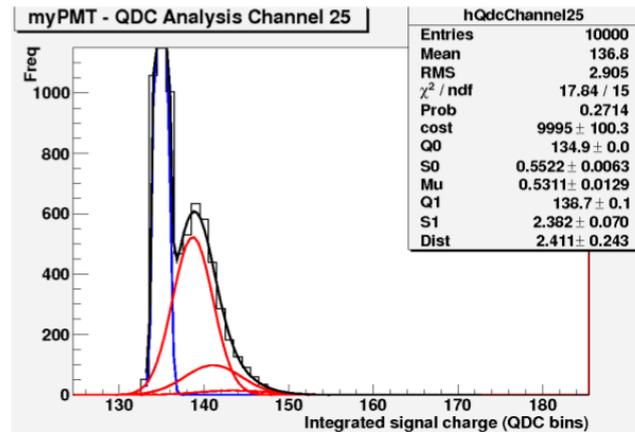

Figure 3.4: Example of a charge spectrum. The curves show the total fit (black), the pedestal (blue) and photoelectron (red) contributions.

with the following equation:

$$f(q) = A \left[e^{-\mu} P(q) + \sum_{k=0}^{N} \frac{\mu^k e^{-\mu}}{k!} G_k(q) \right]$$

where:

- **q** is the ADC value readout

- **P(q)** is a function to describe the shape of the pedestal
  (blue line in the plot shown)

- **k** is the number of photoelectrons

- **G$_k$(q)** is a function to describe the signal shape of the k photoelectrons
  (red lines in the plot shown)

- μ is the average number of detected photoelectrons

- **A** is the number of recorded events taking into account that the pedestal and signal functions are nomalized to 1.

Both pedestal and signal functions are parametrized with a gaussian distribution and, in particular, the mean and the width of the multi-photon $(k > 1)$ peaks are extracted as:

$$m_k = m_1 + (k - 1)d; \qquad \sigma_k = \sqrt{k}\sigma_1 \,,$$

with m_1 and σ_1 mean and width of the first photoelectron peak and d the separation between the first and the second photoelectron peak.

The most interesting information is provided by $\mathbf{G_1(q)}$ of the single photoelectron peak as the multi-photon peaks are related to it. The pedestal distribution represents measurements of the fluctuating baseline when a photon was not incident upon the photocathode. The single-photon condition is reached when the probability of a multi-photon event is negligible. In this regime the spectrum is dominated by single-photon distribution and the relevant information could be precisely extracted.

An example of charge spectrum extracted from a channel of a H8500 MAPMT is shown in Fig. 3.5a, and one from a H12700 MAPMT is shown in Fig. 3.5b. Here the pedestal averages have been subtracted to obtain amplitudes directly

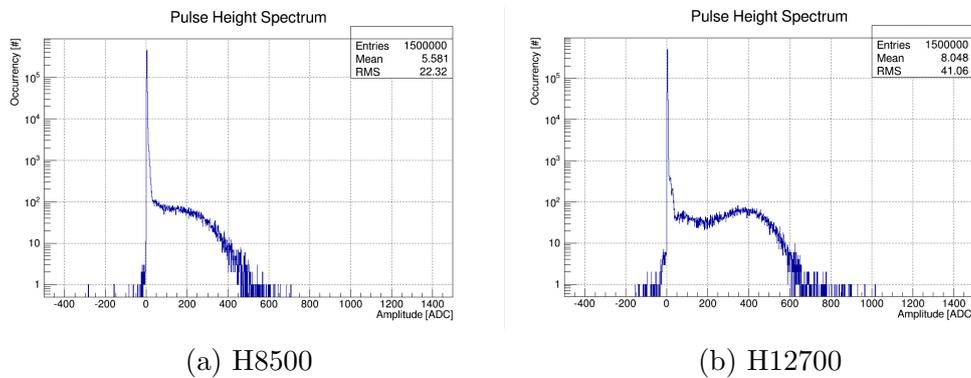(a) H8500   (b) H12700

Figure 3.5: Individual pulse amplitude spectra.

proportional to the measured charge. It is possible to note some differences between the two technologies mainly due to the fact that the H8500 version, despite born for other applications, has been found still fairly good in detecting single photon signals, whereas the H12700 version has been implemented specifically for single photon applications.

These distributions provide interesting information on the MAPMT response. My work concentrated on two main quantities:

⋄ **Gain**, numerically defined as the mean of the photoelectron peak, i.e. m_1 in the above equation, indicates the ability to promote the multiplications of electrons when the photon strikes on the photocatode surface producing a photo-electron;

⋄ **Efficiency**, defined as the ratio of the number of detected hits over the total number of triggers sent to the laser unit, provides a relative estimation of the efficiency suitable to compare the response pixel by pixel, or among various MAPMTs. The absolute efficiency, defined as the ability to detect a signal once a photon hits the photocatode surface, could have been estimated only knowing the laser intensity.

In order to get a correct estimation of both quantities, the events without a genuine signal has to be removed. Pedestal events are identified as the ones with a signal below a given threshold and, therefore, rejected. The thresold is usually defined at $5\sigma_{ped}$ values above the pedestal average m_{ped} (or 0 if the average has been already subtracted as in Fig. 3.5a and 3.5b).
Other events that are not genuine and are responsible for the shoulder at the right of the pedestal peak in the plots of Fig. 3.5 are crosstalk events.
Every time a channel is injected, the adjacent one can experience an induced signal due to, e.g., charge sharing during the discharge in the dynodes or capacitive coupling in the MAPMT or front-end boards circuits. Fig. 3.6 presents an example of the electronic crosstalk signal identified through the reconstruction of its waveform. The top plot shows the regular waveform of the injected channel while the bottom one shows the waveform of a neighbor channel. The latter is a crosstalk signal: it is much smaller, at a few % level, it resembles a derivative of the proper signal due to the capacitive coupling between adjacent input lines and, as a consequence, appears to happen earlier.
A software algorithm that develops a comparative analysis of signals in adjacent anodes (optical crosstalk) or MAROC channels (electronic crosstalk) has been developed to identify and reject the crosstalk signals together with the pedestal and clean the spectra. The plots in Fig. 3.7 show the different steps followed to improve this process. The top row shows the whole charge spectrum of the events under study whereas the central row highlights the most interesting region around the pedestal. In all the spectra, the pedestal mean value has been subtracted. The left plots (in blue) show all the events without selection. The central plots count events (in red) with a TDC hit, i.e. whose pulse has been discriminated by the front-end electronics at the programmed threshold. A large fraction of the spike at zero (the pedestal) has been already
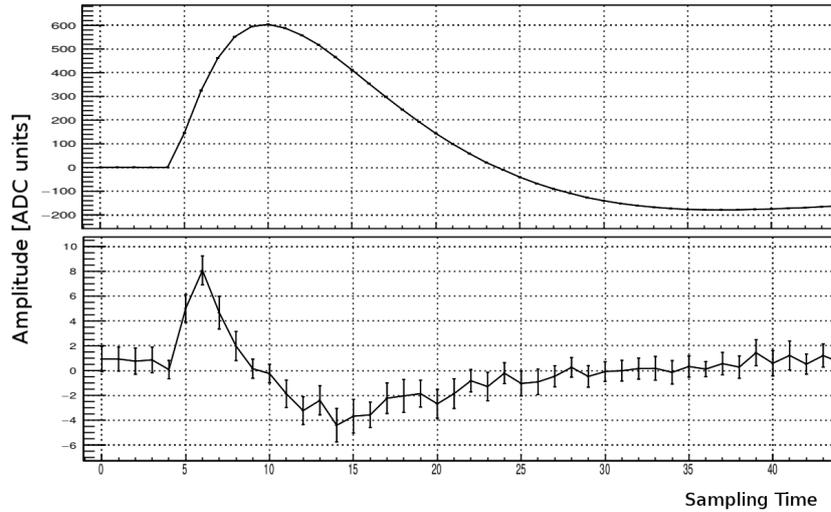
Figure 3.6: Crosstalk estimation with waveform reconstruction

cleaned up, but two smaller peaks survive at low charges. In order to under-
stand these structures in the spectrum, a crosstalk analysis is needed. The
algorithm first looks for local maxima over the MAPMT anodes, taken to be
the original signals. As a second step, it controls all the MAPMT anodes and
MAROC channels adjacent to a local maximum: if there is a signal significantly
smaller than the maximum, it is taken to be an induced charge.
The plots in the bottom row show the identified crosstalk components: on the
left (magenta) the events that have been registered when the local maximum
was an adjacent pixel on the MAPMT, in the middle (green) the events when
the local maximum was an adjacent channel on the electronics, on the right
the events taken as local maximum. The optical (from adjacent pixels) and
the electronic (from adjacent channels) crosstalk contributions have distincted
features in the spectrum. The predominat optical effects have sizeable ADC
values (between $\sim$ 15 and $\sim$ 50 ADC units). The prevalent effects of the
eletronic crosstalk appear at ADC values lower than $\sim$ 10 ADC units due to
its derivative shape (see Fig. 3.6). By subtracting these two components from
the full spectrum, the only events that survive are genuine ones represented in
the last plots on the first two rows of Fig. 3.7 (in orange).
This algorithm allows to reject cross-talk signals and to work with truly single
photo-electron events in order to extrapolate the real working parameters of
each photomultiplier. All the analyses that will be presented in the following
start from this software filter.
With the subraction of the pedestal and of the crosstalk, the estimation of gain
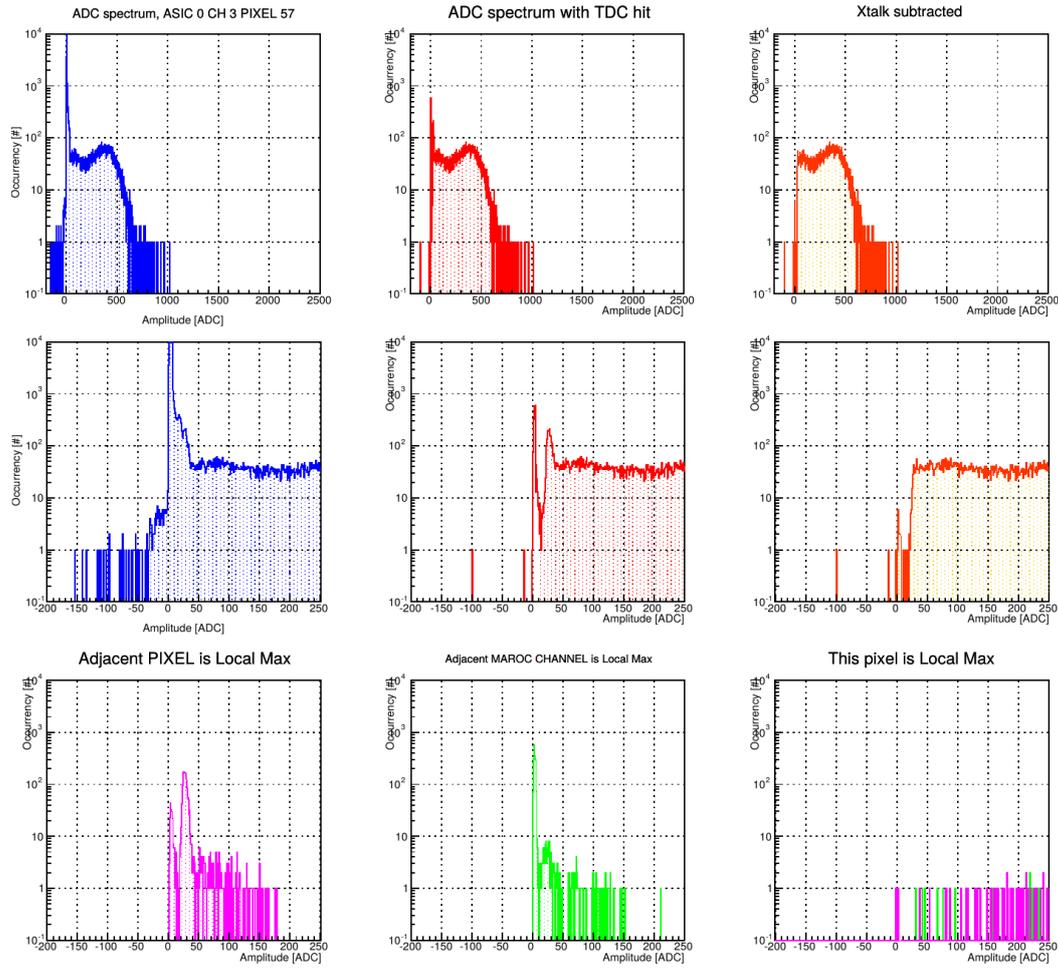
Figure 3.7: Example of crosstalk correction in charge spectrum

and efficiency is realistic. To better compare the two different photomultipliers chosen for the first RICH sector, an investigation on two main parameters given by the producer have been done:

- **Cathode blue sensitivity** or Blue sensitivity index, is the photoelectric current generated from the photocathode when a blue filter (CS 5-58) is interposed between the device and an incident light flux from a tungsten filament lamp operated at a temperature of 2856K. It is espressed in $\mu A/lm$ (microampere per lumen) [39]. It is strictly correlated to the cathode performances and its spectral response.

- **Gain** is the internal multiplication process of the detector and it is correlated with the capability to produce an avalanche when a photon strikes

on the surface of the MAPMT.

These two parameters characterize the performances of the MAPMT. Fig. 3.8 presents a scatter plot of these two quantities for all the MAPMTs that will be mounted in the first RICH sector: the H8500 appear in black while the H12700 in red. It is possible to notice that the two technologies populate the space in different ways: they have a similar range of gain, but, on average, the H12700 has a better cathode blue sensitivity, that should result in a enhanced detection efficiency.
Few tests done on the photosensors to check if they were responding as expected will be presented in the results section 3.2.3.
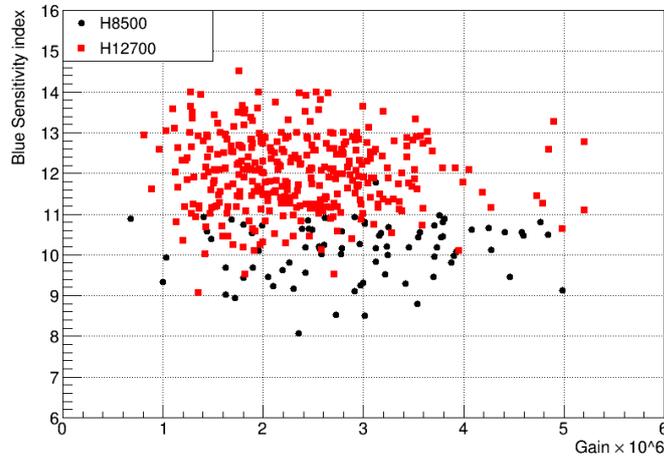

Figure 3.8: Example of crosstalk correction in charge spectrum

Time Measurements   The digital (TDC) information provides a precise (resolution less than 1 ns) time measurement of the start and stop of a signal pulse. The MAROC parallel binary outputs are obtained from a high gain fast shaper amplifier followed by a discriminator with a programmable threshold. Every time a signal gets over or under the threshold, the discriminator changes its output logical level. The TDC units inside the FPGA recognize such a level modifications and assign a time stamp to the so-called leading (going above threshold) and trailing (going below threshold) edge of the signal. The digital information is stored in a 8 μs long circular pipeline awaiting a trigger before being sent to the acquisition system. This way of processing the signal is almost dead-time free and supports the long latency expected for the CLAS12

70

trigger. Such a readout mode does not provide a direct measuremet of the signal pulse height. Still, some information on the shape of the signal can be recovered from the difference in time between the trailing and the leading edges, called time-over-threshold (TOT), which is related to the duration of the signal and therefore to the delivered charge. The choise of the threshold is extremely important not to lose any information on the incident light. A threshold too close to the baseline (pedestal) would bring in a large amount of spurious hits from electronics fluctuations. On the contrary, a threshold chosen too high would miss important information of the real signal. With the data collected in this laser stand two quantities have been investigated:

◇ **Time Walk**, shown in Fig. 3.9, is a typical systematic effect for discriminators working at a fixed threshold. In case of two signals of different amplitudes occurring at the same time, the larger signal would cross the chosen threshold earlier than the smaller signal, causing a mismatch in the measured arrival times of the two signals. As a consequence, the measured arrival time depends (or walks) on the signal charge (duration).
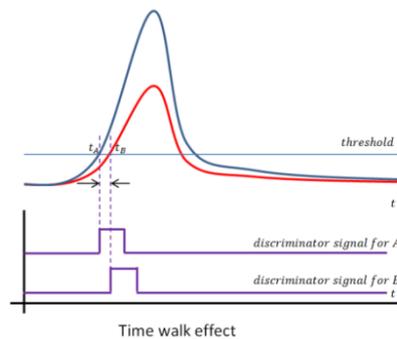

Figure 3.9: Time walk scheme

◇ **Time Offset**, is the difference in time between the discrimination of a signal and the reference clock beat. It depends on the specific length and components of each front-end circuit, but also on the distribution lines of the common clock and trigger from the central DAQ to the various front-end units. As a consequence it undergoes channel by channel variations of the order of few ns.

Fig. 3.10 shows a typical distribution of the digital quantities just introduced for the two MAPMT technologies. On the left, Fig. 3.10a shows the measured time as a function of the signal duration. Both technologies exhibit the same

trend, although the two choosen MAPMTs span a different range of charges (durations) since their gain is not equalized. On the right, Fig. 3.10b shows the time offsets for the 64 pixels of a MAPMT: the measured time of a simultaneous signal, provided by the laser pulsed with tens of picosecond precision, is presented as a function of the pixel position. There is $\sim$ 20% offset between the two technologies due to the differences in dynode structure and signal amplitude already introduced with the spectra in Fig. 3.5: lower signals have bigger time offset (H8500) while higher signals have lower time offset (H12700) as a function of the chosen threshold.

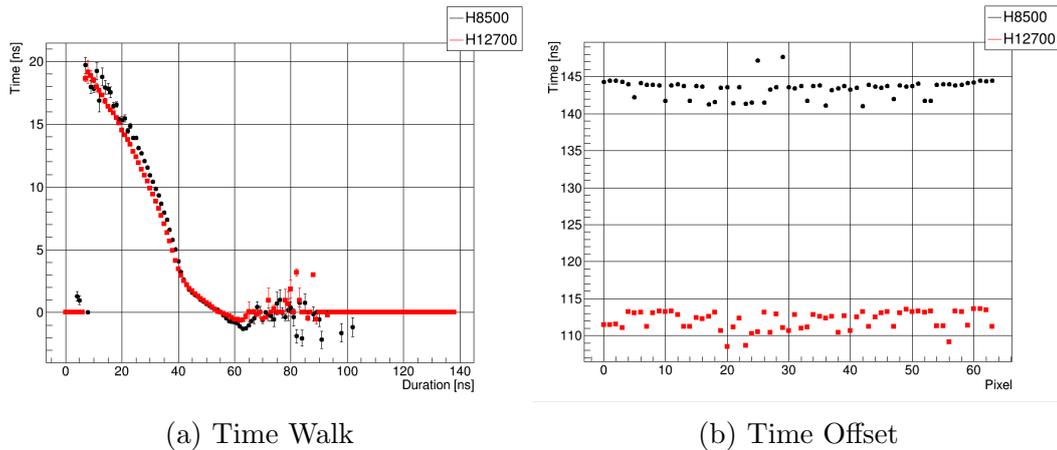(a) Time Walk   (b) Time Offset

Figure 3.10: MAPMTs Performances Comparison

In order to satisfy the RICH time resolution requirements it is necessary to apply some software correction. Fig. 3.11 shows the steps of this analysis. The first plot (3.11a) presents the measured hit time as a function of the duration of the signal of each pixel before any correction. The dispersion between all the curves has to be associated with the time offset: this is the first correction to be applied. Its result are the plot 3.11b and 3.11c. It is still not possible to recognize a narrow distribution (3.11b) of the hit time due to the time walk. To correct for this effect it is possible to calculate the dispersion of each channel with respect to the average behaviour (red dots in 3.11c): the result is shown in Fig. 3.11d. Finally, the signals with different charges (durations) are aligned. It is possible to see that the majority of the signals falls between the red lines at ± 1 ns that indicate the time resolution requested.

Setup parameters   The data acquisition has been controlled through a script that allowed to work at different values of the main parameters:

- ■ MAROC **Gain**, as the MAROC preamplification gain will be called. It

(a) Hit time vs hit duration, no correction applied

(b) Hit time distribution with time offset correction applied

(c) Hit time vs hit duration with time offset correction applied. Red dots: average behaviour

(d) Hit time vs hit duration with time offset and time walk correction applied.
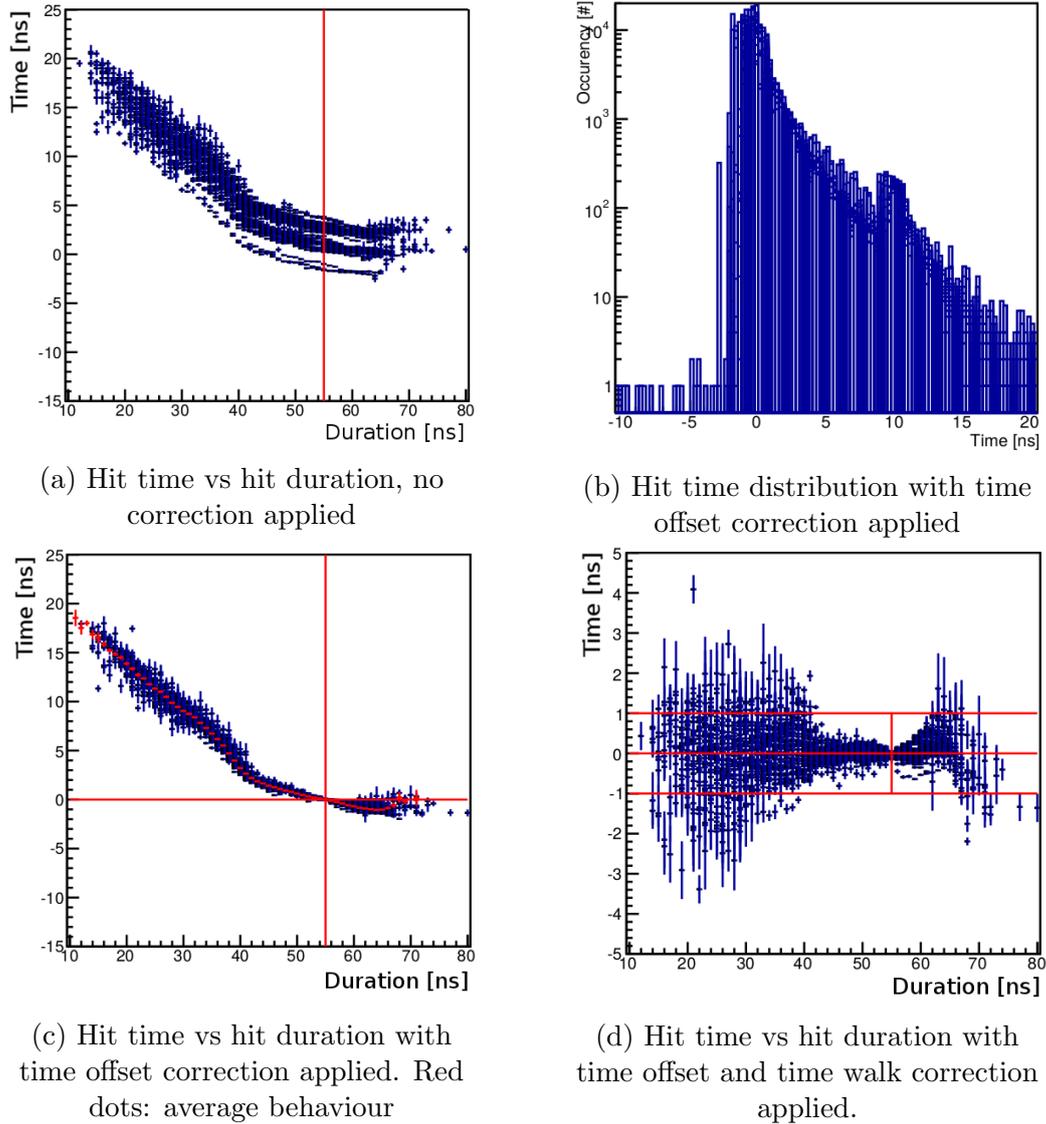
Figure 3.11: Example of the time walk correction

allows to compensate the gain dispersion among the MAPMT anodes. It can be tuned in the range from 0 to 4 with 8 bits resolution. During the laser calibration runs 5 values have been used: $G/2$, G, $2G$ that correspond to 32, 64 and 128 as a string to submit to the MAROC . The nominal value is $G = 64$, that corresponds to gain equal to 1, i.e. no modification to the signal from the MAPTMs. Smaller values cause a suppression of the signal, while larger values an amplification, with a linear relationship.

■ **High voltage** as power supply for the MAPMTs. The sensor performance changes with the bias voltage as the collection efficiency and the secondary emission of photoelectrons from the dynodes (globally referred as discharge probability) depend on the accelerating voltage. The test has been performed at 3 different values in the working range indicated by the sensor producer: 1000 V, 1075 V and 1100 V. The nominal value is 1000V.

■ **TDC threshold** is the configurable threshold value of the MAROC discriminator, common for all the channels of a chip. Its value has to be optimized to maximize the detection efficiency of all the channels while minimizing the probability of sporious hits from noisy ripples of the input baseline. The acquisition has been made at 25, 50, 100 and 200 DAC units above the TDC pedestal level, which is the DC voltage level of the fast shaper output. The DAC register has $2.2mV$ LSB. The nominal value is 50 DAC units.

■ **Light intensity** is correlated with the neutral density attenuator chosen for the laser source. The measurements were done with two different attenuation filters, referred as wheel 4 and 6 in relation to the corresponding supporting wheel position. Both filters provide single photon conditions at the anode level, but the filter on wheel 6 was choosen slightly less intense to achieve a larger hit occupancy in the sensor.

3.2.3 Results

The main results obtained during the characterization of the MAPMTs will be described in this section. At first, a check of the instrumentation characteristics will be reviewed, followed by the presentation of the behaviour of the devices with respect to the working parameters.
The first part of the study concentrates on the comparison between the features given by the producer and the ones directly measured. Each photomultiplier can be characterized by two couples of parameters. The first couple is extracted from the datasheet and it is composed by the cathode blue sensitivity and the gain, while the second couple is composed by the efficiency and the gain measured at the laser stand. In Fig. 3.12 these parameters are represented as a function of each other: the measured efficiency with respect the blue sensitivity in Fig. 3.12a and the measured gain with respect to the data-sheet value in Fig. 3.12b. The plots present values relative to the maximum of each quantity in order to remove the dependence from the different definitions. The various colors represent different front-end tiles and the dashed line is representing a

full correlation, just for reference. A strong correlation is visible in the gain case in the whole range of values accepted by the design specifications. On the other hand, such correlation is not clear in the efficiency case: both quantities shows a reduced spread of values (limited between ~ 0.75 and ~ 1) but the measured efficiency results systematically lower than the blue cathode sensitivity. This is likely due to the different method of evaluation, as the producer does not account for the mutual induction among the MAPMT anodes despite they are all illuminated at the same time.
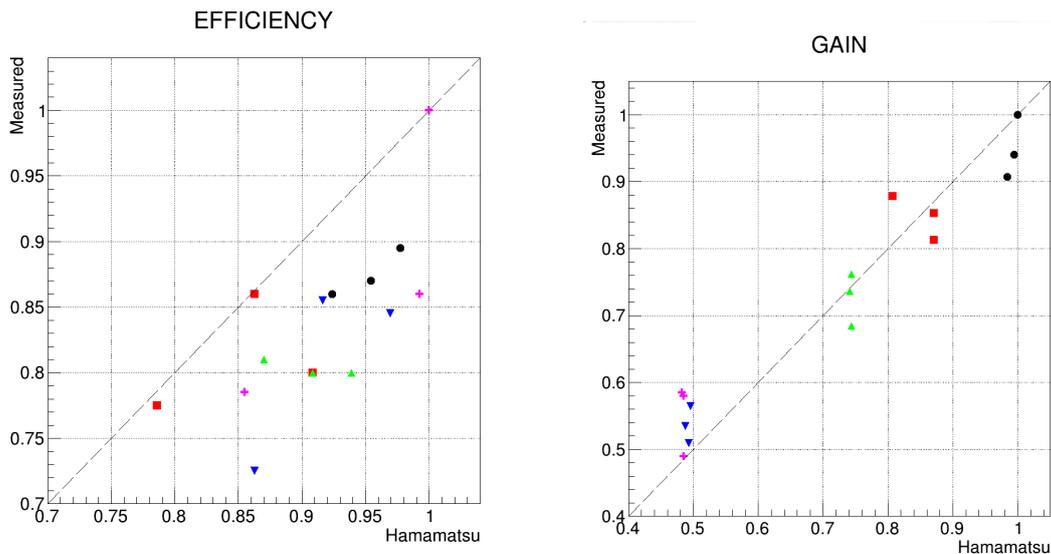
(a) Measured Efficiency vs Hamamatsu Cathode Blue Sensitivity, both normalized at the maximum value

(b) Measured Gain vs Hamamatsu datasheet's Gain, both normalized at the maximum value

Figure 3.12: Comparison between the measured and the reference values

The goal of this following analysis is to understand how the sensors behave as a function of the main working parameters that can be set at the start of a physics run. This knowledge is required to choose the best values to maximize the performance while operating in safe conditions. In addition, this study should provide a full set of reference data to be compared to the future calibration data that will be taken along the physics runs to check the readout status during several years of running.

At the laser stand, the laser light intensity was varied as a systematic check. Here the result are presented for just one MAPMT, a H12700, to show an example of the effect of the neutral density filter choice. Fig. 3.13 presents

the gain and efficiency results for the two different filters (w4 = lower light intensity, w6 = higher light intensity). No effect is detected on the charge spectrum as there is no difference in the extracted gain (see Fig. 3.13a). This is expected because nothing has changed on the sensor side. The increment of the light luminosity has effect mainly on the relative efficiency (see Fig. 3.13b) due to the increased photon hit probability per each trigger.

(a) Gain measurement   (b) Efficiency measurement
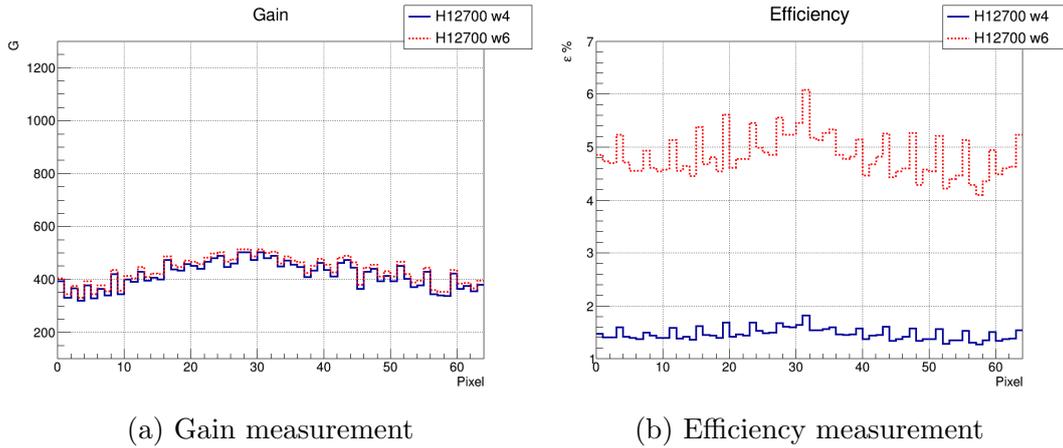
Figure 3.13: Light Luminosity Test

In the following, for simplicity, the results are discussed for the only case of low light intensity. This is the condition that better resembles the final application, where not more than one Cherenkov photon per PMT is expected. Higher intensities could provide larger statistics, but unnecessarily magnify the crosstalk effect between anodes.

The first results presented will be the ones of the analog part with efficiency and gain, to go on, at the end, with the digital part with the time measurements of time offset and time walk.

For this analysis some values have been chosen as nominal: high voltage at 1000V, MAROC gain at 64 (=1, no amplification) and threshold at 50 DAC units. Whenever one of these parameters is not explicity mentioned in the plot, it has been chosen at the nominal value. The result obtained at the nominal working parameters is the reference used to calculate the ratio of the analog quantity under study (efficiency, gain) or the difference for the time offset. The plots are organized in order to show the behaviour of the quantity under study as a function of two working parameters, while the third is chosen equal to the reference value.

Charge measurements   The quantities of interest (gain and efficiency) have been studied as a function of the various working parameters, to understand

their behaviour in every condition and highlight possible correlations.

The measured gain is the product of the avalanche process in the MAPMT dynodes (MAPMT gain) and the linear pre-amplification stage of the readout chain (MAROC gain). Fig. 3.14 shows a typical outcome of the gain study. The plots show the ratio calculated from the measured gain in each working condition with respect to the one obtained at the nominal values of the working parameters. The ratio is studied as a function of the MAROC gain for different values of high voltages (Fig. 3.14a), as a function of the MAROC gain for different values of thresholds (Fig. 3.14b), and as a function of the high voltage for different values of thresholds (Fig. 3.14c). The general trend is summarized in the following points.

(a) Gain Ratio vs MAROC Gain at different values of HV

(b) Gain Ratio vs MAROC Gain at different values of THR

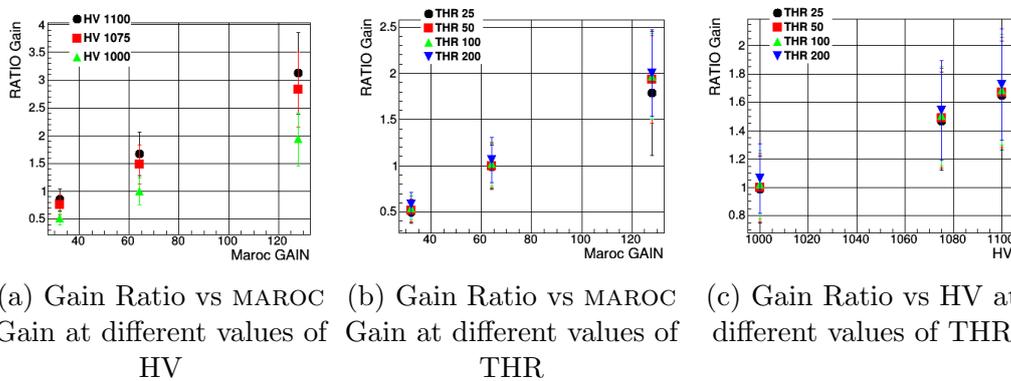(c) Gain Ratio vs HV at different values of THR

Figure 3.14: Gain Analysis

- As expected, the measured gain is directly proportional to both parameters that control the signal amplification: MAROC gain and high voltage (affecting the multiplication in the MAPMT dynodes). In particular, Fig. 3.14a indicates that for every high voltage set the measured gain increases as the MAROC gain, but the slope of increase rises up with the high voltage.

- The choice of the threshold influences the gain measurements because the gain is calculated as the average of the photoelectron peak in the charge spectrum. The gain difference between the higher and the lower values of the threshold is stable around $\sim 20\%$ and independent from the high voltage in Fig. 3.14c. However the threshold seems to influence more the result at the extreme values of the MAROC gain, where the gain spread reaches values up to $\sim 50\%$, see Fig. 3.14b.

The gain control is important for at least two aspects. The first is the capability of equalizing the response of the MAPMT anodes before the discrimination

stage, at which a common threshold is applied over the whole front-end chip. The second is the capability to compensate possible ageing effects that could deteriorate the photon sensor response during the data-taking.

The relative efficiency is defined as the ratio of the number of detected hits over the total number of trigger sent to the laser source. Fig. 3.15 shows the typical outcome of an efficiency study. The efficiency ratio with respect the nominal working condition is studied as a function of the MAROC gain for different values of high voltages (Fig. 3.15a), as a function of the MAROC gain for different values of thresholds (Fig. 3.15b), and as a function of the high voltage for different values of thresholds (Fig. 3.15c). Such a study qualifies the response of the photon detector, as summarized in the following.

(a) Efficiency Ratio vs MAROC Gain at different values of HV

(b) Efficiency Ratio vs MAROC Gain at different values of THR

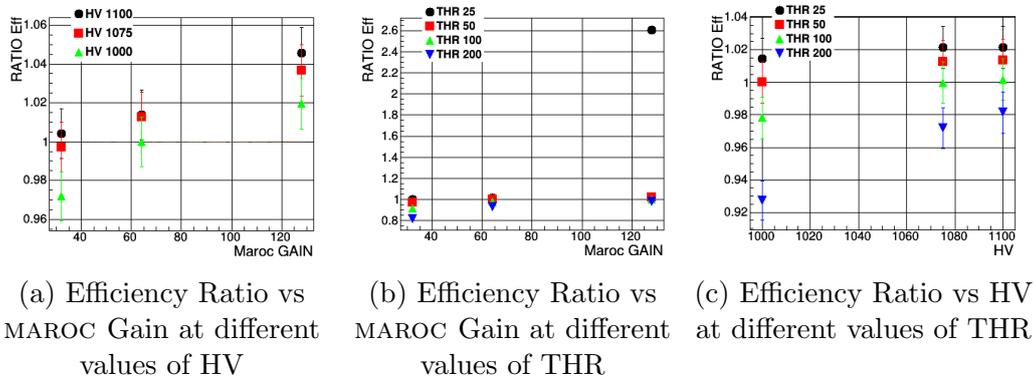(c) Efficiency Ratio vs HV at different values of THR

Figure 3.15: Efficiency Analysis

- Values of the MAROC gain lower than the nominal one reduce the efficiency, while the effect of the amplification is not so strong as the efficiency seems to reach a sort of saturation.

- Lower thresholds correspond to a higher efficiency while with higher thresholds the efficiency decreases. This happens because when the threshold increases, the cut reaches the signal and good events are not recorded.

- In case of low gain (< 64), a proper choise of high voltage (that should be high) and threshold (that should be low) can help to keep the efficiency close to the saturation level.

- Conditions of high gain (> 64) or high voltage ($= 1100V$) reduce the sensitivity to the threshold.

The saturation effect of the efficiency is important because allows to identify a wide range of safe values of the working parameters at which the photon detector response is stable. This implies that a fine tuning of the working conditions is not necessary and that the performance could be monitored and easily compensated during the years of operation. In particular, the efficiency is not directly related to the gain and it is only affected when the gain is not adequate (too low). As soon as the amplification is adequate, the efficiency (or its saturation value) depends at the first order from the quality of the photo-catode. The photo-catode deposition is a complicated process and is not uniform among the MAPMT sample as can be deduced from the blu cathode sensitivity values provided by the manufacturer. Working at amplifications higher than necessary is not helpful, as increases ageing effects and crosstalk probability for the MAPMT.

Time measurements   The behaviour of the relevant quantities (time offset and time walk) have been studied as a function of the working parameters (MAROC gain, high voltage and discrimination threshold).

The time offset is defined as the difference between the time at which the signal occurs and the reference clock beat. Fig. 3.16 shows the typical outcome of a time offset analysis. The difference with respect to the nominal working conditions is studied as a function of the threshold for different values of MAROC gains (Fig. 3.16a), as a function of the high voltage for different values of thresholds (Fig. 3.16b), and as a function of the high voltage for different values of MAROC gains (Fig. 3.16c). The behaviour is summarized in the following points.

(a) Time vs THR at different values of MAROC Gain

(b) Time vs HV at different values of THR

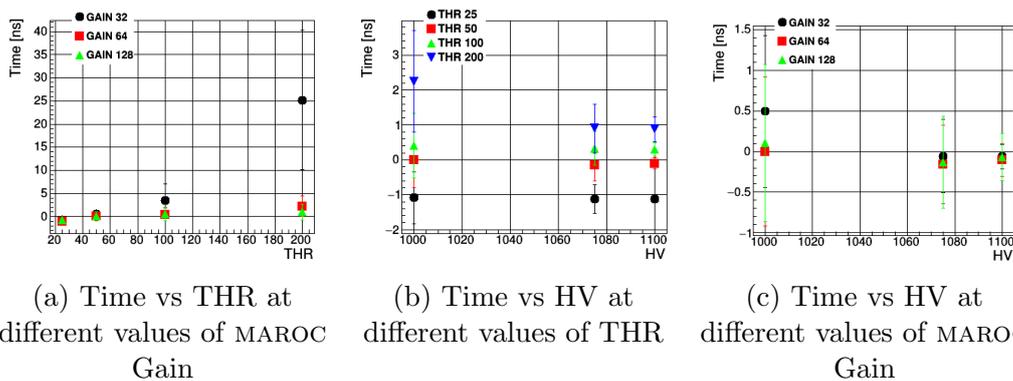(c) Time vs HV at different values of MAROC Gain

Figure 3.16: Time Offset Analysis

- Fig 3.16a shows that the time offset increases with increasing threshold. This is due to the shape of the rising edge of the wavefront. When the

gain is low the time offset's rise with the threshold is significant. As soon as the gain is enough, the rising edge become steep so that the threshold does not anymore significanlty influence the time offset measurements.

- At low gain and low high voltage the time offset is high (see Fig. 3.16c). Increasing the high voltage helps to reduce the time offset in conditions of low amplification. Gains at the nominal value or above improve the time offset in a way that the high voltage is barely effective in the performance.

- Fig. 3.16b presents the situation at the nominal gain. At low threshold (25 and 50 ADC units) the time offset is independent from the high voltage set, but as soon as the threshold increases, a larger amplification at the PMT level, thanks to the supplied higher voltage, helps to increase the signal and reduce the time offset.

The time offset depends, in first approximation, on the specific circuit and components of each readout channel. It depends however also on the amplitude (or shape) of the signal pulse. At low amplification the time offset undergoes large variations, but as soon as the gain is adequate, the offset values are stable over a wide range of working parameters. This behaviour can be better understood by investigating the time walk.

The time walk is defined as the difference in the time at which signals of different amplitude cross the threshold. The MAPMT avalanche process follows a statistical behaviour and largely depends on the multiplication at the first dynode when the number of electrons is limited. As a consequence, the single photo-electron signal naturally spans a wide range of amplitudes. Low signals cross the thresholds later than large signals, as suggested by the above time offset study. The best way to control the readout performance related to this effect is to study the correlation between the hit time (time at which the event occurs) and the duration of the signal (which is proportional to the amplitude of the analog signal and therefore to the charge detected), as done in Fig. 3.17. The relation between hit time and duration was studied at different values of high voltage (Fig. 3.17a), different values of MAROC gain (Fig. 3.17b), and different values of threshold (Fig. 3.17c). The main features are summarized in the following.

- The hit duration spans a typical range and there are no too short signal (less than 15 ns), because they stay below threshold, or too long (greater than 70 ns), because of the single photon-electron regime conditions.

- In general, larger durations correspond to earlier times as signal of large amplitude anticipates the time at which they cross the fixed threshold chosen.

(a) Hit Time vs duration of the signal at different values of HV

(b) Hit Time vs duration of the signal at different values of MAROC Gain

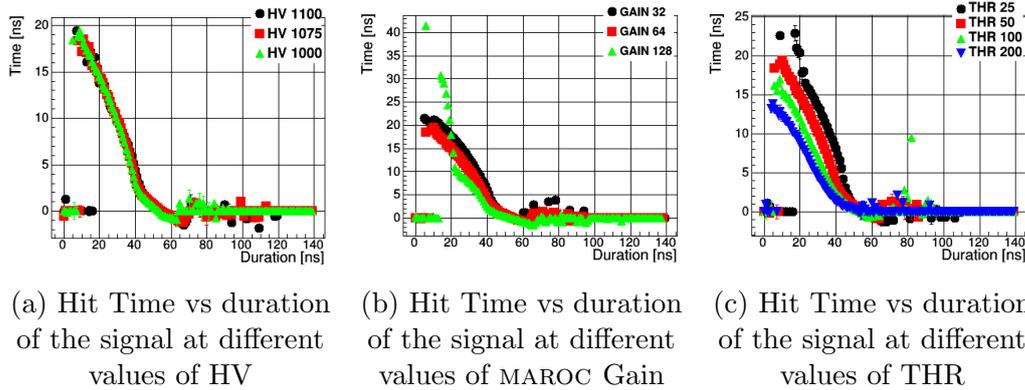(c) Hit Time vs duration of the signal at different values of THR

Figure 3.17: Time Walk Analysis

- The high voltage changes the amplification but seems not to affect the shape of the signal and therefore the relationship between hit time and duration. It is clear from Fig. 3.17a that the behaviour does not change.

- The time walk appears to depend on the MAROC gain in Fig. 3.17b. As the MAROC gain acts on the amplification similarly to the high voltage, this dependence is likely a reflection of the interplay with the threshold. It is possible to notice that an increase of the gain reduces the time walk effects, but not far from the design resolution of 1 ns. Some effects appear at high signal, as in the case of gain 128 (green triangle), where probably the setup limits does not allow to return a proper signal to analyse.

- the time walk exhibits a strong dependence on the threshold as shown in Fig. 3.17c. This is expected, as the time walk follows the shape of the rising edge.

In order to achieve the required 1 ns time resolution, a software correction for the time walk is required, as presented in Fig 3.11. In first approximation, the amplification (high voltage or MAROC gain) affects the charge spectrum, i.e. the distribution of the hit duration, but does not alter the relationship between hit time and duration. The time walk correction should be defined as a function of the choosen threshold provided that the gain is adequate.

3.3   Conclusions

The characterization done as part of this work on every active component of the RICH detector and additional spares at the laser stand was very important

to validate the photo sensors and readout elements, investigate a proper working point and collect a reference set of data before assembling the detector.

The first step was to check and verify that all the tile components - MAPMTs, adapter boards, MAROC boards and FPGAs - were working properly. As a second step the validation of the datasheet parameters has been done. Finally, investigating the response of all the components in various running conditions allowed to define the configuration parameters that can be tuned to maximize the performance without drawbacks. As the single-photon detection efficiency reaches a plateau at moderate values of gain and bias voltage, the definition of the working point is not critical. Strong gain suppression may be effective for some noisy pixels, but for the entire MAPMT may be counterproductive. On the opposite side, strong gain amplification did not show any benefit. For this reason as a starting point the readout preamplification gain will be set around 1 (64 in the MAROC DAC units) with a possible mild modulation to equalize the signal shape before discrimination (see Section 5.4). A discriminator threshold per readout chip will be defined relative to the pedestal value, with a typical value of 50 DAC units.

This set of data provides a reference to be used with future calibrations to compare the performance before and during irradiation. If some MAPMT performance changes in time, the calibration done before irradiation helps in evaluating which are the possibilities to bring it back to a normal situation: if, for example, through the power supply, by affecting also the neighbors MAPMTs that share the same tile, or through the MAROC gain amplification or suppression done at channel level.

Chapter 4

SiPM for the RICH sector 2

This chapter presents the preparatory work done for the second sector of the CLAS12 RICH detector that will be built in the next future. The focus is on the choice of the best candidate for the photon detector: the silicon photomultiplier (SiPM). A brief motivation about the choice of this new type of photon detector is done at the beginning of the chapter. In the follow-up, the validation study done as part of this work is reported. In particular, the proof-of-principle beam test and the irradiation test done on SiPM prototypes is reviewed and the results discussed. To conclude, the preliminary study of the performance of novel SiPM matrices in conjunction with the RICH readout is presented.

4.1 Motivations

The hybrid optic design of the RICH detector have been studied to reduce the active area to about $1\,\mathrm{m}^2$ on each sector. This approach demands to image both direct and reflected light. To be able to reconstruct both type of tracks and satisfy the physics requirements it is necessary to disentagle the direct and the reflected photon paths with a traveling distance of about 1 m and 3 m, respectively. This implies a time resolution of at least 1 ns. Moreover, to not degrade the Cherenkov angle measurement, the spatial resolution required is less than 1 cm.

Being compatible with the above constraints, matrices of silicon photomultiplier (SiPM) have been considered as a cost-effective solution for the second RICH sector in conjunction with the same readout of the MAPMTs used for the first sector. Solid-state SiPMs have several good features that make them a good photon detector candidate for Cherenkov applications [41]. They are compact and light with a robust mechanical design. Their technology is in rapid evolution and is suitable for mass productions with optimized costs.

They offer fast timing and are insenstive to the magnetic field. With a comparable gain to the MAPMTs now in use, they do not need high bias voltages. The drawbacks are the high dark rate, the sensitivity to temperature and to radiation.

To validate the use of SiPM for the CLAS12 RICH, several tests have been performed at different facilities. A preliminary beam test of a small RICH prototype was done at the T9 beam line in the CERN-PS East Area. The main goal of this test was to get a proof-of-principle of the use of SiPM for Cherenkov applications. The prototype was made by customized arrays of 3×3 mm^2 SiPM sensors. The Cherenkov ring was generated by a 8 GeV/c pion beam passing through an aerogel radiator with refractive index $n = 1.05$. The SiPM response could be studied as a function of the temperature over a range from -25°C to $+25$°C thanks to the use of water cooled Peltier cells. The test showed that it is possible to work with SiPM in the single-photon regime and reach stable and uniform conditions in a wide range of overvoltages at low temperatures. The Cherenkov signal could be effectively isolated thanks to the fact that a time resolution better than 1 ns was achieved in all the working conditions and as good as 130 ps could be reached in the best condition of temperature and overvoltage.

To further validate the use of SiPMs as single photon detectors in the CLAS12 environment other tests have been performed and will be introduced in the following sections.

4.2 Irradiation Test

The neutron fluence expected at the CLAS12 RICH photon detector position has been evaluated to be around few 10^9 n$_{eq}$/cm^2 per year at the maximum luminosity of 10^{35} cm^{-2}s^{-1} and at an overestimated 100% duty cicle. Such a fluence is not too high to prevent the use of SiPMs, but could still results prohibitive for a single photon application.

The irradiation test performed at the Frascati Neutron Generator (FNG) of ENEA allowed to study the response of SiPMs to an environment with a moderate irradiation rate. At the FNG it is possible to exploit the $T(d, n)\alpha$ reaction to produce an isotropic flux of 10^{11} neutrons per second of 14 MeV energy. Two pictures of the experimental area are shown in Fig. 4.1.

In the following sections the setup and the analysis methods will be introduced and the irradiation test work and the results will be discussed.

Figure 4.1: FNG experimental hall

4.2.1   Setup

Several SiPM types from different producers have been irradiated at the FNG facility. The tested devices, shown in Fig. 4.2, were 3×3 mm^2 SiPMs of different micro-cell size as listed in the following.

- **Hamamatsu** prototypes with micro-cell sizes of $10\,\mu$m, $15\,\mu$m, $25\,\mu$m, $50\,\mu$m and $100\,\mu$m. Some of the devices with this micro-cell sizes have been studied with two different technologies: the *standard* one and a new one under developement that has introduced *trenches* between the micro-cells to reduce the optical cross-talk.
- **Advansid** with micro-cell sizes of $40\,\mu$m for two different types: RGB for *visible light detection* and NUV for *Near Ultra Violet light detection.*

In Fig. 4.2a all the tested devices are presented on their holder that have been used during the test. The SiPM have their own label to be distinguished before and after irradiation while handled for testing. In the bottom row, the

Advansid SiPMs can be identified thanks to their own socket adapter (the small green printed circuit board) to be connected to the evaluation board. A custom adapter has been used for the bare Hamamatsu SiPMs visible in the top row. In Fig. 4.2b the holder is shown in the position ready to be irradiated.


(a) SiPMs on the test holders

(b) SiPM samples ready to be irradiated

Figure 4.2: SiPM during the test

The irradiation was done into steps. At each step, the SiPMs were exposed at a given neutron dose monitored by the number of detected alphas. Tipically, each step delivered twice the dose of the previous run, balancing longer running times with higher fluxes. As not all the devices were exposed at the same time, a difference in the irradiation sequence can be noticed. Moreover some SiPM has been irradiated more than the others to try to reach the limit a technology like this can afford for single-photon detection. The SiPM response has been analysed before and after each step of irradiation. The pre-irradiation measurements have been performed in Ferrara, while all the other measurements were done on site after every irradiation run. Two testing setups were realized to perform the following measurements.

I-V Characteristic Curve: it is a standard characterization for this kind of devices. The measurements have been done by means of a Keithley 6487 picoamperometer, shown in the lower right part of Fig. 4.3a. The devices under measurement were placed inside a small dark box. A

bash shell script and a programmable power supply (on top of the Keith-
ley in the picture) allowed to register the absorbed current for different
values of the bias voltage.

Dark Count Signal Analysis: it is a protocol designed to evaluate
the single-photon detection capability and to better understand the main
source of noise as a function of the temperature and the irradiation. Dur-
ing the measurement, the SiPM signal was preamplified by an Advansid
ASD-EP-EB-N evaluation board and then sampled at $2.5\,\mathrm{Gb/s}$ over a
$20\,\mathrm{ms}$ time window by a Tektronik DOP 7254 oscilloscope shown in the
left part of Fig. 4.3a. The device under test was in the dark box and
controlled in temperature by the Peltier cell. Fig. 4.3b shows the inside
of the small dark box with the setup for the measurements with the os-
cilloscope: it is visible the preamplification board on which the device
under test is installed.
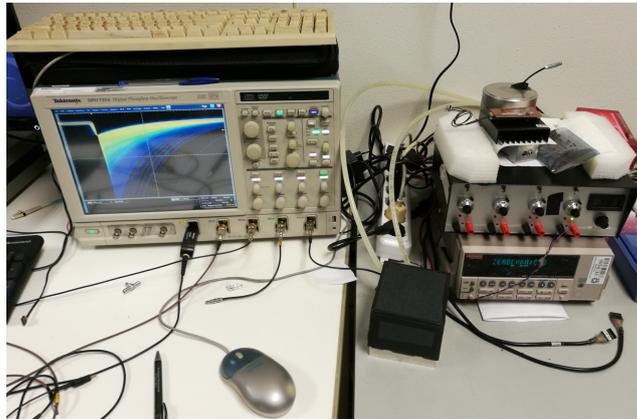
(a) The two measuring setups in the lab
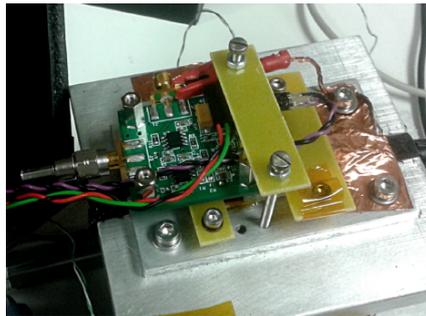
(b) The inside the dark box

Figure 4.3: SiPM Setup in Ferrara

4.2.2   Analysis

The analysis of the SiPM response has been done in two different ways to maximize the understanding of their behaviour in different condition of radiation and to validate their use for single-photon detection in the CLAS12 enviroment. This paragraph will be divided into two parts to follow the work of the analysis.

I-V Characteristic Curve   The aim of this measurement is to investigate the characteristic curve of the absorbed current versus the applied bias voltage. The devices were measured after every run of irradiation to be able to follow step by step any change in the characteristic behaviour.
Fig. 4.4 shows an example of the SiPM I-V characteristic curve studied. In the top plot there is the measured absorbed current versus the bias voltage, in the bottom, the calculated current derivative. The bias voltage scan run from a value below the breakdown voltage, where the absorbed current is minimum and quites constant, through a first current absorption peak following the brakdown, along the operating voltage interval where the current increase proportionally to the bias and the derivative is almost flat, until the next change of slope that corresponds to the un-controlled multiplication of secondary discharges and identifies the end of the bias range in which the device can operate.
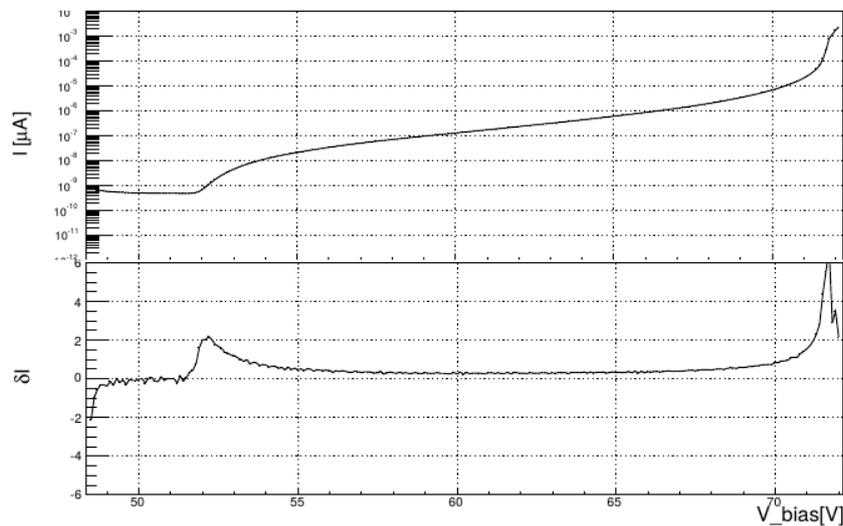

Figure 4.4: Example of a I-V analysis

Dark Count Signal Analysis   In the CLAS12 RICH enviroment, and in general in Cherenkov applications, the crucial parameter is the single photon capability. This second part of the analysis on silicon photomultipliers is not standard and it is elaborated specifically to verify the needs of a Cherenkov detector in terms of noise. Thermal effects are usually the main cause at the origin of the dark rate in a SiPM. Generally it may be also followed by after-pulses or optical cross-talks. As explained in the section 2.3.3, the signal from a silicon photomultiplier is composed by a fast rising edge that corresponds to the discharge initiated by the photon and a slow trailing edge correlated with the recovery phase of the cell bias with time constat $C_d \times R_q$.

In order to resolve pulses close in time, the first part of the analysis involves the application of a custom software filter, developed as part of this work, to reduce the slow signal tail due to the SiPM micro-cell recharge. Basically the filter correct each sampled value V_i that occured at a time t_i using a weight-average of the previous N samplings (~ 15), with weights that accounts for the exponential fall with the typical time constat τ (of the order of 50 ns):

$$V_i^{filtered} = V_i - \frac{1}{N} \sum_{j=1}^{N} V_{i-j} \cdot exp\left(-\frac{t_i - t_{i-j}}{\tau} \right).$$

A second correction is applied to remove the undershoot tail at the end of the SiPM pulse. The average pulse shape, extracted from a sample of selected single-discharge signals, was used to correct the undershoot of each pulse after rescaling it by the pulse amplitude. Fig. 4.5 shows the signal before and after the software filter is applied: the blue line is the original signal, the red one is the signal after the filter and the horizontal line is the threshold chosen to perform the pulse identification. The aim of this correction is to allow to isolate the dark counts, resolving possible overlaps, and to analyse them as signal peaks. For each of the registered pulses, the amplitude, integrated area, width and time distance from the previous peak are recorded, to be able to identify the single and the multiple micro-cell discharges and to distinguish specific sources of noise as, for example, after-pulses.

4.2.3   Results

In this section the most significant results are discussed. For simplicity, only one kind of SiPM is considered to discuss the relevant information. The later development trend favors small micro-cell size as this ensures linearity of the response in a wider dynamic range due to the enhanced capability of photon counting (a cell discharge is independent from the number of photons initiating it). It has been chosen to present the Hamamatsu $25\,\mu$m micro-cell size, as
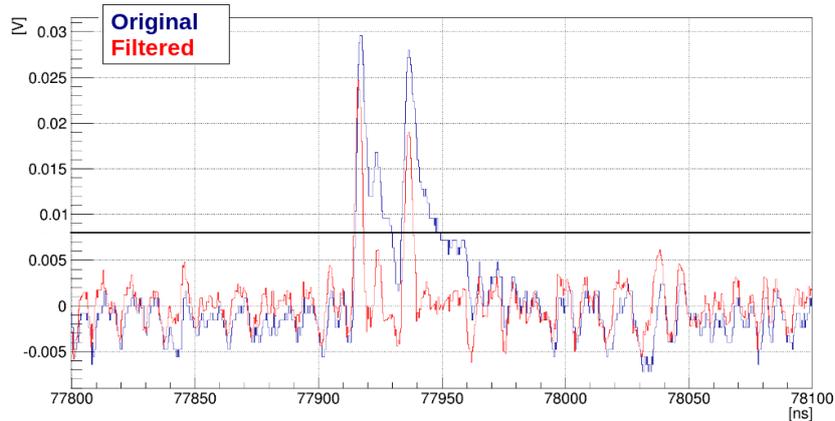
Figure 4.5: Example of the application of the software filter. (Blue) Original
signal; (Red) Filtered signal; (Black) Threshold for the pulse analysis

available with both techologies: the standard one (labeled S12572), and the
one with trenches (labeled S13360). To follow the order already used in this
chapter the results will be discussed following the above introduced setups
and the relative analyses. At the end a comparison of the two studies will be
presented as a check to validate the dark count signal analysis, since it is a
non-standard approach.

I-V Characteristic Curve   To investigate the progressive irradiation ef-
fects, this analysis was run after every step of irradiation. At first, a qual-
itative analysis on the shape of the characteristic has been made. Fig. 4.6a
shows the various measurements of a SiPM with different colors, all performed
at 22°C. The curves are presented as a function of the applied bias voltage.
The top plot shows the measured absorbed current; the central plot shows the
calculated derivative of the current; the bottom plot shows the ratio of each
curve with respect to the reference taken before irradiation (corresponding to
the lower black curve in the top plot). The derivative helps to understand if
the shape of the I-V characteristics changes with the fluence, while the ratio
helps to quantify the increasing of the absorbed current. Basically, while the
typical behaviour of the current absorption does not change, the amount of it
worsen by orders of magnitude with the increase of the irradiation dose.
As a second step, to compare the two geometry under test, a value of each
ratio, taken at the operating voltage suggested by the producer, is reported in
Fig. 4.6. The blue triangles indicate the standard technology and the magenta
squares the new trench one.

90
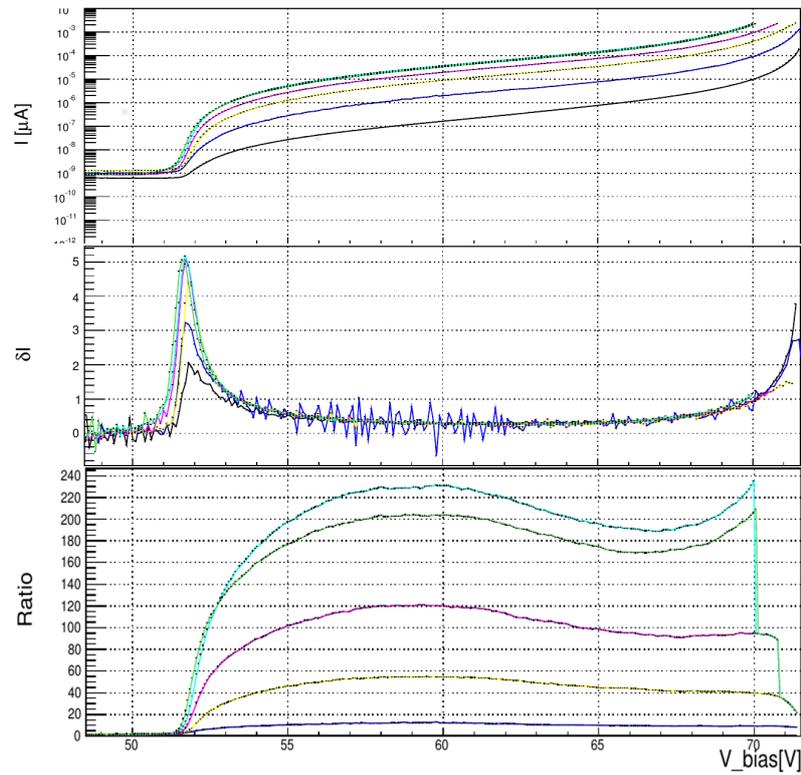
(a) Analysis for each step of irradiation. The colors indicate the level of irradiation: yellow, the lower level; cyan, the higher level.
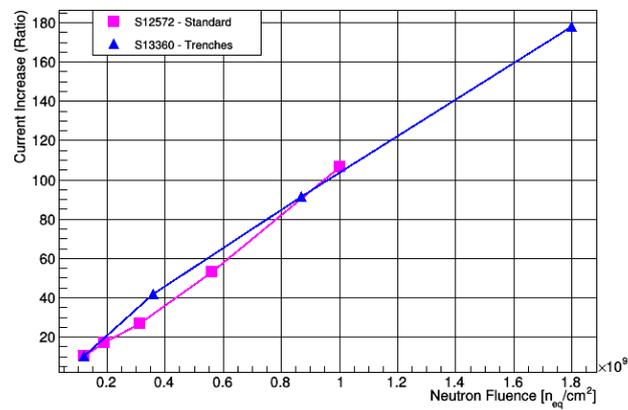
(b) Current Absorption comparison between two technologies

Figure 4.6: I-V analysis

No significative difference is visible between the two technologies in terms of absorbed current. As it is possible to notice, even if exposed at an higher neutron fluence with respect to the old technology, the trench technology shows the same trend of current increase. The new technology does not bring an improvement in radiation hardness despite it is designed to suppress secondary discharges. In order to understand this surprising result, the second analysis method is needed.

Dark Count Signal Analysis The aim of this part of the analysis is to recognize and distinguish single micro-cell discharges with respect to multiple micro-cell discharges. The measurements in this case are performed at $0°C$ to reduce the background. Fig. 4.7 shows the typical SiPM sampled signal before (top) and after (bottom) irradiation. In the same time window, chosen as example, it is possible to see that after irradiation the signal is much more noisy and there are many more pulses.
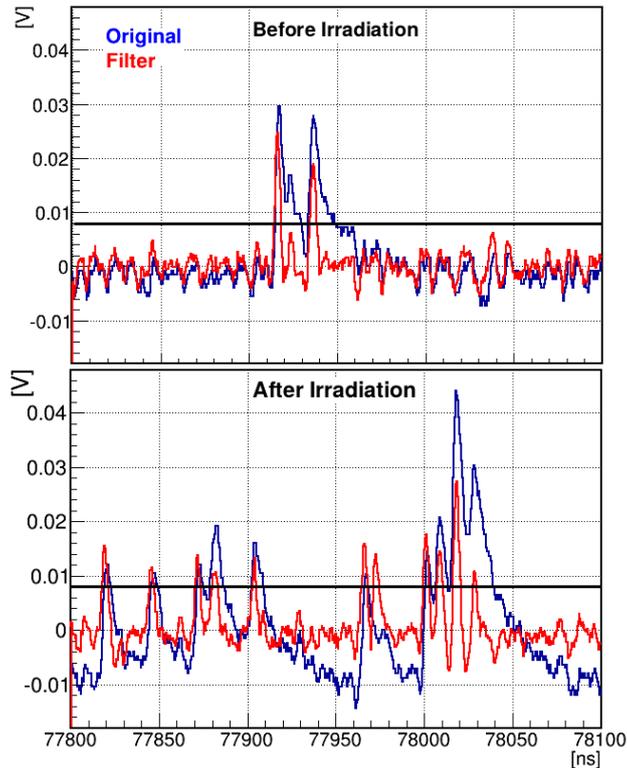

Figure 4.7: Example of the SiPM signal as sampled by the oscilloscope before (top) and after (bottom) irradiation

The analysis runs over the entire spectrum acquired by the oscilloscope in the
20 ms time window, looking for single pulses. For every detected peak, it
calculates the normalized area as a multiple of the expected single pulse. By
collecting the amount of single peaks, with respect the multiple peaks, it is
possible to built the plots shown in Fig. 4.8, where the number of counts are
shown as a function of their normalized area. This representation is useful to
compare the two tecnologies before and after irradiation. The plots on top
represent the situation before irradiation and the plots in the bottom show
the one after irradiation. On the left plots the standard technology and on
the right plots the trenches technology are presented. As the S12572 SiPM
has been irradiated up to $1 \cdot 10^9 \, \mathrm{n_{eq}/cm^2}$, while the S13360 SiPM has been
irradiated up to $1.8 \cdot 10^9 \, \mathrm{n_{eq}/cm^2}$, the dashed line on the right plots shows the
results for the standard geometry normalized to the same neutron fluence of
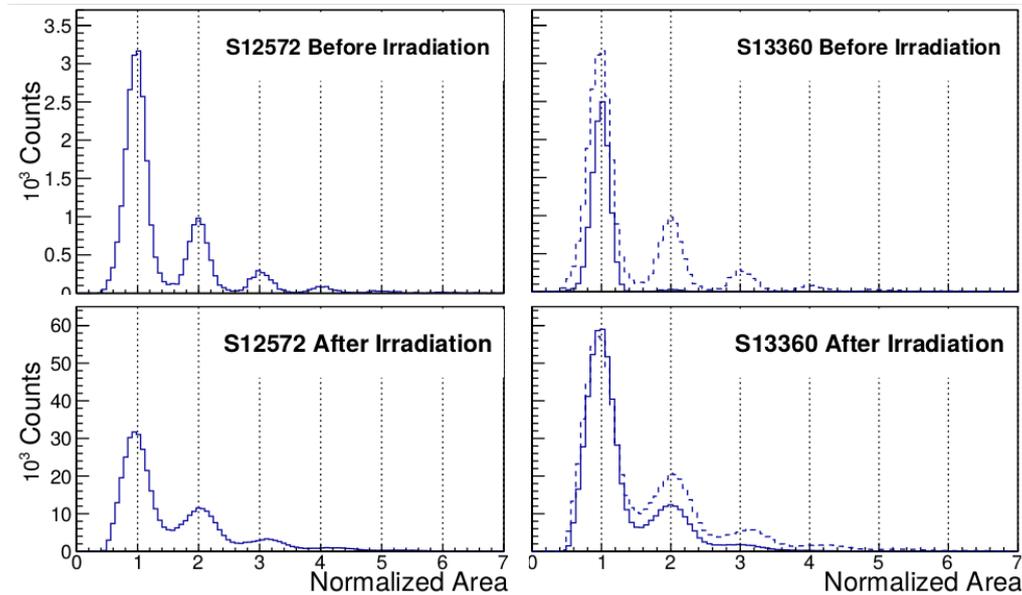the trench one.

Figure 4.8: Area of the pulses normalized to the single pulse. (Top) Before
irradiation. (Bottom) After irradiation. (Left) Standard geometry. (Right)
Trench geometry; the dashed lines represent the standard geometry curves
normalized to the same neutron fluence of the trench geometry.

The first important thing to notice is that in all the conditions the single pulses
are always distinguishable and separated from the multiple ones. The compar-
ison between the device responses shows that multiple disharges, correlated
with the presence of cross-talks, are largely suppressed by the trench with

respect to the standard geometry in the original conditions. However, it indicates that the trench technology is more sensitive to the neutron fluence. This SiPM shows a negligible level of multiple pulses with respect to the single ones before irradiation, but, with the increasing of the neutron fluence, it almost reaches the condition of the standard geometry SiPM whose multi-discharge probability does not change too much after irradiation as it was already high before due probably to thermal effects.

There is no evidence of afterpulses, one of the specific noise source investigated, regardless of irradiation. They should have appeared as a secondary pulse separate in time from the original discharge, with an amplitude lower than the single pulse and depending on the delay, i.e. the time available for cell re-charge. The plots do not show any shoulder on the left of the single peak. This is a consequence of the lately improvements in the quality of the silicon material used in the SiPM production and an example of how the rapidily evolving technology opens new opportunities for SiPM use in Cherenkov application.

The dependence with the neutron dose is presented in Fig. 4.9 where the blue triangles indicate the new geometry and the magenta square represent the standard one. On the top, Fig. 4.9a pictorically illustrates a primary micro-cell discharge (in red) generating two secondary micro-cell discharges (in cyan) on the same SiPM. On the bottom left, Fig. 4.9b shows the rate of the primary discharges as a function of the neutron dose. On the right, Fig. 4.9c present the secondary discharge fraction, i.e. the ratio between the secondary discharges over the total, where the latter has to be intended as the number of events multiplied for their molteplicity with respect to the single pulse recongnized. The secondary fraction is pretty high even at low (or zero) fluence in the standard technology with a value around 50%, while with the trench geometry the same fraction have been halved and its values float around 20%. As discussed above, this reflects in a not significant difference in the increasing of the absorbed current in the two technologies.

Comparative Analysis   The last part of this section presents a test to validate the dark count signal analysis by comparing the outcome of this new technique with a more standard one such as the I-V characteristic curve. For this purpose, a new set of measurementes at 22°C has been performed one year later the irradiation test in both cases, I-V and dark counts analysis. For the dark count signal analysis, different samplings of the signal have been taken with the same time window but different bias voltages in order to have more than one point to be compared with the characteristic curve.
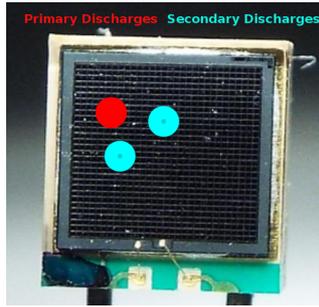
(a) Primary (red) and
two secondary (cyan)
discharges adding into a
single SiPM signal.
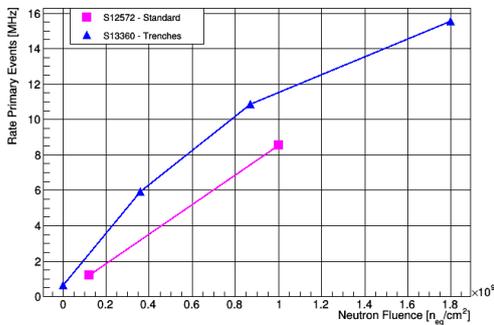
(b) Rate of the primary discharges
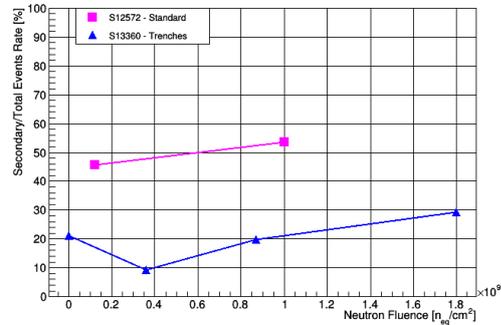
(c) Ratio of the secondary discharges on
the total number of discharges

Figure 4.9: Trend of primary and secondary discharges as a function of the
neutron fluence

In Fig. 4.10 the current is presented as a function of the bias voltage. The
empty markers represent the I-V characteristic as introduced before, while the
full ones are extracted from the dark count signal analysis. The black color
indicates the situation before irradiation while the red one is after irradiation.
For the comparison, the dark current was estimated as the product of the total
number of discharges multiplied by the single pulse amplitude at that overvolt-
age. The total number of discharges was estimated by counting the discharge
multiplicity for each pulse detected. This product should be proportional to
the measured dark current: to be able to overlap the estimated and measured
dark currents on the plot and facilitate the comparison of the trend, an arbi-
trary constant factor has been adopted for all the technologies.
The two analyses give consistent results: the dark count signal analysis is

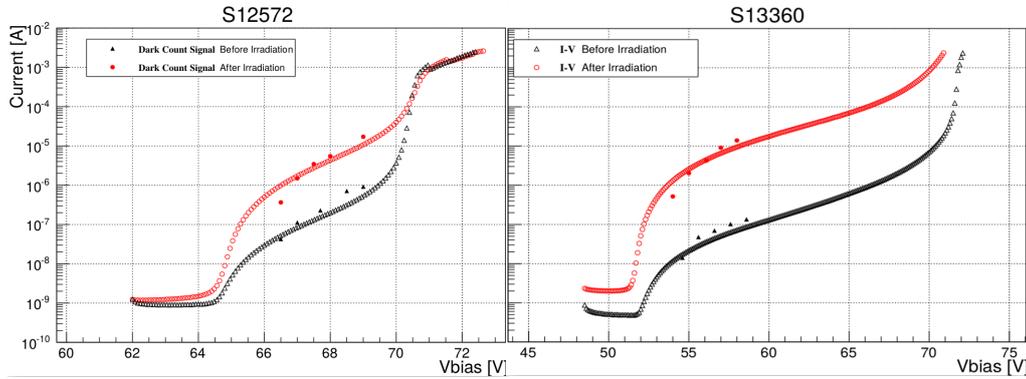validated and their results are compatible either before and after irradiation.

Figure 4.10: Comparison between the I-V (Empty markers) and the dark current (Full marker) analyse

4.2.4   Summary

The irradiation test on the $3 \times 3\,\mathrm{mm^2}$ SiPM samples has been run over various devices: different producers, different micro-cell sizes and different technologies. For simplicity, in this chapter the major outcomes of the study have been presented for a relevant case, the Hamamstsu $25\,\mu$m micro-cell size in both techologies (standard and with trenches) tested at $22\,^{\circ}$C. To deeply investigate the behaviour of the noise in this devices as a function of the irradiation, the analysis has been divided in two branches: the standard I-V characteristic curve and the dark count signal analysis, a new development. As presented in the very last paragraph, the two studies provide comparable results both in non-irradiated and after irradiation conditions. This validated the second part of the study, which for the first time analysed the irradiated SiPM signal sampled at the oscilloscope to isolate the various dark noise components.

The I-V characteristic analysis highlights that the condition of the SiPM device get worst with neutron irradiation. With the increasing of the neutron fluence the absorbed current increases by order of magnitudes. No significant improvement has been observed with the new trench technology with respect to the standard one. The dark count signal analysis indicates that the trench technology ensures a much cleaner condition before irradiation, with a reduced dark count rate and a negligible probability of secondary discharges due to optical cross-talk. Nevertheless, the SiPM with trench geometry still gets worst response with the increasing of the neutron dose, rapidly approaching the standard SiPM performance. No evidence of afterpulses were recorded for

both technologies, regardeless of irradiation, indication of a high quality silicon material.

As a positive sight, in both technologies it is possible to distinguish the single and the multiple discharges both before and after irradiation. This list of tests and analyses indicate that the SiPMs can be used as single-photon detectors at the neutron fluence expected in the CLAS12 enviroment. The most important element to be kept under control in the Cherenkov application is the dark rate. The analysis tool developed as part of this work investigated its detailed behaviour. The increase of dark current due to the optical cross-talk affects the linearity of the device response and is an issue for e.g. calorimetry. In single photon application, optical cross-talk is not a problem as what matters is the ability to distinguish a pulse initiated by the photo-electron. The software filter here discussed is an effective way to clean the SiPM signal to maximize the ability to resolve the pulses and achieve a good time resolution.

4.3   SiPM Matrices

In this part of the chapter the tests just started with the SiPM matrices will be introduced. The work is at the beginning since SiPM installation in CLAS12 RICH is foreseen in few years from now. It is intended to develope a characterization process of these innovative devices.

After the validation of the prototypes in terms of dark count with irradiation, it is time now to start the tests with some products closer to the final ones that will be used in the final second sector of the detector.

The matrices are arrays of SiPM in a common substrate: they allow a compact alignment of each single device with a reduced dead area and a common bias. Their behaviour and usage is comparable with the one of multianode-photomultiplier. They have to be tested with the final readout electronics.

Several samples of matrices are now under testing to deep investigate their behaviour in different enviromental condition. A sample of them are presented in Fig. 4.11: from the left to the right, a 4×4 Advansid NUV_3S matrix connected to an INFN custom adapter board, a 4×4 Hamamatsu matrice with S12642 SiPMs directly installed on another kind of adapter board still custom INFN and a 16×16 Hamamatsu matrice with S12642 SiPMs. All the adapter boards have been studied and produced to be connected to the ADAPTER BOARD as the one presented in the MAPMTs chapter (as shown in the picture), or directly to the ASIC board.

The first matrix shown on the left is the one under test in Ferrara on a laser stand. The actual setup is the one without the second adapter board: the matrix is connected to the INFN adapter board and then directly to the ASIC
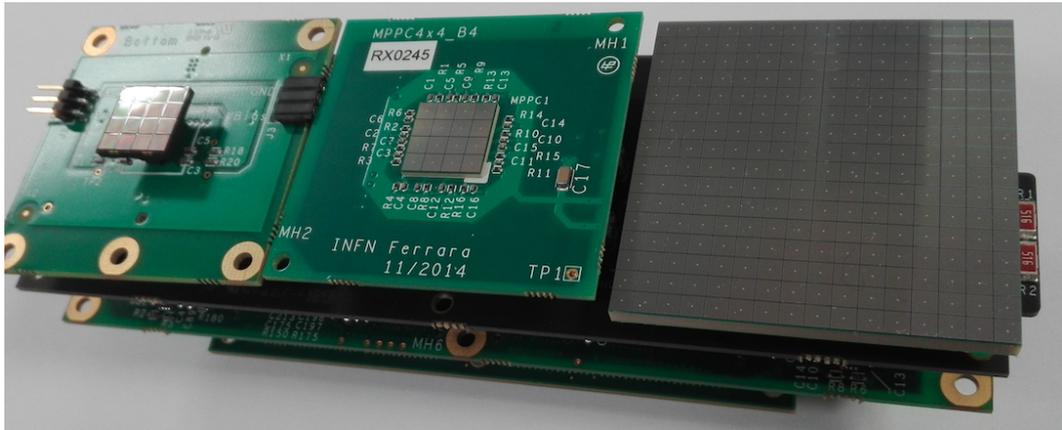
Figure 4.11: Example of SiPM matrices to be tested

board.

In the following lines the setup will be introduced as first, then a brief explanation of the analysis will be given and, at the end, a very preliminary result on the small matrice shown on the left of Fig. 4.11 will be presented.

4.3.1 Setup

As already mentioned, the setup for the test of the SiPM matrices has been prepared in Ferrara. The laboratory has a dark box and the SiPM setup has been installed inside and shown in Fig. 4.12:

Laser Source   The laser setup is the same setup used at the Jefferson Lab: it is a PicoQuant unit with 405 nm wavelength laser. Also in this case the head of the laser is mounted on mechanic motors to move it all over the active surface of the sensor and it is possible to install optical density filters to reach the single photon conditions. The movements can be controlled by an esternal PC, while the filters have to be positioned by hand. The laser has been positioned to hit just one pixel of the whole matrix.

Readout Electronics   To readout the signal form the SiPM, as already said, the same electronics developed for the first sector will be employed. This implies the use of the ASIC board connected directly to the SiPM matrices and the FPGA. As it is possible to see from the pictures, they will be positioned between two white plastic layers to hold the tile during the operating time.

Power Supply   To supply power to the full setup it is needed a low voltage source for the electronics board and a high voltage source for the matrices. The HV power supply has been built custom from INFN-FE personnel to have a more precise signal with lower noise. The LV, instead, is a Thurlby Thandar Instruments EX345T power supply triple power supply, but only one channel will be used.

Data Acquisition   It is the same as the one used for the first sector and presented in 3.2.1.
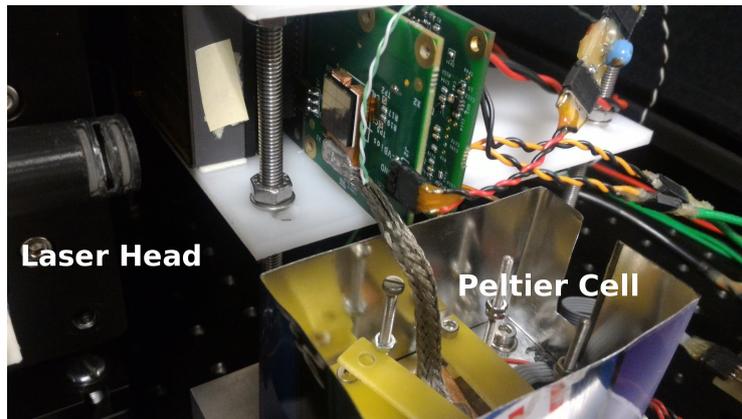

Figure 4.12: Laser setup in Ferrara inside the dark box

4.3.2   Analysis

This part will be kept short since the readout is the same presented in the MAPMTs' part.
Even if the MAROC allow to extract both the analog and the digital information from the signal for each channel, here the analyses run will be focused on the second one, correlated with the time measurements, already introduced in the section 3.2.2. The two main quantities to describe the behaviour of the devices are:

- **Hit time** It is the time stamp assigned by the elctronics to the leading edge of the signal.

- **Time Over Threshold** It is the difference in time between the trailing edge and the leading edge. It is the quantity proportional to the amplitude of the signal and therefore to the charge.

4.3.3   Results

This section shows the very first result from the SiPM matrices setup. The analysis is still on going, but Fig. 4.13 present a first scatter plot of the hit time distribution as a function of the time over threshold at 22°C for the single channel hit by the laser. Already at this temperature it is possible to see the signal of the single photon as the cluster with duration between 40 and 60 ns with a hit time around ~ 165 ns. It is possible to see another small accumulation between 80 and 100 ns that can be associated with double peaks, indicating a photon counting capability. Moreover, a vertical band with the same duration time of the signal shows up: it is an indication of the dark counts that have the same discharge properties of the single photons
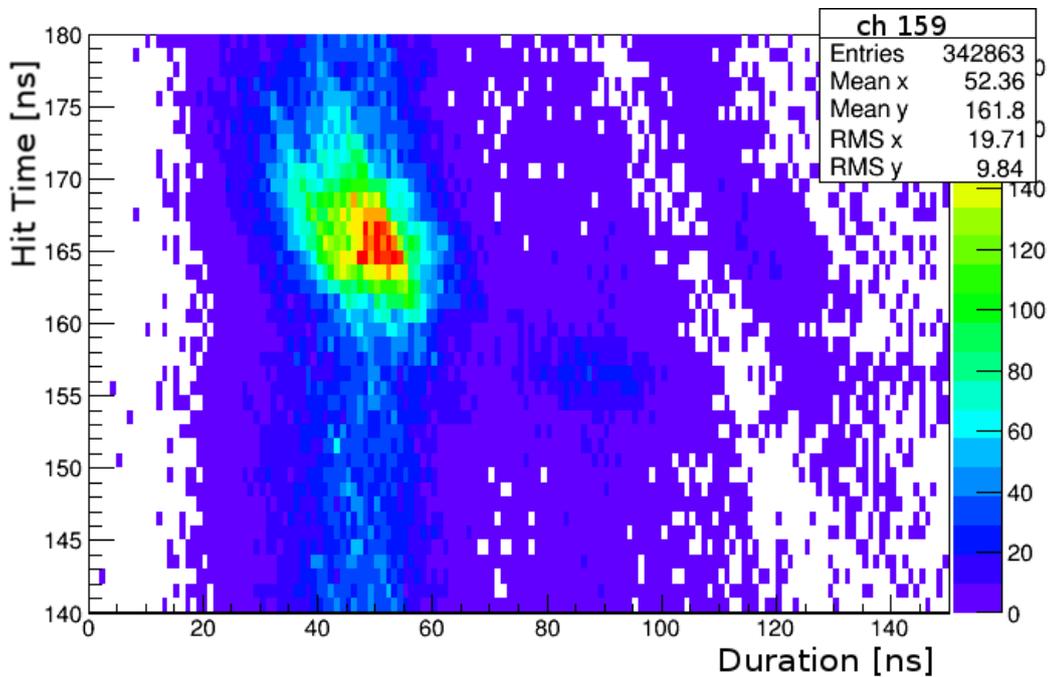

Figure 4.13: Hit time vs Time Over Threshold Distributions

4.3.4   Summary

The SiPM matrices validation follows the work done on on the $3 \times 3\,\mathrm{mm}^2$ SiPM samples. It is still in a preliminary stage of analysis, since the installation of the second sector of the RICH with the SiPM is planned to be in few years. The setup prepared in Ferrara to study the SiPM included a dark box were the

SiPM matrices connected with the RICH readout could be placed in front of a laser source. This kind of test is important to check the performance of the SiPM with the readout already in use for the MAPMTs. The first analysis, presented in this chapter, had as a goal to be able to see the signal from the laser with the proper timing. Since during the physics run a digital readout will be used, while the analog information will be used during calibration run, the first quantity to be focused on was the time. The hit time indicates when the event occurs with respect to a reference clock beat. The hit duration is an information correlated with the injected charge. The preliminary results allow to confirm that these devices are working properly with the existing electronics. The other important feature to investigate is the possibility to work with a fixed threshold to discriminate the signal: this implies study the behaviour of the baseline together with the dark counts. Before the final sensor choice, more investigation and studies have to be performed to improve the knowledge of the features of the SiPMs in conjunctions with the RICH electronics. Some test could be performed at lower temperature to reduce the background, but also other kind of SiPM matrices could be investigated since the SiPM technology is improving fast.

4.4 Conclusions

A first validation of the use of the SiPM in Cherenkov applications has been provided from a beam test at the T9 beam line in the CERN-PS East Area done with a small RICH prototype together with other studies on different experiment as presented in [40]. The SiPM technology has been chosen to substitute the MAPMTs as a photon detector thanks to the reduce cost and to the spatial and time resolution that can reach. A typical drawback of this tecnology, however, is the sensitivity to the radiation damage. It has been proved in this work that the CLAS12 radiation enviroment is sustainable by this technology that is still able to discriminate single photons after several years of data-taking.

Further tests has been presented on the SiPM capability to work with the RICH readout already in use. The preliminary result shows that it is possible to distinguish the single photon signal from the background of the dark counts and also to discriminate single and multiple discharges.

These studies are still on going to be sure to chose the right sensor to work in the CLAS12 enviroment to have the highest performances.

Chapter 5

Commissioning of the RICH Photon Detector

This chapter's goal is to describe the assembling of the active part of the RICH detector and to present the first analysis on the data collected during the run with cosmics. In this section a brief explanation about the mounting procedure for the initial small setup and the full system will be presented. Another section will be dedicated to the functionality validation and the preparation of the photon detector for data acquisition. A succesfull running has been achieved and the first rings from the online monitor can be shown. Finally, some of the first results that have been achieved will be shown even if the analysis is on going to illustrate in particular the time properties and resolution.

5.1   Assembling

After the full characterization at the laser stand was completed, all the readout components were ready to be installed on the electronic panel. Being the most complicated element of the detector, joining several active subsystems, the electronic panel has been assembled as a stand alone piece on its own support. To prevent any issue correlated with the assembling and to better understand the mounting process not to occur in any error, the assembling was staged into two phases. In the first phase, a limited amount of tiles were installed covering about one forth of the surface. The number was enough to equip a cosmic stand to detect the Cherenkov light produced by cosmic muons passing through a tile of aerogel. Despite the different geometry, the setup allowed to develop and check all the subsystems: communication protocols of the front-end with the data acquisition, trigger and clock distribution, slow control, hardware interlock, event display. After few weeks of data taking, the small cosmic

stand was dismounted. In the second phase, the full panel has been assembled together with the upgraded version of the services and later on completed with the gas systems (cooling air and nitrogen). A second campaign of cosmic data allowed to verify the full functionality of the system.
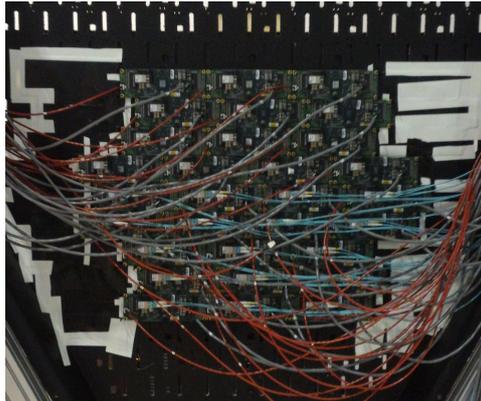
5.1.1   Small Cosmic Stand

In Fig. 5.1 few pictures are shown to documentate the assembling of the different components. About one forth of the panel, corresponding to 30 tiles, was instrumented. Two additional tiles were instrumented in a separate station for tracking and triggering. For practical reasons, the covered area was in the middle of the panel. The tile number was restricted by the first simplified version of the data-acquisition system. The tile distribution was optimized for the cosmic run, suitable for the detection of the Cherenkov ring and compatible with the coverage of an available black cylinder. The 32 tiles have been chosen in order to be all 3 MAPMTs version; mount both MAPMT types, H8500 and H12700; have most of the MAPMTs at average gain but 2 samples at high gain and 2 at low gain.
The mounting proceeded with the following steps.

(a) **Adapter boards:** they have to be installed on the internal side of the panel to give support to the MAPMTs while being electronically connected with the readout on the outer side. They are anchored to the panel with screws and nuts, see Fig. 5.1a.

(b) **Asic boards** and **FPGA boards**: the asic and FPGA boards were mounted in a row before connecting the cables, see Fig. 5.1b. First to be plugged were the low voltage cables: this allowed to check the connections between the boards through the absorbed current and the configuration protocols. Then the high voltage was cabled to provide power to the adapter boards for the MAPMT sensors. The absorbed current was verified with a test sensor: some HV connectors with problems could be rapidily replaced without any change on the other parts of the setup. The last item was the optical fibers as they are the most fragile cables. At that point it was possible to run the data-acquisition system to do a quick check of the hardware status and exclude any sub-optimal working condition or damage.

(c) **MAPMTs**: this operation had to be done in dim light to keep illumination as low as possible in order not to activate and maybe damage the photocatodes. Furthermore, the photomultipliers could not be plugged
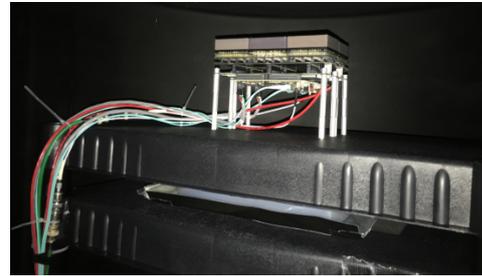
(a) Adapter view
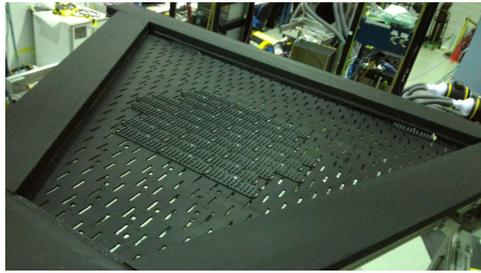
(d) Aerogel and Trigger view

(b) Electronic boards view

(c) MAPMTs view

(e) Full setup

Figure 5.1: First cosmic stand.

either with their proper cover cups or by touching the frontal glass window. For this reason a peculiar ordering of installation was studied that allowed to always have half of the sensor perimeter free for pick and plug: exploiting the staggering of the MAPMTs in adjacent rows, the mounting proceeded from left to right plugging by columns. Fig. 5.1c shows the MAPMT layer surrounded by the black cylinder acting as a cosmic box, with visible the four legs of the tracking station support.

(d) **Tracking** and **aerogel**: they were placed inside the dark cylinder to generate the ring. The tracking station is composed of 2 tiles assembled exactly like a standard tile on the electronic panel, see Fig. 5.1d. Each tile generates a prompt digital signal as an OR of all the connected anodes. These signals could be put in coincidence with the signals of two scintillators to generate the trigger. The aerogel is a 20×20 cm^2 tile that, placed on top of the MAPMT layer at a height of 60 cm, allows to fit a Cherenkov ring on the installed tile array.

(e) **Full setup:** it is visible in Fig. 5.1e. The electronic panel is kept horizontal to maximixe the cosmic flux and to facilitate the stand assembling. The black cylinder hosted, at the top, the trigger tiles and the aerogel, and, at the bottom, the MAPMTs. The readout boards were attached to the bottom of the electronic panel. Below the panel there were a fan to guarantee the cooling and, under it, the two trigger scintillators.

This setup allowed to acquire experience in all the phases of the assembling in preparation for the complete panel instrumentation. The mechanical procedures were optimized, the functionality test defined (to identify badly connected boards, swapped cables, missing or malfunctioning parts). All the sub-systems except the cooling were connected and commissioned, at least in a simplified version. In particular, only one 8-channel low-voltage and one high-voltage board out of five were employed. The DAQ was based on one Sub System Processor (SSP) board out of the five foreseen for the final setup, without the need of a common clock and trigger distributor. The limited amount of boards did not required a sophisticated data-acquisition protocol to provide reliable and fast connection in all the conditions. Only basic configuration options were activated and no calibration algorithms applied.

Once all the problems with the small setup were solved and how to use the acquisition program has been learned, the data collection started.
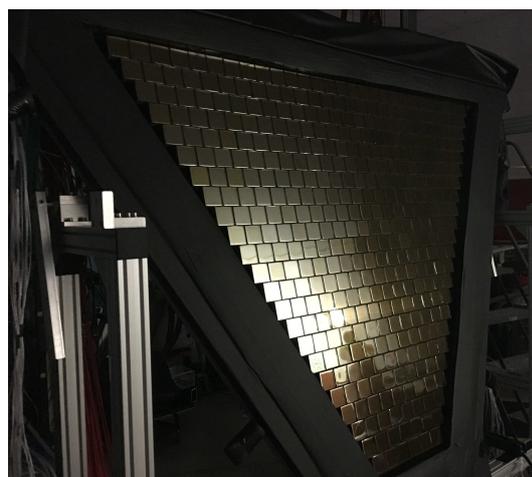
5.1.2   Full Cosmic Stand

After few weeks it was time to equip the full electronic panel. Every component of the small cosmic stand was dismounted not to damage the MAPMTs with light and to better anchor the adapter boards after some mechanical evaluation of the structure.
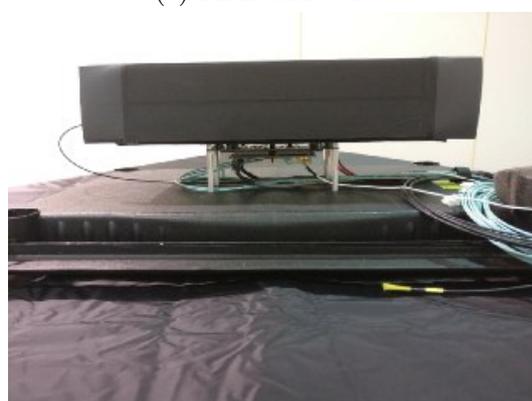
In Fig. 5.2 several pictures show the assembling of the components of the full electronic panel. The same mounting steps explained before for the small setup have been followed for the complete system: adapter boards (Fig. 5.2a), front-end electronic boards and cables (Fig. 5.2b), photomultipliers (Fig. 5.2c),
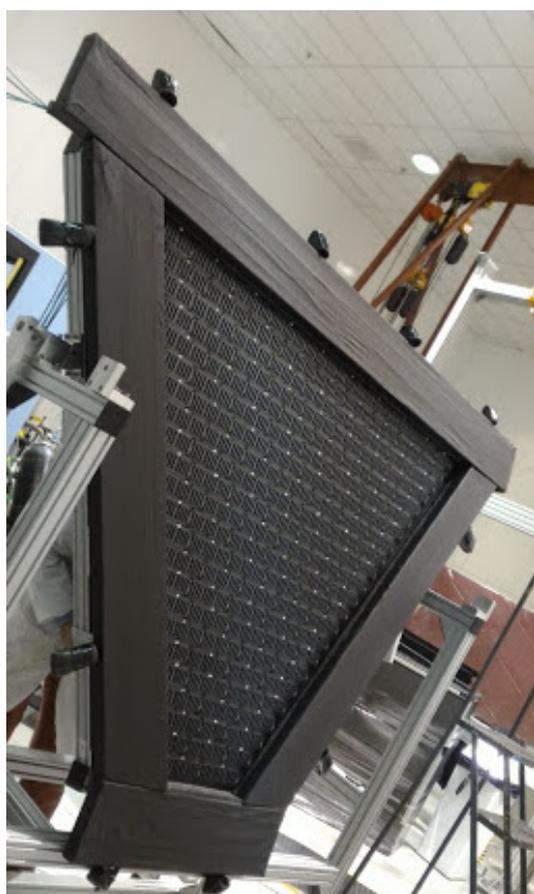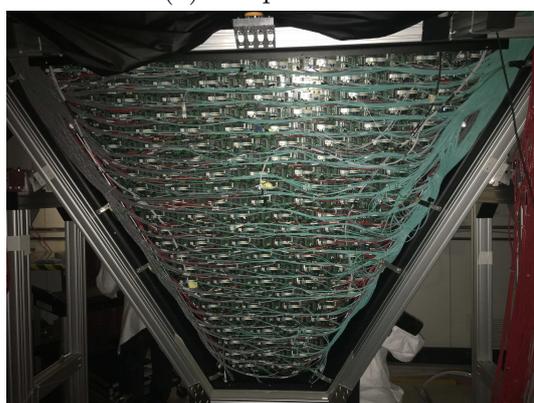
(a) Adapter view

(c) MAPMTs view

(d) Trigger box

(b) Electronic boards view

(e) Full setup

Figure 5.2: Final cosmic stand.

trigger station (Fig. 5.2d) placed on top of the dark box. Fig. 5.2e shows the completed system: the big dark box covers the full electronic panel that in the cosmic run configuration is rotated in a horizontal position. On top of the box there is the trigger station comprising of 2 tiles (6 MAPMTs) connected with a logic OR with two scintillators placed at the bottom of the setup. In the pictures two big fans are visible, used to help cooling down the electronics before the designed cooling system had been activated. At the time all the power supply boards for HV and LV were in use and also all the 5 SSP readout boards were connected.

Once everything was setup and all the channel proved to respond properly, the data acquisition started.

5.2 Functionality Tests

Both the setups worked properly. Several tests have been done to be able to check the functionality of the photon detector in all its components. As first thing, it had to be checked that it was possible to see a Cherenkov ring. Later on, the work has been focused on the slow control and online monitor, on the optimization of the noise condition and on the performance assessment.

5.2.1 Cherenkov rings

After every tile was turned on and all the sub-systems were confirmed to work properly, the data acquisition was started to initially verify that it was possible to record some Cherenkov rings. Even without any quantitative information, a Cherenkov ring would have provided the first evidence of the healty of the system and the starting point for the full photon detection optimization.

Small Setup   Fig. 5.3a shows an example of what could be seen with the first small equipped setup. On the left of the picture, the six yellow squares represent the six MAPMTs that compose the trigger together with the two scintillators. On the right, all the instrumented PMTs of the electronic panel are shown. The magenta points are the pixels firing on a specific event. The clusters derives from the cosmic ray passing through the system while the single pixels distributed in a circular pattern around a central cluster highlight the Cherenkov ring produced by the aerogel. A satisfactory number of cosmic events could be collected even with this small setup.

Full Setup   A ring extracted from this setup is shown in Fig. 5.3b. Here only the PMTs on the trapezoidal electronic panel are shown. The description

of the firing pixels follows what has been just presented in the previous paragraph. A remarkable notice is that an acquisition time window of 1 μs was used and no selection of hits was applied. The outcome dimostrates the low level of background that is possible to achieve with this kind of photomultiplicators.

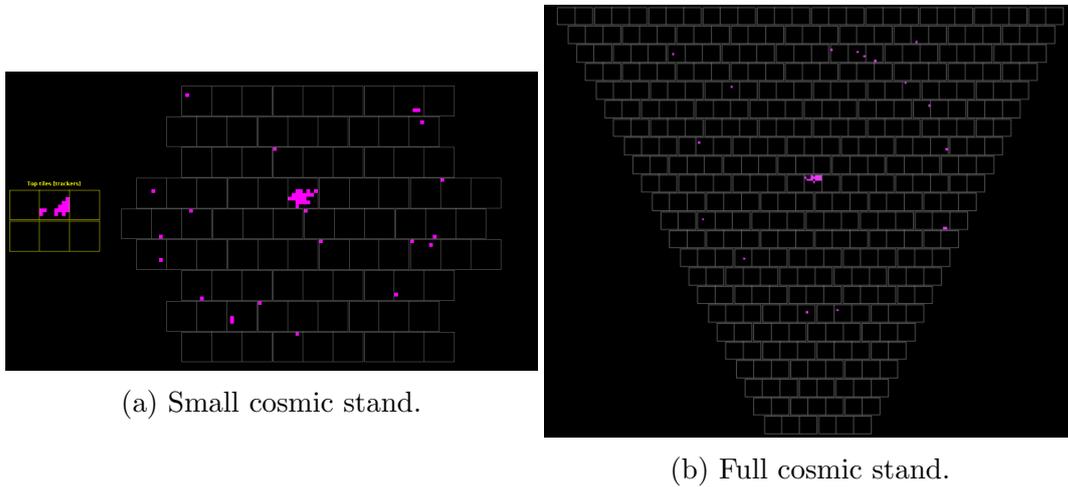(a) Small cosmic stand.

(b) Full cosmic stand.

Figure 5.3: Example of events with Cherenkov ring

5.2.2   Slow Control

The next step in the functionality checks was to test the ancillary systems: monitor the temperature of the boards and the stability of the MAPMTs. This was done through the online monitor interface developed for the RICH.

Temperature   A cooling system has been studied to prevent the overheating of the front-end boards once they are closed inside the RICH module. Several external sensors will be placed around the mechanical structure of the detector to serve an hardware interlock, but there is also an on-board sensor on each FPGA board. Fig. 5.4 shows the temperature map in use with the FPGAs information. A value per each tiles is registered every few seconds. The color scale helps to visualize dangerous conditions or to check the uniformity of the system: the yellow-green region indicates a standard condition at which the temperature is a bit above the environmental temperature and there is no risk for the instrumentation; the blue one highlights a colder temperature, that could be likely correlated with a turned-off board; the red color indicates a dangerous condition above which the components can be permanently damaged.
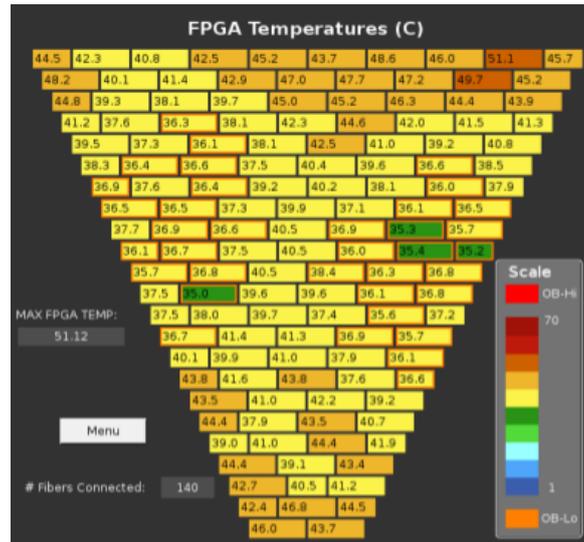
Figure 5.4: Example of the online monitor of the FPGA board temperature.

Scalers A way to check the performance of the MAPMTs through the electronics are the scalers implemented in the FPGA firmware: they are a counting system to register the number of detected pulses on a preset amount of time. On the online monitor, presented in Fig. 5.5, the rate averaged over the 64 pixels of each PMT is shown. It allows to immediately check the status of each device. On the right, the blue area corresponds to not-illuminated MAPMTs and reports typical dark counts values around 10 Hz. On the left, the yellow-green area with higher rates corresponds to MAPMTs illuminated by a optical fiber with a LED in single photon conditions. As it is possible to see in the picture, some of the MAPMTs present an high rate while others do not, but, since the LED illumination is supposed to be constant in time, also the response map should be and provide a check of the stability of the system. In some cases, red spots signal the presence of malfunctioning pixels called hot as they presents an abnormally high rate. The interface allows to click on each MAPMTs to visualize the status of each pixel and check if any is dead or too sensitive.

5.2.3 Noise

The first checks with the slow control monitor allowed to spot an issue with noisy pedestals on the boards. The average and RMS of the pedestal values without any photon striking on the PMTs is an indicator of the noise on the electronic chain. In Fig. 5.6 the evolution of the performances in terms of
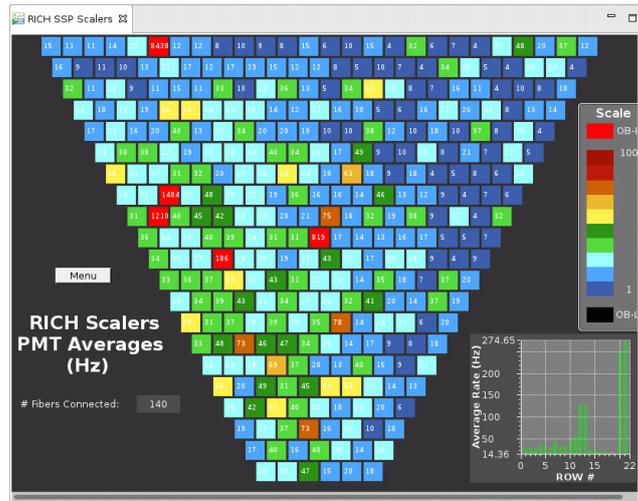
Figure 5.5: Example of the online monitor of the boards scaler.

reduction of the spread of the pedestal distribution is shown. On Fig 5.6a the pedestal RMS of each pixel is presented in ADC units on the z-axis. The situation is not as uniform as expected: the boards do not have a common groud and this results in having some noisy channels. The solution found to this problem was to connect each board to the others and all together with the frame: in this way all the boards have the same ground and the flaoting baseline level is common over all the channels. An improved situation is shown in Fig. 5.6b when only a partial grounding grid was installed.
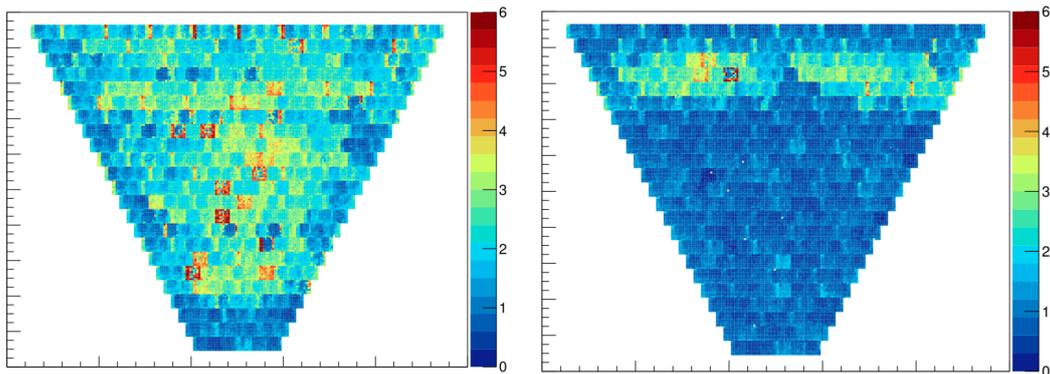
(a) Before correction

(b) After Correction

Figure 5.6: Pedesal RMS values as measured for all the channels.

111

5.2.4 Online Monitor

Finally, together with the online monitor for the slow control of the healty parameters, another online monitor to follow the physics events and the data acquisition performance has been developed and improved with growing requirements during the commissioning phase. An example of what is possible to monitor is shown in Fig. 5.7:
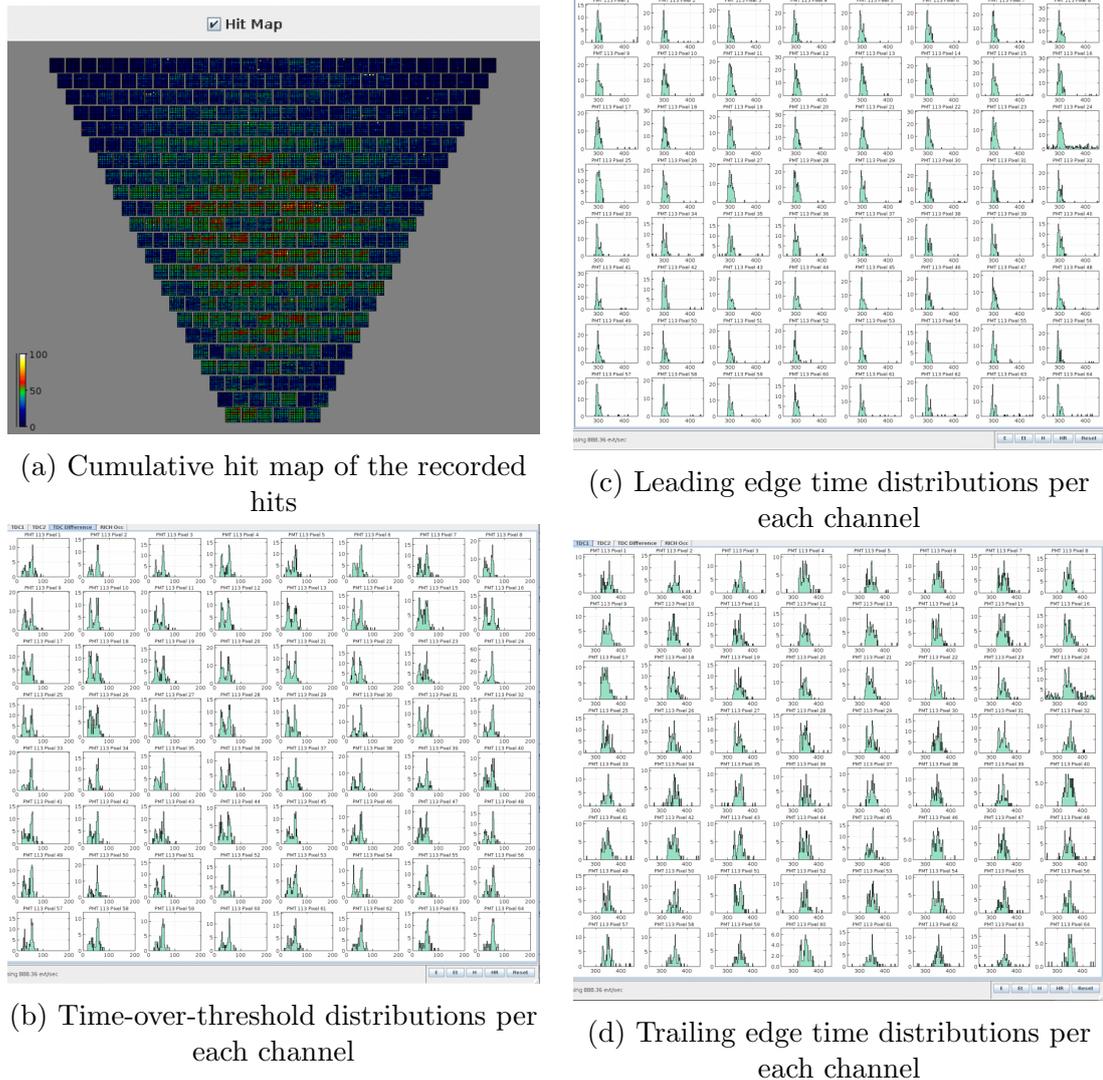

(a) Cumulative hit map of the recorded hits

(c) Leading edge time distributions per each channel

(b) Time-over-threshold distributions per each channel

(d) Trailing edge time distributions per each channel

Figure 5.7: Data acquisition online Monitor.

Fig. 5.7a shows the cumulative hit map that allows to see how the events distribute in the area of the photon detector.

Fig. 5.7b shows the distribution for each channel of the time-over-threshold which is the difference between the trailing and the leading edge and is the quantity extracted from the digital measurement proportional to the charge of the photon that strikes on the PMT. The x-axis shows the time in ns while the y-axis the occurency.

Fig. 5.7c shows the distribution for each channel of the leading edge time at which the waveform go above the threshold. Also here the time is indicated in ns on the x-axis.

Fig. 5.7c shows the distribution for each channel of the trailing edge time at which the waveform go under the threshold. The time on the x-axis is indicated in ns and on the y-axis there is the occurency.

Such monitoring allows to see if all the MAPMT pixels and readout channels are responding properly. If something changes in the distributions or a signal does not appear, it is possible to act instantaneously to fix the problem by checking the software and the parameter settings.

5.3   First Data

The work on the electronic panel was complete when the hardware and the software were connected and properly comunicating and the slowcontrol and monitor was ready to check that the conditions of the detector could remain stable. Since at that moment the RICH module was not yet completed with the others passive components, it was possible to collect cosmics data for few weeks. In this section, some preliminary results of the analysis on the time response will be described. An explanation on the method and on the results will be presented. It has to be considered that the cosmic setup has been built to mimic the final conditions, but the readout settings chosen are not the final ones, as these kind of tests are precisely intended to learn the working conditions and look up for the best ones.

5.3.1   Analysis

Here the steps of the analysis will be explained, starting from the selection used to identify the good events, ending with the time offset correction applied.

Event Selection   The trigger for the cosmic run was composed by two electronic tiles, exactly like the ones on the electronics panel, connected with two scintillators in a OR logic. This allowed to collect data everytime at least one of these components was crossed by a particle.
From all the events registered, it was necessary to select only the ones that

correspond to a cosmic particle crossing the system and generating a proper
Cherenkov ring. Those have to satisfy the following requirements:

- a cluster of hits is found on the tiles that compose the tracker;
- a cluster of hits is found on the electronic panel.

The cluster is a signature of a charged particle, as it adds up the numerous
Cherenkov photons generated on the PMT window and the ionization electrons
extracted from the dynode structure. After an event is selected, the isolated
hits on the panel are the ones of interest: they are the evidence of a single
Cherenkov photon hitting the panel. For each single hit some parameters are
registered to know specific properties such as the position on the panel and the
time at which the event occurs. Those will be the identification number for
tiles, photomultipliers and anodes, together with the hit time and duration.
Fig. 5.8 shows the time at which the hit occured with respect to the duration
of the signal over threshold. This is a standard plot to have a first look on the
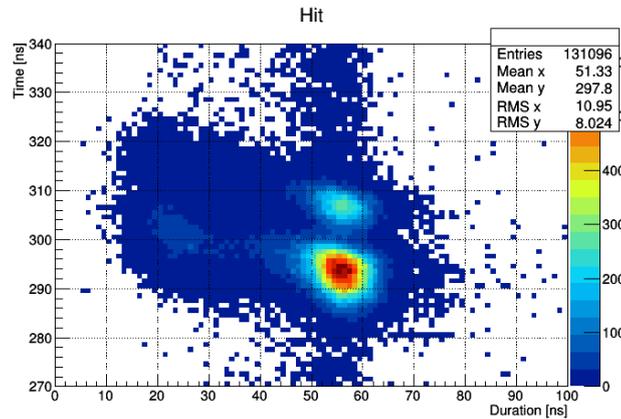

Figure 5.8: Hit Description: hit time vs hit duration.

time properties. Every point on this plot is a single hit. The typical duration
is around 55 ns, whereas the typical delay with respect the trigger is around
292 ns. The tail at smaller duration correspond to incomplete PMT avalches
or cross-talk events, while th evertical band around the typical duration are
out of time hist, i.e. dark counts. The main time selection to run the analysis
would be:

      Hit Time in the range between 280 and 320 ns;

      Hit Duration longer than 37 ns but lower than 68 ns.

The secondary excess at later times around 308 ns is due to a so-called glitch
of the trigger that shifts the event time with respect to the standard time
distribution. This effect is confirmed by Fig. 5.9 that shows the distribution

of the hit time average per each event. The two peaks are still separated by $\sim 10\,\mathrm{ns}$ and this clarifies that it is not a spread in time inside the event but a shift between an event and another. To extract some preliminary results,
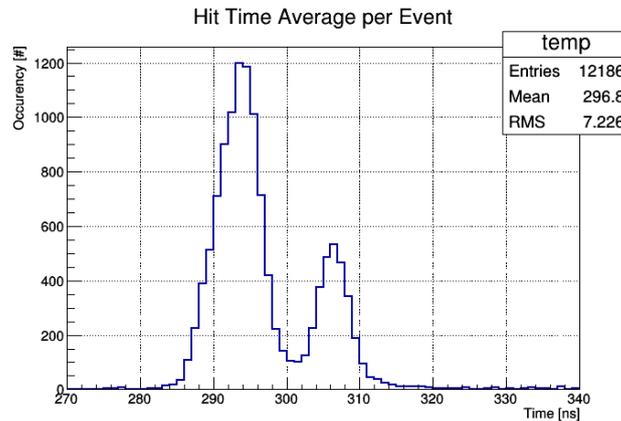

Figure 5.9: Hit time average per event

during this analysis it has been chosen not to consider the secondary peak. This implies that the final requirement for the duration of the signal will remain the same, but the one for the hit time the requirements will select it to be between 286 and 300 ns.

Correction On a setup like the one of large area and high segmentation such is the RICH photon detector, every channel (~ 25000) response can be characterized by a systematic error due to its location with respect to the position on the tile or on the panel. Fig. 5.10a shows the dispersion of the hit time as a function of the tile position on the panel, keeping in mind that each tile can have 128 or 192 channels and the tile enumeration starts from the bottom of the sector. The typical spread inside a single tile is $\sim 20\,\mathrm{ns}$. To have a better time resolution an offset correction needs to be applied at each channel to equalize it with the others. To do that, the average time at which an hit occurs inside a channel has been calculated and used as an offset on that channel for every event.

Fig. 5.10b shows its effects: the hit time is presented with respect to the tiles as before. From the color distribution is possible to notice that the distribution is more uniform around zero but, with the help of the red lined placed just as a reference, it become clear that the correction does not help in resolution. This lower limit of the resolution is correlated with the jitter coming from the 8 ns timestamp precision.
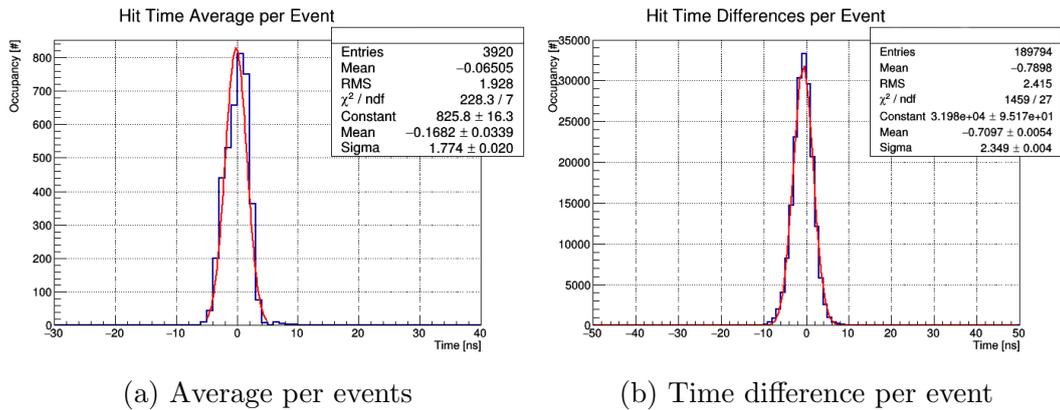
115
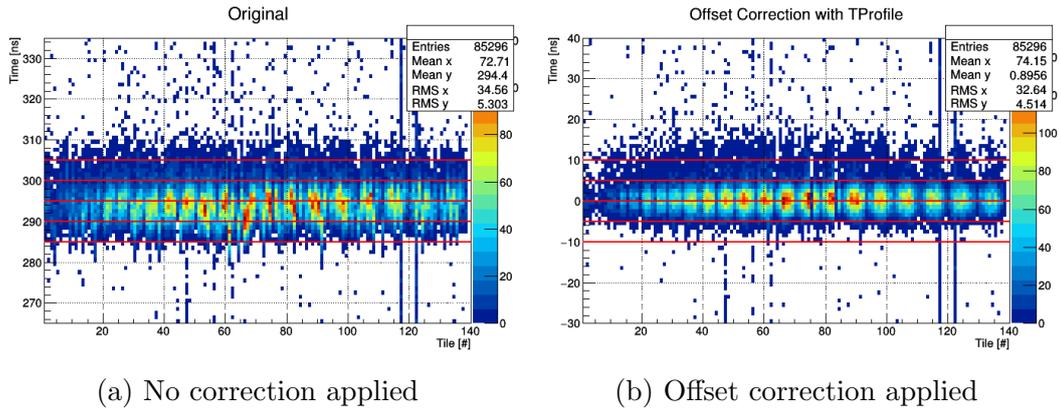
(a) No correction applied   (b) Offset correction applied

Figure 5.10: Hit Correction: hit time vs tile number

5.3.2 Results

In order to extract information about the time resolution of this detector two different distributions of interest for the hit time of each event are shown in Fig. 5.11.
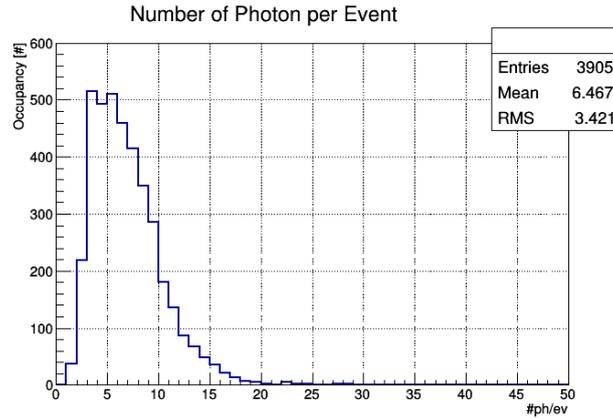

(a) Average per events   (b) Time difference per event

Figure 5.11: Hit time distributions

There the distribution of the hit time average per event and the one of the difference in time between hits of the same event are presented. It is possible to notice also in these plots that the trigger jitter affects the measurement by looking at the σ values of the fits. To compare the two values it is necessary to divide the differences one by a factor $\sqrt{2}$: the lower value is 1.66 ± 0.066 ns. To confirm that is the trigger that affects such measurements, in the following the results for the analysis of the σ of these distribution will be presented as a function of the number of photons registered per event (see Fig. 5.12).
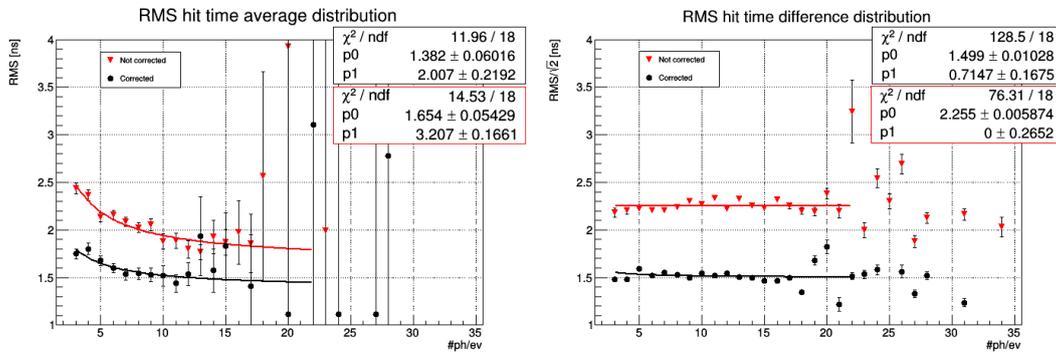
116

(a) Number of photon per event distribution

(b) σ of the average distribution

(c) σ of the time difference distribution

Figure 5.12: σ analysis with respect to the number of photons per event

Fig. 5.12a shows the distribution of the number of single photons detected per events. It is possible to notice that the statistic for this preliminary analysis is quite low and there is a significant occupancy only up to 20 photons per event. A cut has been performed to avoid events with less than 3 photons. Fig. 5.12b and 5.12c show respectively the σ calculation for the average and the time difference as a function of the number of photons detected per event. In the time difference case a $\frac{1}{\sqrt{2}}$ factor is applied because the data derives from a difference among independent measurements. Moreover, here is presented the comparison between the original data (red triangle) and the ones corrected by the time offset (black circles). Those data are fitted, where there is a sufficient statistic, i.e. from 3 to 20 photons, with the following formula:

$$\sigma = \sqrt{p_0^2 + \frac{p_1^2}{N_{ph}}}$$

117

where p_0 is the parameter to indicate the offset and p_1 indicates the error on the single photon.

It is first important to point out that the offset correction helps improving the time resolution in both cases. The time average shows on the final black fit a resolution on the single photon equal to $\sim 2.01 \pm 0.22$ ns that is comparable with the single photon resolution, as should be, and an offset of $\sim 1.38 \pm 0.06$ ns that is mainly generated by the trigger's jitter which is expected to be $\frac{8\,\text{ns}}{\sqrt{12}} \simeq 2.3$ ns for this system. The difference in time between hits, instead, gets rid of the trigger jitter and reveals a resolution almost flat in the number pf photons with an offset value of $\sim 1.50 \pm 0.01$ ns. This is pretty close to the requirements of the detector even if the offset is affected from a non optimal time offset correction due to the trigger issues presented.

5.4   Conclusions

The full photon detector has been validated. A first setup with a quarter of the full panel had been mounted to learn and optimize the assembling procedure. With a temporary black cover it was possible to equip a cosmic stand to validate the software chain with the limited number of units available. Cherenkov rings were detected as a demonstration of the correct readout chain. Subsequently this setup was dismounted and the full electronic panel has been setup. Once the hardware was done, some software tests has been performed on the online monitoring and slow control. They allowed to point out some remaining issues like the noisy pedestals that could be corrected with a groundind grid connecting all the boards together to a common ground. While the passive components were installed on the RICH module, a cosmic stand with the fully instrumented electronic panel, an aerogel tile and two tiles for the trigger, started taking data. The preliminary analysis on a first portion of this data concentrates mainly on the time requirements for the RICH. Some software correction has been applied to correct the time offset and equalize the channels. By construction, the temporary cosmic setup does not have all the accuracies of the final detector and some trigger issues showed up. The time resolution reached is $\sim 1.50 \pm 0.01$ ns and it is close to the one expected. Such value is still a reflection of the cosmic trigger jitter. During the experiment a much better time resolution will be reached thanks to a better optimization of the trigger and also to the help of the other detectors. Further investigation are on going to study all the properties of the detector, such as the Cherenkov angle identification.

At the end, the completed panel has been installed into the RICH module and extensive tests of all the subsystems have been performed. After having

completed such a validation, the aerogel has been installed, the RICH module closed and the gas system validated, before moving the detector to the experimental hall. Recently the RICH module has been installed in the experimental hall and it is now working properly. The first data from calibration run are now available. Fig. 5.13 shows the time duration distribution for different configuration tested: different discriminating TDC threshold and MAROC gain are applied. Their effects are clearly visible and affect the shape and the offset of the distributions as it was measured with the laser stand data. It has been decided to start the production run with the green configuration (+25 TDC threshold) of Fig. 5.13c where the distributions are narrower even if a cross-talk signal is present, since the software tool developed is able to distinguish it from the main signal.

(a) Without correction gain (g=0)
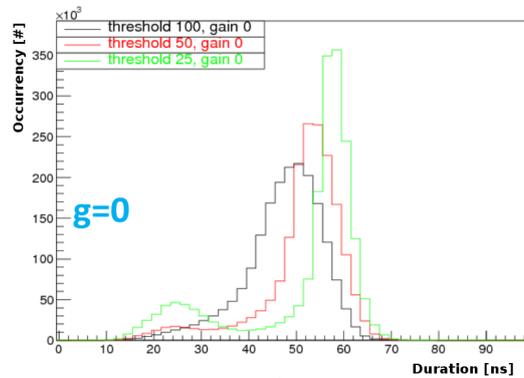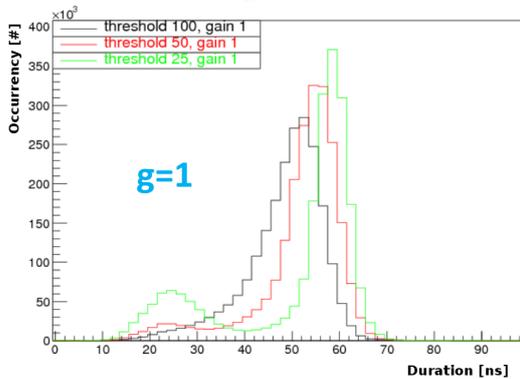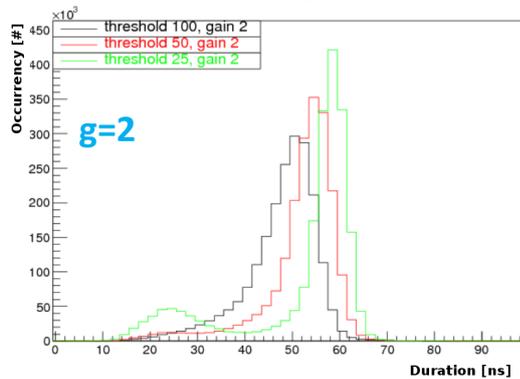

(b) With amplification of the lower signal pixels only (g=1)

(c) With equalization of all the pixels to an average value (g=2))

Figure 5.13: Hit duration distribution for different discriminating thresholds from calibration run data.

Chapter 6

Conclusions

The author's contribution to the CLAS12 experiment with the RICH detector is divided in two main parts involving the innovative photon detectors chosen for the two sectors that will compose the full experimental setup: Multi-Anode Photomultipliers and Silicon PhotoMultipliers.

The author followed the validation and preparation of the photon detector based on MAPMTs till the installation while he initiated the test of prototypes of the SiPMs to investigate their performances for the future installation. The activity on the MAPMTs involved the characterization tests, their assembling on the final detector and the first functionality tests. For the SiPMs, the work focused on the develoment of a dedicated analysis to investigate the single photon detection capability for state-of-the-art ~~of the~~ silicon photomultipliers under irradiation conditions and on the firsts studies of SiPM matrices connected with the same readout electronics used for the MAPMTs that has been already optimized for the first sector.

The work on the MAPMTs allowed to check the proper functioning of the full chain of photon detector components that were connected together for the very first time. The tests were performed in the laser stand prepared inside a dark box to investigate the performance of each readout units (composed by MAPTMs, adapter board, MAROC board and FPGA) as a function of the experimental parameters. The setup was prepared to run the tests at different high voltages supplied to the photomultipliers, at different MAROC gains amplifying the signal before digitalization and at different discriminating thresholds for the digital part of the readout. Different values has been chosen for each parameter to span the full range available. Such an extensive characterization if crucial to define a set of parameters that allows to maximize the performance during the experiment.

The analysis shows that a saturation of the detection efficiency could be reached in a wide range of working parameters, as this is ultimately limited

by the photocathode quality. This allows some freedom in the choice of the
working point. The high voltage can then be taken at the lower value of the
recommended range, i.e. 1000 V, to minimize ~~aeging~~ effects and keep power
leverage in case of MAPMTs performance degradation. On the another side,
the chance that the electronics gives to amplify or reduce the signal regulat-
ing the MAROC gain can be used to equalize the signals among the MAPMT
anodes, as the MAROC discriminating threshold is common to all the readout
channels. For the digital readout, a threshold relative to the pedestal will
be the best choice not to cut out a significant fraction of the signal with an
hardcoded online selection. The cross-talk effects can be controlled with a
threshold level and by the offline analysis. Moreover, this test identified a full
set of performance indicators that can be compared with the ones that will
be extracted in the future during the calibration runs of the experiment: it
will allow to follow the ~~aeging~~ and eventually to correct some parameters to
maximize the performance in real time.

The work on the SiPM has been presented in two different parts: the first part
involves an irradiation test and the second one is correlated to the ~~test with
SiPM matrices started to test the~~ readout electronics of the first sector of the
RICH together with the new photon detector.

During the test at the ENEA of Frascati, several $3 \times 3\,\mathrm{mm}^2$ SiPM prototypes
have been irradiated. They were from different companies, of different micro-
cell sizes and also of different technologies, i.e. standard ones and brand new
ones improved to reduce noise, such as crosstalk, with the so-called trenches.
To understand and deeply investigate their behaviour in a moderate radia-
tion environment such as CLAS12 an in-depth analysis has been performed on
the dark counts. As a start, the standard I-V characteristic curve has been
extracted at different irradiation stages. The absorbed current increases, as
expected, with the accumulated dose and no improvement with the new tech-
nology has been observed. To improve our knowledge on the dark counts the
author implemented an innovative analysis to study the signal sampled from
an oscilloscope to recognize and distinguish single micro-~~cells~~ discharges with
respect to multiple micro-~~cells~~ discharges and to follow their number increas-
ing as a function of the accumulated dose. In this case a difference between
standard technology and the one with trenches has been pointed out: the new
technology have a negligible number of secondary discharges (due to optical
crosstalk) before irradiation. With the increasing of the accumulated dose
the response gets worse in both cases and the number of secondary discharges
tends to become similar ~~but~~ with the new analysis developed, it is still possible
to distinguish single from multiple discharges even after a dose ~~close~~ to 10 year
of CLAS12 data taking at maximum luminosity.

SiPMs have been validated as photon detector for the future RICH module as photon counting is still manageble at CLAS12 radiation levels.

Accordingly with these results, new tests have been started on a 4×4 SiPM matrices with the RICH readout. A very preliminary test is presented to confirm that the SiPM matrices are able to communicate with the RICH electronics and detect single photon. Further tests need to be performed to investigate in details properties and performance, but the use of SiPMs in conjunction with the RICH electronics has been validated.

As conclusion, the assembling and commissioning of the first sector of the RICH detector has been presented. Several tests have been performed to prepare the active area of the RICH detector before the final installation in the experimental hall. Starting from mechanical test during the assembling, following by the validation of the online monitoring and of the slow control and ending with a cosmic stand and beam test. Here the preliminary results are presented to show that the detector is ready to fulfill the requirements of the experiment in terms of time resolution, that the detector response can be effectively controlled by means of the studied parameters and that the proper working point has been defined and implemented.

The work presented in this thesis represents a great example of the initial statements. The necessity to deepen our knowledge in high energy physics requires a huge technological development. As the first sector of the RICH detector is ready to be operated with the mature MAPMTs technology, the studies for its upgrade with SiPM sensors to be used in the second sector already started.

Bibliography

[1] J. Dudek et al., Physics Opportunities with the 12 GeV Upgrade at Jefferson Lab

[2] CLAS12 Technical Design Report, Technical Design Report $v\_5.1$, JLAB, 2008

[3] The CLAS12-RICH Technical Design Report, Technical Design Report v_1, JLAB, 2013

[4] A. Bacchetta and M. Contalbrigo, The proton in 3D, Il nuovo saggiatore, vol28, 2012

[5] M. Contalbrigo et al., "The CLAS12 large area RICH detector", NIMA, vol.639, 2011, pp.302-306, https://doi.org/10.1016/j.nima.2010.10.047

[6] H. Avakian et al.,"Probing Strangeness in Hard Processes; the science case of a RICH detector for CLAS12", arXiv: 1202.1910

[7] M. Contalbrigo at al., "The Large-Area CLAS12 Ring-Imaging Cherenkov Detector", ICATPP 2013

[8] A. El Alaoui, "A RICH Detector for CLAS12 Spectrometer", Physics Procedia 37 (2012) pp.773–780, TIPP 2011

[9] S. Anefalos Pereira et al., "Test of the CLAS12 RICH large scale prototype in the direct proximity focusing configuration", Eur. Phys. J. A (2016) 52:23, DOI 10.1140/epja/i2016-16023-4

[10] L.L. Pappalardo, "The RICH detector for CLAS12 at Jefferson Lab", EPJ Web Conf. 73 (2014), https://doi.org/10.1051/epjconf/20147308003

[11] A. Augusto Alves et al., "The LHCb Detector at the LHC", JINST 3 S08005

[12] R. Montgomery, "A Ring Imaging Cherenkov Detector for CLAS12", NIMA, vol.732, 2013, pp.366–370, https://doi.org/10.1016/j.nima.2013.08.012

[13] M.Hoek et al., "Investigation of Hamamatsu H8500 photo-tubes as single photon detectors", NIMA, vol.790, 2015, pp.28-41, https://doi.org/10.1016/j.nima.2015.03.068

[14] S. Blin et al., MAROC3 datasheet - draft, October 2010, Omega web site: http://omega.in2p3.fr/

[15] M. Contalbrigo et al., "The large-area hybrid-optics CLAS12 RICH detector: Tests of innovative components", NIMA, vol.766, (2014), pp.22–27, https://doi.org/10.1016/j.nima.2014.06.072

[16] http://meroli.web.cern.ch/meroli/Lecture_photon_interaction.html

[17] http://www.nuclear-power.net/nuclear-power/reactor-physics/interaction-radiation-matter/interaction-gamma-radiation-matter/

[18] https://www.nucleonica.com/wiki/images/0/02/Dosimetry_Shielding.pdf

[19] https://psec.uchicago.edu/links/Photomultiplier_Handbook.pdf

[20] S. Donati at al., "Single-Photon Detectors: From Traditional PMT to Solid-State SPAD-Based Technology", IEEE, 10.1109/JSTQE.2014.2350836

[21] Photomultiplier tubes - basic and applications, 3d ed. Hamamatsu. https://www.hamamatsu.com/resources/pdf/etd/PMT_handbook_v3aE.pdf, 2007

[22] R. Montgomery et al., "Multi-anode photomultiplier tube studies for imaging applications", NIMA, vol.695, 2012, pp.326–329, 2012. https://doi.org/10.1016/j.nima.2011.11.026

[23] R. Pestotnik et al., "Proximity focusing RICH with flat panel PMT (Hamamatsu H8500) as photon detector and aerogel radiator", NIMA, vol.525, 2004, pp.158-162, https://doi.org/10.1016/j.nima.2005.08.007

[24] T. Matsumoto (Tokyo Metropolitan U.) et al., "Studies of proximity focusing RICH with an aerogel radiator using flat panel multi-anode PMTs (Hamamatsu H8500)", NIMA, vol.521, 2004, pp.367-377, https://doi.org/10.1016/j.nima.2003.11.384

[25] M. Contalbrigo, "Tests of innovative photon detectors and integrated electronics for the large-area CLAS12 ring-imaging Cherenkov detector", NIMA, vol.787, 2015, pp.224–228, http://dx.doi.org/10.1016/j.nima.2014.12.009.

[26] TRB Collaboration (C. Pauly et al.), "Upgrade of the HADES RICH photon detector with H12700 MAPMTs", NIMA, vol.876, 2017, pp.164-167. http://doi.org/10.1016/j.nima.2017.02.067

[27] J. Adamczewski-Musch et al., "Single photon test bench for series tests of HAMAMATSU H12700 MAPMTs", NIMA, vol.876, 2017, pp.123-125, http://doi.org/10.1016/j.nima.2017.02.034

[28] http://www.hamamatsu.com/resources/pdf/ssd/mppc_kapd9005e.pdf

[29] https://www.first-sensor.com/cms/upload/appnotes/ AN_SiPM_Introduction_E.pdf

[30] https://www.sensl.com/downloads/ds/TN-IntrotoSPMTech.pdf

[31] Slawomir Piatek, Technical guide to silicon photomultipliers, January 2017, Hamamatsu Corporation & New Jersey Institute of Technology https://www.hamamatsu.com/us/en/community/optical_sensors/articles/ technical_guide_to_silicon_photomultipliers_sipm/index.html

[32] NUV SiPMs Chip Scale Package (CSP), Advansid http://advansid.com/attachment/get/up_53_1432731710.pdf

[33] RGB SiPMs Chip Scale Package (CSP), Advansid http://advansid.com/attachment/get/up_53_1432741078.pdf

[34] Photomultiplier tubes, Hamamatsu https://www.hamamatsu.com/resources/ pdf/etd/PMT_TPMZ0002E.pdf

[35] Flat Panel Type Multi-Anode PMT Assembly H8500 Series, Hamamatsu https://www.hamamatsu.com/resources/pdf/etd/H8500_H10966_TPMH1327E.pdf

[36] Flat Panel Type Multi-Anode PMT Assembly H12700 Series, Hamamatsu https://www.hamamatsu.com/resources/pdf/etd/H12700_TPMH1348E.pdf

[37] MPPC and MPPC module for precision measurement, Hamamatsu https://www.hamamatsu.com/resources/pdf/ssd/mppc_kapd0004e.pdf

[38] MPPC(multi-pixel photon counter)S12572-025,-050,-100, Hamamatsu http://www.hamamatsu.com.cn/UserFiles/DownFile/Product/ 20140117212906284.pdf

[39] https://www.hamamatsu.com/us/en/support/glossary/c/index.html

[40] I. Balossino, et al., "Cherenkov light imaging tests with state-of-the-art solid state photon counter for the CLAS12 RICH detector", NIMA, vol. 876, 2017, pp.89-92, https://doi.org/10.1016/j.nima.2017.01.074

[41] R. Pestotnik, et al., "Module of silicon photomultipliers as a detector of individual Cherenkov photons", NIMA, vol.639, 2011, pp.99–102, http://dx.doi.org/10.1016/j.nima.2010.09.122.